Engineering Heterogeneous Biocatalysts

Tushar N. Patel

Submitted in partial fulfillment

of the requirements for the degree of

Doctor of Philosophy

in the Graduate School of Arts and Sciences

COLUMBIA UNIVERSITY

2014

ABSTRACT

Engineering Heterogeneous Biocatalysis

Tushar N. Patel

In heterogeneous catalysis, the phase of a catalytic agent, which is responsible for reducing the activation energy of a reaction, is different from the phase of its reactants or substrates. Often, soluble catalysts are tightly associated with an inert carrier in order to artificially alter their phase. Applying this concept to biocatalysis yields a system in which enzyme molecules are immobilized on a solid support. This often serves to stabilize the enzyme, as well as enhance the recyclability of the enzyme since it is no longer soluble. In this dissertation, two methods of enzyme immobilization are evaluated: adsorption to a solid surface and whole-cell biocatalysis. The latter is then engineered for improved kinetics and functional activity using principles of synthetic biology.

Adsorption of a protein to a solid surface is driven by the same thermodynamic factors that are responsible for the folding of a protein. Hydrophobic interactions, ionic interactions, covalent bonding, and weak forces all contribute to minimizing the free energy of a protein, which defines its secondary, tertiary, and quaternary structures. Upon introduction to a surface, these different forces rearrange across the surface of the substrate to minimize the free energy of the system. Many factors influence this behavior, including particle curvature, material properties of the surface, and the stability of the protein. In the preexisting body of work, much of the research performed regarding the effects of thermal stability on adsorption were performed using mutant proteins whose structures were intentionally altered for a range of stabilities.

In Chapter 2, we evaluate the effects of thermal stability on adsorption behavior using naturally evolved enzymes from the AKR superfamily, namely AdhD and hAR. These enzymes were

selected for their structural homology, but vastly different thermal stabilities. Using these proteins, we demonstrate that the previously held theories of thermostable protein adsorption behavior are not entirely applicable to naturally evolved proteins that are not artificially stabilized. We also propose a modification to the classic 4-state adsorption/desorption model by introducing new pathways and protein states based on our experiments.

In addition to physisorption, whole-cell biocatalysis was explored as an enzyme immobilization platform. In general, this can be accomplished by cytosolic expression, periplasmic expression, or surface display. After weighing these options, we chose periplasmic expression in *E. coli* for our biocatalysts. As for the catalytic component, we selected carbonic anhydrase (CA), a class of Zn^{+2}-binding metalloenzymes that are capable of catalyzing the reversible hydration of CO_2. This enzyme was selected for the breadth of applications it can be used for, as well as its ubiquity in nature and extremely fast kinetics. Two isoforms were selected (Cab and Cam) for their respective benefits and were periplasmically expressed using 2 different leader peptides, which we discuss in Chapter 3. The enzyme loading in the periplasm, kinetics, thermal stability, and functional activity are all reported for the resulting whole-cell biocatalysts. We also describe a new method for the measurement of the operational stability of CA-based biocatalysts.

Modifications to the whole-cell biocatalysts are described in Chapter 4 and Chapter 5. In Chapter 4, we demonstrate that expression of a viral envelope protein enhances the permeability of the outer membranes of *E. coli* cells. We characterize this improvement by measuring small-molecule permeance, whole-cell kinetics, and functional activity of the modified biocatalysts. We also quantify this enhancement by applying concepts of porous chemical catalysts to our whole-cells. In doing so, we show improvements in parameters such as the effectiveness factor, Thiele modulus, diffusivity, and permeability.

Finally, in Chapter 5 we show enhancement of the functional activity of the whole-cell biocatalysts by displaying small peptides on the outer surfaces of the cells. The modified cells are shown to enhance precipitation of calcium carbonate, a common end product of carbon mineralization. Improved solid formation rates are also reported and possible explanations for these effects are discussed.

Overall, this dissertation explores immobilization of enzymes to create heterogeneous biocatalysts. First, the effects of immobilization on enzyme structure, stability, and activity are shown for two different immobilization techniques: adsorption to a solid surface and periplasmic expression in *E. coli* cells. After characterization, engineering of the whole-cell biocatalysts for improved properties is presented. Finally, future directions for this work are discussed which would advance our understanding of heterogeneous biocatalysts, as well as enhance their utility.

Table of Contents

List of Figures

List of Tables

Acknowledgements

Throughout my time as a Ph.D. candidate at Columbia, starting in 2009, I have had many people behind me that have helped make this dissertation a reality.

To my advisor, Dr. Scott Banta, thank you for the opportunity to conduct my research in your lab, and for your mentorship, optimism, and support throughout my time here.

Thank you to Drs. Sanat Kumar, Alissa Ah-Hyung Park, V. Faye McNeill, Jingguang Chen, and Scott Banta for serving on my defense committee.

Thank you to the members of the Banta Lab, past and present, for your camaraderie and advice. In particular, I would like to acknowledge Kevin Dooley for helping preserve my sanity and focus, as well as Elliot Campbell, Flora Felsovalyi, and Oren Shur, for their guidance and assistance in my early days. Thank you as well to my collaborator and close friend, Ed Swanson, for your timely and practical advice.

I would also like to thank my friends from New York, Boston, and Shrewsbury for the motivation and timely distractions they have provided over the years.

To my parents, Navin and Jyoti, and my sister, Tejal, I would not be in this position in my life without your unwavering love, patience, and guidance. You have given me every opportunity to succeed and I am extremely grateful for that.

Thank you also to Katie and Jonathan Wienslaw who have always treated me as one of their own. Your support has never faltered and that truly means a great deal to me.

Finally, I must take this opportunity to thank my loving fiancée and soon-to-be wife, Betsy. Your undying encouragement, patience, and optimism throughout this process have not gone unappreciated.

1. Introduction

1.1. Heterogeneous Biocatalysis

For most chemical reactions, catalysts can be used to decrease the activation energy required to reach a transition state, a necessary intermediate for product formation. Enzymes are proteins that are capable of catalyzing a wide spectrum of chemical and biochemical reactions. Due to their high substrate specificity, efficiency, kinetics, and biodegradability, enzymes are becoming increasingly common in many industries including food processing and the manufacturing of cleaning products [1]. Enzymes also have medical applications including the chemical synthesis of pharmaceutical intermediates [2] and the treatment of leukemia, jaundice, and blood clots [1]. Although these enzymes are generally not consumed during the reactions they catalyze, they do possess finite lifetimes due to degradation of their active sites, or the protein altogether. In most situations, fresh enzyme would be added to a reaction to account for this loss of activity. However, modification of the enzyme to increase its stability has the potential to be a more cost-effective solution to this issue [1]. Such modifications could include engineering the amino acid sequence of the protein to alter its intrinsic stability, which is a common practice, or immobilizing the enzyme to generate a heterogeneous biocatalyst.

In general, a heterogeneous catalyst is one in which the phases of the catalytic agent and its reactants are different. Commonly, the phase of a catalyst can be altered by tightly associating it to an inert carrier via covalent attachment, attractive forces, or entrapment. In terms of an enzymatic reaction, this would involve immobilization of the enzyme onto a solid support before introduction to a reaction or process. Heterogeneous biocatalysts have been previously used in

industries such as polymer synthesis [3], amino acid synthesis [4], and electrochemical enzyme assays [5].

Depending on the enzyme and immobilization strategy used, the stability, activity, and selectivity of a biocatalyst can all be enhanced [6]. In terms of stability, immobilization can be used to increase the operational, storage, and chemical stability of the protein, as well as increase its resistance to oxygen or peroxide [7]. Immobilization also facilitates reuse of the biocatalyst [1]. Although adding free enzyme to a reactor would result in efficient operation, separation of the protein molecules from the reaction solution for reuse would be difficult, time-consuming, and expensive. Immobilizing the enzyme renders it insoluble, which is much more conducive to recycling.

In this work, two immobilization modalities were explored: physical adsorption to a non-functionalized solid surface, and periplasmic expression in *Escherichia coli* cells to generate whole-cell biocatalysts. Each of these techniques has their own benefits and drawbacks, as outlined below.

1.2. Protein Adsorption to Solid Surfaces

The adsorption of proteins to a solid surface is governed by the same interactions that are responsible for the secondary, tertiary, and even quaternary structure of a protein. Hydrogen bonding, hydrophobic interactions, disulfide bridges formed between cysteine residues, ionic bonds, and weak interactions such as van der Waals forces and Coulomb interactions all contribute to protein folding [1, 8]. Upon introduction to a solid surface, a protein's structure will rearrange such that the Gibbs Free Energy (ΔG) of the system is minimized. In fact, even in

the presence of a net repulsive force, a protein will still undergo conformational changes to minimize ΔG [9], which is defined as:

$$\Delta G_{ads} = \Delta H_{ads} - T\Delta S_{ads} \quad (1)$$

In general, the adsorption of protein molecules to a surface is entropically driven. The dehydration of hydrophobic domains on the surface, the dissociation of entrained water molecules within the protein, and the surface-induced conformational changes experienced by the protein all contribute to this term. Enthalpic driving forces are determined by the conformational changes upon adsorption, ion transport to the adsorbed protein, and charge rearrangements. Ion transport and charge redistribution are dependent on the pH, charge difference between the adsorbent and protein, and ionic strength of the solution [10]. Also, it has been shown that on a bare surface, the adsorption of one protein molecule promotes the adsorption of subsequent molecules. This means that once one protein molecule has adsorbed, a cascade of protein adsorption and unfolding is initiated [11]. However, it is still largely unknown what properties are responsible for the amount of protein adsorbed and the extent of denaturation. According to the current literature, the two most important factors to consider are the curvature of the particles [12, 13] and the stability of the protein [14, 15].

Adsorbed proteins can often be desorbed easily with a slight change in ionic strength, pH, or even a concentration gradient between the surface and bulk solution. Since proteins lack structural memory, refolding upon desorption will usually stop at a stable intermediate, also known as a molten globule state [16]. In such a state, the protein's structure achieves a local minimum in free energy before reaching the global minimum defined by a correctly folded

molecule. This could have significant implications in applications such as therapeutic proteins where misfolding could skew the activity, efficacy [17], or toxicity of the protein [18].

The concepts described above have long been a topic of interest among researchers. For example, it has been previously reported that adsorbed Bovine Serum Albumin (BSA) on silica particles showed significant conformational changes, often resulting in a 60% loss in α-helical structure. Upon desorption with a low concentration of morpholine, some of those helical domains were restored, but the total helical content was still about 30% less than the native structure [9]. This structural rearrangement has previously been shown to translate into losses in a protein's physical and chemical properties including activity [19] and thermal stability [20].

Other studies have demonstrated the effects of carrier particle diameter on adsorption behavior. Both lysozyme [12] and Human Carbonic Anhydrase I (HCAI) [13] have been shown to be susceptible to curvature effects. In both cases, larger particles with less apparent curvature relative to protein size resulted in a higher degree of protein denaturation than smaller particles. Further, it has been speculated that larger particles are more conducive to multilayer adsorption as opposed to monolayer formation. This hypothesis was made by comparing the measured amount of protein adsorbed to a theoretical amount of protein that would be required to form a monolayer [12].

Finally, the effects of thermal stability on adsorption behavior were previously studied using T4 lysozyme (T4L) adsorbed onto silica wafers [21], nanoparticles [15], and planar mica surfaces [14]. In these studies, wild-type T4L was compared to mutants I3W, I3C, and I3L in which the isoleucine residue at position 3 was changed to tryptophan, cysteine, and leucine, respectively. Of these mutants, I3W was the least stable, followed by the wild-type enzyme, I3L, leaving I3C

as the most stable mutant. This is unsurprising since the cysteine substitution allowed for the formation of an additional disulfide bridge not present in the wild-type enzyme. This extra covalent bond increased the energy required for denaturation and therefore, the stability of the mutant. The conclusion of all of these studies was that less stable proteins undergo more extreme conformational changes in both secondary and tertiary structure [14, 15, 21]. While these conclusions appear definitive, there exists a gap in the current literature.

The studies described above all used artificially stabilized (and similarly destabilized) mutants. However, naturally-evolved homologous proteins with similar structures but different thermal stabilities have been scarcely used for this type of analysis. This work addresses this gap using the model system described below.

1.2.1. Model System: Aldo-keto Reductases with Distinct Thermostabilities

As described above, previous studies that relate thermostability to adsorption behavior have been performed, but used engineered mutants of a wild-type enzyme. Instead of using artificially stabilized proteins, the work presented herein used two enzymes from the Aldo-Keto Reductase (AKR) Superfamily. The first is a highly thermostable Alcohol Dehydrogenase D (AdhD) from the hyperthermophile *Pyrococcus furiosus* [22]. The other is a mesostable Aldose Reductase (hAR) found in humans [23]. These proteins were selected because of their shared $(\alpha/\beta)_8$-barrel type crystal structures [24], which confers NAD(P)(H)-dependent activity to most proteins containing this scaffold [25]. Almost all of the oxidoreductase enzymes in the AKR superfamily exhibit this characteristic structure, despite low primary sequence homology across the various proteins. Since the only significant difference between AdhD and hAR is their thermal stabilities, they are ideal candidates for determining the impact of inherent, native stability on adsorption behavior.

1.3. Whole-Cell Biocatalysis

In contrast to physically adsorbing a protein onto a solid surface, whole-cell biocatalysts are in large part self-assembled where the host cell that expresses a protein also becomes its carrier. This provides a distinct advantage over adsorption or other immobilization techniques because protein purification, which is often a very time-consuming and expensive process, is not necessary. Also, solid supports onto which the enzymes are to be immobilized are no longer required, offering an additional cost benefit. Whole-cell biocatalysts have been previously shown to be viable for applications such as the production of biofuels [26], chiral alcohols [27], and L-amino acids [28], among others. Most commonly, these biocatalysts are generated by recombinant overexpression of an enzyme within the cytosol [26], the periplasm of gram-negative bacteria such as *Escherichia coli* [29], or on the exterior surface of the cell [30]. However, native cells have also been previously used as whole-cell biocatalysts [31]. Cytosolic expression is most easily achieved by simply cloning the gene encoding the protein of interest into an expression vector, of which there are a large number available. Periplasmic expression can be achieved by fusing the desired protein to a signaling peptide or periplasmic protein in order to direct it to the periplasm [32]. If desired, the fusion can either be cleaved or left intact after translocation. Surface display can be achieved by a number of different means [33]. One of the most common methods is fusion of the protein of interest to a transmembrane protein such that the recombinant protein is exposed to the extracellular matrix [32]. Each of these methods possesses their own limitations and advantages which must be balanced when selecting an immobilization method.

Initially, it would appear that surface display would be the most attractive method of whole-cell heterogeneous biocatalysis since the enzyme has direct access to its substrate(s) and cofactor(s)

with little chance of local product accumulation. However, this technology is not without limitations. Activity losses, difficulties with displaying multiple proteins at once, and difficulties with multi-subunit proteins are all challenges associated with the use of surface display [34]. Further, low expression levels and exposure to the extracellular space could be potential limitations of this technique.

Of the two intracellular compartments, expression in the cytosol generally results in the highest levels of protein expression. The cytosol is also a favorable environment for most proteins, so proper folding is almost guaranteed [35]. Periplasmic expression, on the other hand, has slightly lower yields and is an oxidative environment, which may not be conducive to the correct folding of all proteins [35, 36]. However, since the periplasm constitutes a small portion of the total cell volume (~10% [37]), a high degree of crowding within this space is assumed. This could result in unfavorable entropic penalties for protein unfolding, thus stabilizing the recombinant enzymes.

The main limitation to using whole-cell biocatalysts generated by either cytosolic or periplasmic expression is the reduction in catalytic efficiency as a result of mass transport limitations across the semi-permeable cell membranes. It has been reported that the reaction rate of a whole-cell biocatalyst can be up to 2 orders of magnitude slower than the free enzyme. This limitation could cause an accumulation of product within the cell, which in some cases could lead to product inhibition [38]. Thus, whole-cell biocatalysts generated by intracellular expression are, in general, diffusion-limited.

While recombinant enzyme expression in either of the two cellular compartments is subject to this transport limitation, periplasmic expression is slightly more favorable in this regard. For a periplasmically expressed enzyme, the required substrate(s) and/or cofactor(s) need only diffuse

across the cell's outer membrane, as opposed to both the outer and inner membrane, as with cytosolic expression. Similarly, the product(s) formed by the catalyzed reaction can diffuse out of the periplasm more easily, thus reducing the effect of product inhibition.

In this work, whole-cell biocatalysts for the hydration of CO_2 were generated via periplasmic expression of carbonic anhydrase. These biocatalysts were characterized and modified for improved properties.

1.3.1. Model System: Carbonic Anhydrase

Carbonic anhydrases (CA) are Zn^{+2}-binding metalloenzymes that are nearly ubiquitous in nature; almost all living organisms produce at least one form [39, 40]. The primary function of these enzymes is the reversible hydration of CO_2, accomplished via the bound Zn^{+2} ion [41]. These enzymes are among the fastest ever discovered, with turnover numbers (k_{cat}) ranging from 10^4-10^6 sec^{-1} [42]. Potential inhibitors for these enzymes include monovalent anions that nonspecifically bind to the active site, sulfonamides, which bind to the metal atom preventing its association with a water molecule, imidazole, which will weakly compete with CO_2 [39], and topoiramate, which infiltrates the active site of human carbonic anhydrase [43]. CA enzymes can be divided into three main classes: α-, β-, and γ-class. The α-class contains all mammalian and *E. coli* isoforms, as well as two enzymes from the algal species *Chlamydomonas reinhardtii* [42]. The β-class is comprised of isoforms from all plants [44], *Neisseria gonorrhoeae*, and *Methanobacterium thermoautotriphicum* [45]. Finally, the only enzyme currently belonging to the γ-class is natively found in *Methanosarcina thermophila*. This enzyme exhibits a left-handed β-helix fold, which is not present in any other carbonic anhydrase [42, 46]. Potential

applications for these enzymes include carbon capture [47], engineered photosynthesis [48], biofuel production [49], and electrochemical biosensors [50].

Due to the ubiquity of these enzymes, two were selected for investigation within this work: Cab (*Methanobacterium thermoautotriphicum*; PDB: 1G5C) and Cam (*Methanosarcina thermophile*; PDB: 1THJ). Cab is a β-type CA and is among the most thermostable isoforms ever discovered [42]. Cam is the γ-type CA described above and while less thermally stable than Cab, it is natively expressed in the periplasm, which insures its efficacy in an oxidative environment [51]. Both enzymes possess k_{cat} values on the order of 10^4 sec^{-1}, which puts them among the slower forms of CA, but still incredibly fast relative to other families of enzymes [45]. Due to the distinct advantages each isoform exhibits, these two enzymes were selected to generate whole-cell biocatalysts via periplasmic expression.

1.4. Research Goals

Heterogeneous biocatalysis harbors great potential for use in industrial and research applications, as discussed above. Immobilization of an enzyme can increase its stability, and enhance its recyclability by rendering it insoluble. In this research, the main goals were to evaluate various immobilization techniques, and to engineer an efficient and stable heterogeneous biocatalyst. The specific scientific and engineering goals undertaken in this endeavor are outlined below, along with their corresponding chapters within this thesis:

Goal 1: Investigate the effects of inherent thermostability on protein adsorption to a solid surface

This goal is addressed in Chapter 2, in which AdhD and hAR were used to determine if native thermal stability changes the adsorption behavior of proteins with similar secondary structures.

To do so, Langmuir adsorption isotherms, circular dichroism (CD), and standard NAD(P)(H) activity assays were used to characterize the proteins in their native, adsorbed, and desorbed states.

Goal 2: Create and characterize whole-cell biocatalysts possessing CA activity

This goal is addressed in Chapter 3, where Cab and Cam were periplasmically expressed in *E. coli* and characterized using quantitative western blotting, stopped-flow spectroscopy, and a calcium carbonate precipitation assay to demonstrate their potential for use in an industrial application. Further, the thermal stabilities of free and immobilized enzymes were determined and compared. Finally, a new method for measuring the operational stability of CA-based biocatalysts, a technology surprisingly scarce in current literature, was developed and used to evaluate the various biocatalysts.

Goal 3: Engineer the outer membranes of the whole-cell biocatalysts for enhanced kinetic activity

In Chapter 4, the outer membrane of each biocatalyst was permeabilized via recombinant expression of a viral protein known to increase permeability in *E. coli*. These modified biocatalysts were then evaluated using stopped-flow spectroscopy, a membrane-permeability assay, and the carbonate precipitation assay. These permeabilized cells were then subjected to quantitative characterization using principles of porous catalysts to determine the improvements in various reaction-diffusion parameters.

Goal 4: Engineer the outer membranes of the whole-cell biocatalysts for enhanced functional activity

In Chapter 5, the outer surfaces of the biocatalysts were functionalized with small peptides to enhance the precipitation of carbonates, which again demonstrated their potential for use in an industrial application. In order to do so, the peptides were fused to a version of a native transmembrane protein engineered to display both of its termini to the extracellular space. Successful expression of these fusions was confirmed by Flow Cytometry. Their effectiveness was evaluated by the carbonate precipitation assay, as well as an assay for precipitation kinetics.

2. Immobilization via Adsorption: The Effects of Intrinsic Thermal Stability

Note: A version of this chapter entitled "Effect of thermal stability on protein adsorption to silica using homologous aldo-keto reductases." is published in *Protein Science* (2012), volume 21, issue 8, pages 1113-1125, with co-authors Flora Felsovalyi, Paolo Mangiagalli, Sanat K. Kumar, and Scott Banta.

TNP cloned the hAR construct, collected and analyzed the hAR data, and assisted in the writing of the manuscript.

2.1. Abstract

Gaining more insight into the mechanisms governing the behavior of proteins at solid/liquid interfaces is particularly relevant in the interaction of high-value biologics with storage and delivery device surfaces, where adsorption-induced conformational changes may dramatically affect biocompatibility. The impact of structural stability on interfacial behavior has been previously investigated by engineering non-wild-type stability mutants. Potential shortcomings of such approaches include only modest changes in thermostability, and the introduction of changes in the topology of the proteins when disulfide bonds are incorporated. Here we employ two members of the aldo-keto reductase superfamily (alcohol dehydrogenase, AdhD and human aldose reductase, hAR) to gain a new perspective on the role of naturally occurring thermostability on adsorbed protein arrangement and its subsequent impact on desorption. Unexpectedly, we find that during initial adsorption events, both proteins have similar affinity to the substrate and undergo nearly identical levels of structural perturbation. Interesting differences between AdhD and hAR occur during desorption and both proteins exhibit some level of activity loss and irreversible conformational change upon desorption. Although such surface-induced denaturation is expected for the less stable hAR, it is remarkable that the extremely thermostable AdhD is similarly affected by adsorption-induced events. These results question the role of thermal stability as a predictor of protein adsorption/desorption behavior.

2.2. Introduction

Over the past few decades, extensive focus has been applied to understanding the mechanisms governing the behavior of proteins at solid/liquid interfaces. Due to wide-spread implications of this phenomenon in numerous applications, a large number of systems have been studied. To gain more insight into how protein structure affects interfacial behavior, the importance of surface charge [52, 53], hydrophobicity [54], and structural stability [14, 55] have been investigated.

Approaches to study the effects of these parameters can be categorized as follows: the study of well-defined model proteins [8, 56-59], genetic variants [60, 61], mutants of single proteins [15, 21, 62], and most recently, synthetic polypeptides [63-65]. Significant effort in the two former categories has pioneered our overall understanding of the mechanisms governing protein adsorption; however, it is the latter groups in which the effect of subtle molecular effects can be assessed. Thus, ideal studies could be envisioned in which a single parameter, such as stability or surface charge, are studied in isolation.

Many of these studies have explored the structural consequences of adsorption. Elbaum [66] used stability variants of hemoglobin to hypothesize a strong structural basis for observed differences in adsorption kinetics and protein unfolding at the air/water interface. Kato [67] strengthened this correlation between conformational stability and interfacial affinity and level of surface-induced perturbation using tryptophan synthase mutants. More recently, bacteriophage T4 lysozyme has been the protein of choice for similar studies because it is extremely well characterized and synthesis of stability mutants is well documented. McGuire [62] created T4 variants with enhanced stability by introducing cysteine residues to form additional intra-molecular disulfide linkages. Following the kinetics of adsorption and elutability, they postulated

a correlation between protein stability and time-scale of attachment and binding strength. CD spectroscopy revealed that both the rate and extent of unfolding (characterized by α-helical loss) upon adsorption to silica nanoparticles was most pronounced for the least stable mutants [55]. The general hypothesis emerging from these studies is a strong correlation between thermostability and affinity of surface attachment, structural perturbation and desorbability. However, there are two potential shortcomings with the application of stability mutants to evaluate surface activity. First, only incremental changes in stability can be assessed. The range of stabilities is limited by the number of residue substitutions which alter stability without impacting secondary structure. Second, stability is artificially optimized in these systems. For example, common approaches involve strategically placed disulfide bonds or the insertion of residues with side chains that cause steric disruptions in critical locations. However, these approaches change the topology of the peptide chain and it is difficult to decouple the effect of the stability-altering mutations from the effect on protein-surface interactions.

The goal of our investigation is to explore the relationship between stability and adsorption behavior using naturally evolved homologs with very similar 3-D structures yet vastly different intrinsic stabilities. We have chosen two members of the aldo-keto reductase (AKR) superfamily [24] which share high structural homology with low primary sequence homology (Figure 2-1). The members of the AKR superfamily are monomeric, do not contain disulfide bonds, and fold into well-known 8 stranded, TIM-like, α/β barrels. The first enzyme, alcohol dehydrogenase D (AdhD) from the hyperthermophilic archaea *Pyrococcus furiosus*, is highly thermostable [22, 68] while the second enzyme, human aldose reductase (hAR), is mesostable [23]. We believe this is the first time that homologous stability variants have been used to explore the effects of protein

stability on interfacial behavior. Adsorption and desorption were investigated using a hydrophilic silica surface which was previously used in adsorption studies of model proteins [9, 69, 70]. Based on previous results, we hypothesized that AdhD and hAR would exhibit different adsorption behavior due to their drastically different thermostabilities. Unexpectedly, our results indicate that both proteins have similar affinities to the substrate and undergo nearly identical levels of structural perturbation. Interesting differences between AdhD and hAR are observed during desorption, with respect to elutability, refolding pathways and distribution of desorbed structural states. Both proteins exhibit some level of activity loss and irreversible conformational change upon desorption. Although surface-induced denaturation and activity loss is expected for the less stable hAR, it is remarkable that AdhD, which retains native-like structure and activity at even at 100°C, is significantly affected by adsorption-induced events. Therefore, our results suggest that intrinsic structural stability may not be the most accurate predictor of adsorption behavior, and that other predictors, such as electrostatics, may have a greater impact on the extent of surface affinity and unfolding. These results may call into question the commonly held belief that increasing thermostability should reduce surface activity.

2.3. Materials and Methods

Materials. DNA oligonucleotides were synthesized by Integrated DNA Technology (IDT; Coralville, IA). Isopropyl β-D-1-thiogalactopyranoside (IPTG) was obtained from Promega (Madison, WI). Fumed colloidal silica particles (Cab-o-sil M-5, <99.8% purity) were purchased from Cabot Corp. (Boston, MA) and used without further treatment. Bicinchoninic acid (BCA) and QuantiPro BCA Assay kits were purchased from Thermo Fisher Scientific (Rockford, IL). Restriction enzymes *Nco*I and *Hind*III, T4 DNA Ligase, and Phusion DNA Polymerase were

purchased from New England Biolabs (Ipswich, MA). All other chemicals were obtained from Sigma-Aldrich (St. Louis, MO).

Cloning. The hAR gene was amplified from human placental cDNA (Clontech, Mountain View, CA) using overlap extension PCR to eliminate an internal *Nco*I restriction site present in the hAR gene. Detailed information about the primers can be found in the Supplementary Information (Section 2.8). The purified PCR fragment was doubly digested and ligated into a similarly digested pET-24d (Novagen, Gibbstown, NJ) vector containing a poly-His tag. Ligated plasmids were electroporated into BLR *E. coli* cells (Novagen) and selected on LB agar plates supplemented with 50 ng uL^{-1} kanamycin. Colonies were grown in terrific broth (TB) with 50 ng uL^{-1} kanamycin and stored as glycerol stocks at -80^{o}C. The correct insertion of the hAR gene was verified by DNA sequencing.

Protein Purification. AdhD from the hyperthermophilic archaea *Pyrococcus furiosus* was expressed and purified as previously described [68]. hAR was expressed and purified as follows. Following transformation, the cells were induced at OD_{600} of 0.6 with 0.2mM IPTG. After incubating 18 hours at 37^{o}C with agitation, the cells were harvested by centrifugation. The pelleted cells were resuspended in one-tenth of the expression volume in 20 mM Tris-HCl, 150 mM NaCl, and 40 mM imidazole (pH 7.5) and supplemented with 1x HALT protease inhibitor cocktail (Thermo-Fisher). The cells were lysed by sonication with an 8 minute run time with pulses of 5 seconds with a 5 second rest between each pulse. The cell debris was pelleted by centrifugation at 15,000xg for 30 minutes. The hAR was purified from the clarified lysate using a HisTrap column (GE Healthcare) on a GE ÄKTA FPLC. The fractions containing hAR, (verified by SDS-PAGE) were pooled and concentrated using Amicon (EMD Millipore) centrifugal filters with a 30 kDa MWCO. Protein stocks were stored at 4^{o}C.

Protein Concentration. Concentrations were determined by UV absorbance at 280 nm and the BCA total protein assay (Macro assay: 1-0.025 mg mL^{-1}; Micro assay: 0.05-0.0005 mg mL^{-1}). Absorbance measurements were conducted on a SpectraMax M2 spectrophotometer (Molecular Devices, Sunnyvale, CA). Extinction coefficients for AdhD (ε_{280} = 1.97 mL mg^{-1} cm^{-1}) and hAR (ε_{280} = 1.1 mL mg^{-1} cm^{-1}) were measured experimentally. Preparation of standards for the BCA assays and protein samples for extinction coefficient measurements are described in the Supplementary Information (Section 2.8).

Activity Assay. The 2,3-butanediol oxidation activity of AdhD and DL-glyceraldehyde reduction activity of hAR were measured using spectrophotometric assays under saturation conditions. NAD^+ and NADPH were used as cofactors for AdhD and hAR, respectively. For AdhD, the absorbance at 340 nm (tracking NAD^+ reduction) was measured at 45°C with final concentrations of reaction buffer (glycine, pH 8.8), substrate and cofactor of 50 mM, 100 mM, and 1 mM, respectively. For hAR, the absorbance at 340 nm (tracking NADPH oxidation) was followed for reactions at 25°C with concentrations of reaction buffer (sodium phosphate, pH 7.0), substrate and cofactor of 100 mM, 100 mM, and 0.5 mM, respectively. Raw absorbance change was converted to specific activity using enzyme concentration and cofactor extinction coefficient (ε_{340nm} = 6.22x10^3 cm^{-1} M^{-1}).

Adsorption Isotherms. Silica particles were suspended in 20 mM sodium cacodylate buffer pH 5.0 (AdhD) or pH 6.9 (hAR) to achieve a concentration of 12 mg mL^{-1}. Equal parts of protein solution and silica suspension were mixed. Protein concentrations of 0.1-6 mg mL^{-1}were achieved by diluting with 20 mM Tris pH 7.5. Final pH resulted in 5.7 for AdhD and 7.2 for hAR. The samples were rotated on a rotisserie shaker for 16 hours at room temperature. Supernatants were collected and surface coverage was calculated as described previously [17].

Desorption. After removal of the supernatant, the particle pellet was resuspended in 0.8 mL of 10 mM sodium cacodylate buffer pH 5.0 (AdhD) or pH 6.9 (hAR). Samples were weighed to determine the particle loss over time. A solution density of 1.02 g cm^{-3} was used to determine the resuspension volume. After resuspension, the samples were incubated on a rotisserie shaker for 30 minutes. Then, supernatant was collected in the same as in the adsorption experiments. Resuspension was repeated for a total of 10 supernatants, from which a desorption curve was obtained. It was assumed that by the third resuspension cycle all of the protein had interacted with the particles, and these samples were used for CD and kinetic activity evaluation.

Circular Dichroism. A Jasco J-815 CD spectrometer (Jasco, Inc., Easton, MA) equipped with a Peltier junction temperature control was calibrated with 0.06% d-10-camphorsulfonate solution and used for far-UV CD measurements. Quartz cuvettes with path lengths of 0.01, 0.02, 0.05, or 0.1 cm were used. Protein solutions and protein-particle mixtures were measured using buffer or silica blanks, respectively, for subtraction of the baseline signal. Measurements were taken from 185 to 240 nm with a 0.1 nm interval, 1 nm bandwidth, 8 second response time, and scanning speed of 50 nm min^{-1}. For desorbed protein structure, the 0.1 cm cuvette was used, and the scan was cut off at 200 nm due to buffer interference. For each sample, 3 accumulations were measured and averaged. Raw CD signal (θ) was converted to Mean Residue Ellipticity (MRE) using the equation:

$$[\theta]_{MRE} = \frac{\theta}{10 * C_r * l} \qquad (1)$$

where C_r is the protein concentration (M*residue number) and l is the cuvette path length (cm).

Measurement of Adsorbed Protein Structure. The pellets from the adsorption isotherm were resuspended with gentle pipetting using a 1:1 mixture of 20 mM Tris-HCl pH 7.5 and 20 mM sodium cacodylate pH 5.0 (AdhD) or pH 6.9 (hAR). An aliquot was removed for CD assessment,

and the rest of the solution was pelleted through centrifugation (as described above) and supernatant concentration measured. The CD spectra of the supernatant were also recorded. Using the known amount of adsorbed protein, concentration in the resuspended pellet was determined. Using the MRE signals of the resuspended pellet ($[\theta]_{pell}$) and supernatant ($[\theta]_{SN}$), and the fraction of total protein concentration in the supernatant (χ_{SN}), the adsorbed protein structure was calculated using:

$$[\theta]_{Ads} = \frac{[\theta]_{pell} - \chi_{SN} * [\theta]_{SN}}{1 - \chi_{SN}} \qquad (2)$$

Deconvolutions. The CD spectra were deconvoluted using the CD Pro software package [71]. With each deconvolution algorithm (Continll, Selcon3, and Cdstr), 3 different reference sets were applied: SP37, SPD42, and SMP50. The average across all 3 algorithms and 3 bases are used to estimate the helical, sheet, and disordered content of each sample. The α-helix and β-sheet content is reported as the sum of the distorted and regular classes.

Electrophoretic Mobility. A Malvern Zetasizer Nano-ZS was used to measure particle size distribution and zeta potential of the silica particle suspensions in the pH = 5.7 and pH = 7.2 Tris/cacodylate buffers, or protein-silica mixtures. A 50 mW laser operating at a wavelength of 532 nm was used. Scattering intensities were recorded at a 90^{o} angle. A clear, disposable zeta cell was used for zeta potential measurements. All measurements were performed at 25^{o}C.

2.4. Results

Structural Characterization of Model System. Two homologous AKR superfamily members, AdhD and hAR, were chosen due to their similar secondary structures and different intrinsic structural stabilities. The sequence alignment (ClustalW2, EBI; Figure 2-1A) and ribbon structures (Figure 2-1B) show that while there is low sequence homology (<30%) between the

proteins, the tertiary structures are very comparable. Overlaying the CD spectra for both proteins more clearly demonstrates these similarities (Figure 2-1C). The high degree of spectral overlap indicates similar proportions of α-helical and β-sheet content. The fraction of secondary structure assigned to various domains from primary sequence predictions, the homology model (AdhD) or crystal structure (hAR; PDB: 2ACQ), and deconvolution of CD spectra are tabulated in Table 2-1. For both proteins, the fractions of secondary structure assigned to the helix and sheet domains are similar between the sequence prediction and homology model, but there is a discrepancy compared to experimental deconvolution values. This discrepancy is explained further below. However, the similarity in each secondary structure domain of the two proteins, with all three enumeration methods, is obvious from the table. The CD-based method was used as the principle experimental tool to assess relative changes in secondary structure. While the CD data demonstrate the similar structures of the proteins, the significant difference in structural stability is demonstrated by the melting curve shown in Figure S2-2, where the CD signal at 222nm (indicative of helical content) is measured over a thermal excursion from 25 to 95^{o}C. The curve shows that hAR loses a considerable amount of helical structure, while AdhD is minimally affected and no noticeable unfolding occurs below 95^{o}C.

Adsorption Behavior. The surface coverage of protein molecules adsorbed to the nanoparticles following a 16 hour isothermal incubation period is plotted against the equilibrium (supernatant) concentration (Figure 2-2). For both proteins, there are three well-defined regions: a rising linear portion, a transition region, and a maximum coverage plateau. At least one point from each of these regions is represented in subsequent data sets (letters in Figure 2-2 indicate these coverages). The adsorption data are described using the Langmuir adsorption isotherm defined as:

$$\Gamma = \frac{\Gamma_{max} C_{eq}}{K + C_{eq}} \quad (3)$$

where Γ is surface coverage, Γ_{max} is plateau surface coverage, C_{eq} is equilibrium protein concentration, and K is the apparent dissociation constant. Although assumptions underlying the Langmuirian model are not all necessarily appropriate for the adsorption of complex biomacromolecules (absence of conformational change and lateral interaction on the surface), the model describes this high-affinity protein-surface interaction well. The maximum surface coverage and affinity obtained from this fit are 1.68 mg m^{-2} and 0.50 mg mL^{-1} for AdhD, and 2.40 mg m^{-2} and 0.35 mg mL^{-1} for hAR, respectively. The lower affinity coefficient and higher maximum surface coverage of hAR, as compared to AdhD, indicate an increased affinity and adsorbed amount. Based on the molecular volume of each protein, theoretical surface coverages of 2.20 and 2.26 mg m^{-2} for AdhD and hAR, respectively, were obtained. In order to account for the packing of molecules on the surface, the Random Sequential Adsorption (RSA) [72] packing density (Θ=0.547) was multiplied by the total surface area of the particles to obtain the available surface area [73]. Since these calculations only account for size and not intermolecular interactions, the variance from experimental values is not concerning.

Adsorbed Protein Structure. Figure S2-3 shows the CD spectra of the different populations of proteins following surface interaction. A combination of these spectra was used to calculate adsorbed protein spectra. Figure 2-3 shows the adsorbed spectra for 5 different coverages for AdhD (Figure 2-3A) and hAR (Figure 2-3B). Two important conclusions emerge from these plots: first, for both proteins, the adsorption induces a significant level of unfolding compared to native; and second, the adsorbed spectra do not vary significantly as a function of surface coverage. To further compare the level of unfolding that occurs upon adsorption, all spectra were deconvoluted and the results can be seen in Figure 2-3C. The tabulation of these results

can be found in Table S2-2. The results show that both surface-bound proteins converge on similar α-helical (~0.06) and β-sheet (~0.35) content.

Desorption Behavior. The pellets obtained from the protein-particle mixtures were resuspended in fresh buffer to induce desorption. Previously, eluents such as morpholine [9] or dodeclytrimethylammonium bromide [53] were used to desorb bound proteins. In this study, we relied on the protein concentration gradient between the surface and bulk as the driving force for desorption. Introducing fresh buffer creates a transient difference in chemical potential ($\Delta\mu_s$) at the interface, which is then eliminated by spontaneous desorption. Following resuspension and incubation of the particles, the supernatant protein concentration was measured, which represents the desorbed amount. This sequence of resuspension and supernatant collection was repeated for 10 cycles for each protein (Figure 2-4A and Figure 2-4B). Data with varying protein:particle ratios were collected to assess the effect of coverage on desorption. The most striking difference in behavior between the two proteins is that the desorbed amount is affected by surface coverage much more significantly for hAR (Figure 2-4B) than the AdhD (Figure 2-4A). For AdhD, there is only a slight decrease in desorbed amount as coverage decreases, while for hAR, desorbed amount varies by over an order of magnitude for the lowest coverage shown, 0.08 mg m^{-2}, than for coverages above 0.52 mg m^{-2}. This indicates the propensity to desorb is decreased when fewer proteins coat the surface. A more subtle difference between the two desorption curves is that while desorbed amount levels off after the third cycle for hAR, this decreases continuously from cycle-to-cycle for AdhD. This indicates that the arrangement of particles for hAR reaches a steady state value earlier in the experiment, while for AdhD a possible redistribution on the surface manifests as a variability of the desorbed amount from cycle-to-cycle. Also, because elutability is expected to increase with molecular weight [59], the higher concentration values of

hAR in the supernatant after cycle 5 are consistent with this hypothesis (MW_{hAR}=37.2 kDa, MW_{AdhD}=31.9 kDa).

To adsorption/desorption reversibility, surface coverage following each rinse cycle is calculated and desorption isotherms are created, as shown in Figure 2-4C (AdhD) and 4D (hAR). In these figures, the lines represent the Langmuir fits of the adsorbed data (solid line) and desorbed data (dashed line). For AdhD, all six desorbed data sets are used for the Langmuir fit, as each group follows similar trends. This desorption curve in Figure 2-4C varies distinctly from the adsorption isotherm. For reversible adsorption, the ascending and descending branches of the isotherm must overlap at all values of C_{eq}. Therefore, our results indicate irreversible adsorption, and also coverage-dependent desorption (namely a path-dependent hysteresis of desorption). Conversely, two desorbed populations are found for hAR: at higher coverages (corresponding to transition and plateau values), a single Langmuirian desorption curve can be fit to all the data sets. As before, this desorption curve (Figure 2-4D) deviates significantly from the adsorption isotherm, indicating non-reversible adsorption. At low coverages (below 0.53 mg m^{-2}), two data sets reside in a different desorption regime as seen from their position relative to the Langmuir desorption curve. Interestingly, these data sets align closely with the Langmuir adsorption curve.

Desorbed Protein Characterization. To characterize secondary structure of the desorbed protein, far-UV CD spectra were taken from the third resuspension cycle. Native and desorbed protein spectra are shown in Figure 2-5. Three different coverages (corresponding to the plateau, transition and rising portions of the adsorption curve) are shown for the desorbed protein. The results are consistent with the previously described desorption curves: for AdhD (Figure 2-5A), little variation exists for desorbed protein structure with coverage, while for hAR (Figure 2-5B), the structure at lower coverages is severely perturbed compared to the higher coverages. The

results also show that all desorbed samples are slightly less structured than native for AdhD, while there is practically no difference between the high-coverage desorbed spectra and native hAR.

Activity assays were also performed on the same desorbed protein populations. The 2,3-butanediol oxidation activity of AdhD using NAD^+ cofactor and the DL-glyceraldehyde reduction activity of hAR using NADPH as cofactor were measured. The results of the kinetic assays are shown as percent of native activity in Figure 2-6. The specific activities are also reported in Table S2-3. These activity results correlate well with the secondary structure characterization. For AdhD, all desorbed protein, independent of surface coverage, lose ~35% native activity. In contrast, for hAR, the four high-coverage samples, which were grouped together earlier based on lack of secondary structural modification upon desorption, have no apparent activity loss upon desorption. However, the lower coverage samples, which were found to be severely perturbed by CD, show ~80% activity loss.

2.5. Discussion

Because proteins are naturally surface-active, adsorption can act as a catalyst to induce structural alteration, activity loss, or aggregation. Preventing such undesired surface-induced effects requires a fundamental understanding of the role of intrinsic protein parameters in adsorption behavior. Such knowledge is especially relevant in the pharmaceutical industry, where biologically-active therapeutic agents contact numerous surfaces during manufacturing, storage and delivery. During drug development, extensive effort is dedicated to improve the stability of such proteins, as various types of degradation pathways compromise their safety and efficacy. Although surface adsorption is not traditionally considered among the most common causes for physical instability, this phenomenon has been documented as a catalyst for denaturation [74].

Designing greater stability into proteins is thought to be a key strategy to mitigate such surface effects [75, 76].

It has long been recognized that a protein's structural stability influences its interfacial behavior, as the presence of a surface can disrupt intermolecular forces and render the protein susceptible to adsorption-induced conformational changes. In previous studies, this role of thermostability has been studied using engineered stability variants. Although using point mutations allows very specific changes to artificially stabilize (or destabilize) the protein without significantly changing its tertiary structure, we believe applying these systems in adsorption studies have inherent limitations. Only a limited range of thermostabilities can be studied and the approach used to alter stability often changes protein topology. Along these lines, artificially stabilized mutants may have other attributes that would not be favored in naturally evolved systems. To overcome these limitations, we assess the role of thermostability using naturally-evolved homologs. Additionally, we significantly expand the range of surface coverages previously explored.

As shown in Figure 2-1, the use of AdhD and hAR is a fitting model system for the study of the effect of naturally-occurring stability. These two proteins have similar tertiary structures but vastly different thermostabilities: hAR loses approximately half of its helical content at 57ºC, while AdhD is practically unaffected even at 95ºC. Regarding structural similarity of the proteins, it must be noted that Table 2-1 shows some discrepancies between secondary structure fractions determined theoretically from sequence prediction algorithms and direct CD measurement followed by spectral deconvolution. Although the two approaches result in similar trends in distribution of secondary structure, the CD-derived results are lower than the theoretical values. This is likely due to the inherent limitations of deconvolution algorithms used to quantify secondary structure [77]. Although such issues have been documented, CD remains a powerful

tool for evaluating comparative structural changes [78, 79] and was used here to examine changes in protein structure upon adsorption/desorption.

The difference in thermal stabilities of the two enzymes could be due to many factors. One possible explanation is that since AdhD has a more compact structure, there is more potential for close-range interactions that will stabilize its conformation. Another contributing factor could be the fraction of amino acids assigned to different secondary structure motifs. For example, AdhD and hAR have 118 and 112 amino acids involved in alpha-helices, respectively. However, because AdhD has an overall lower residue count than hAR this corresponds to 42% amino acids assigned to helices (vs. 34% for hAR). This means that a larger fraction of AdhD is made of a motif that contains a high number of hydrogen-bonds per amino acid, which could translate into increased intrinsic thermal stability.

In this study, we chose hydrophilic, unmodified silicon dioxide nanoparticles as the surface for several reasons. On hydrophilic surfaces, in the absence of strong electrostatic forces, protein stability is a key parameters that determines surface activity, as structural rearrangement is the main entropic driving force favoring adsorption [9, 80]. Colloidal silica also has favorable size, refractive index and light scattering properties, which render the particles CD-compatible, allowing *in-situ* structural analysis during adsorption. A final benefit of using colloidal system is our ability to target a wide range of surface coverages. This is a key parameter for our system of interest: proteins in delivery devices, where therapeutic concentration can vary by orders of magnitude. Thus, relevant coverages extend to the plateau region of the adsorption isotherm [17]. To minimize and normalize the effect of electrostatics, experiments were performed at a pH slightly greater than the isoelectric point of each protein, (AdhD pI 5.5, hAR pI 6.9; system pH 5.7 for AdhD and 7.2 for hAR) thus imparting a slight positive charge, which is consistent for

both proteins. The sodium cacodylate buffer (pK_a 6.3) was selected as its effective buffering range was compatible with the desired conditions. The silica particles used are negatively charged in both systems (pzc 3.0).

Our results shed new light on the relative role of structural stability in the different kinetic processes depicted in Figure 2-7. During surface attachment (Step I, Figure 2-7), the Langmuir curves in Figure 2-2 compare the surface affinity and adsorbed amounts of hAR and AdhD. Although we anticipated hAR to have a significantly greater affinity for the surface due to its lower thermostability, we find its K value is comparable to that of AdhD. Similarly, the differences in maximum surface coverage can most likely be attributed to the size difference between the proteins. Therefore, these results indicate structural stability does not play a significant role in protein-surface attachment. Figure 2-3 shows hAR and AdhD exhibit similar structural transitions on the surface (Step II, Figure 2-7). While both proteins undergo significant structural perturbation, the extent of α-helical loss and concomitant β-sheet formation is nearly identical. Although such disruption of intermolecular forces upon adsorption was expected for hAR, it is remarkable that the extremely thermostable AdhD undergoes such drastic conformational changes on a hydrophilic surface. Another interesting finding is the lack of correlation between surface coverage and structural denaturation for either protein (Figure 2-3C). Coverage-dependence of adsorption-induced unfolding has been reported previously [9, 11].

The results of this study reveal differences between hAR and AdhD during detachment and refolding (Steps III and IV, Figure 2-7). The desorption isotherms (Figure 2-4C and Figure 2-4D), and structural (Figure 2-5) and kinetic (Figure 2-6) characterization of the desorbed states indicate that while adsorption is irreversible in both cases, desorption follows different pathways for hAR and AdhD. For AdhD, some of the structural loss incurred upon adsorption is regained

upon detachment, however native-like refolding is not complete and ~35% enzymatic activity is lost. These findings re-emphasize the surprising effect adsorption-induced instabilities have on a thermally stable protein. AdhD also exhibits hysteresis in its refolding pathways as shown in Figure 2-4C. The pathways appear to be a function of surface coverage (possibly due to microscopic difference in surface arrangement). Although such examples of hysteresis are not commonly reported, Norde found similar behavior for albumin[81]. To schematically capture this incomplete refolding and pathway-dependent hysteresis behavior of AdhD, we believe that the single diagonal arrow in Figure 2-7 (Step V) can be replaced by multiple arrows representing different pathways. In contrast to AdhD, we find two distinct desorbed populations for hAR: at high coverages, the desorption isotherms follow a single pathway to native-like structural refolding and the desorbed protein has no activity loss. These results are unexpected due to the low thermal stability of hAR. At low coverages, desorbed hAR maintains high levels of structural loss and ~80% activity loss, which more closely represents our hypothesis. Unlike AdhD, no hysteresis is found. This coverage-dependent desorption behavior can be represented in Figure 2-7 by a combination of arrows both at Step III (desorption to a perturbed state, the low coverage case) and at Step V (desorption to a native-like state, the high coverage case).

Two driving forces are likely to govern the adsorption and structural unfolding of the proteins on the silica surface. One driving force is enthalpic-based, due to charge differences between the protein and silica. Although we have set the pH of the system to minimize overall point charge of the proteins, the surface charge profile of the two proteins vary, and localized charged patches can attribute to attractive/repulsive forces with the substrate. 3-D molecular models are shown in Figure S2-4 to illustrate the distribution of surface charge on both hAR and AdhD. Based on these diagrams, qualitative assessment of the differences between the two proteins can be made.

While both proteins have a few localized patches (both positive and negative) this charge distribution is generally homogeneous across the surface of the protein for hAR. By contrast, AdhD has more localized patches of both charges, with very few neutral areas. Specifically, positive patches seem to be more prevalent and larger for AdhD. The implication of these differences in surface charge distribution is discussed below. The other, entropic-based, driving force can be due to unfolding of secondary structure which increases conformational entropy of the protein molecule. This has been cited in previous studies [9]. Both proteins demonstrate a helix-to-sheet transition, which indicates that once the protein comes into proximity of an interface, less favorable intermolecular interactions, which constrain the molecular dynamics of the protein, are lost in favor of a more relaxed conformation and more possible surface-interactions.

One possible explanation for the adsorption-induced denaturation of the thermophilic AdhD is the presence of the aforementioned positive patches on the surface of the protein, as seen in Figure S2-4. Because the surface is negatively charged, strong Coulombic attraction would lead to high levels of surface affinity, with possibly concomitant structural unfolding as favorable attractive forces lead to new protein-surface bond formation.

Unlike previous results that indicate the existence of only two states: a native-like desorbed and a highly perturbed adsorbed state [17], we see evidence of a non-native like desorbed state. There is also indirect evidence that differentially unfolded states exist on the surface. This hypothesis is supported as follows. First, hAR desorbs in a coverage-dependent manner. This may be a consequence of two (or more) adsorbed protein populations: at low coverages, proteins arriving early have longer residence times, allowing the occupation of more optimal attachment sites, formation of stronger surface bonds, and lateral inter-molecular interactions. The detachment of

clusters would require greater free energy consumption, resulting in decreased desorbability [82]. Conversely, at high coverages, a greater packing density may inhibit optimal protein-surface interactions [83]. Second, previous results show differences in elutability, bound fraction and interfacial area in adsorbed proteins, indicating that the existence of a single adsorbed population is unlikely [62, 84]. Finally, evidence for molten globule-like adsorbed states is postulated by studies involving carbonic anhydrase [85], lysozyme [86], and human growth hormone [87]. Our results indicate that overall adsorption behavior of these homologous proteins on silica does not correlate strongly with thermostability. These results are surprising, as the structural stability of mutants has been previously hypothesized to strongly influence their surface affinity, degree of structural perturbation, and desorbability. The main difference in our study is that we assess a greater difference in thermostability, by using proteins with naturally evolved structures that have been optimized for their environment. As such, these homologs have similar topology and tertiary structure, but vastly different primary sequences. In contrast, stability mutants have similar primary and tertiary structure, but often different topologies. Both approaches introduce parameters into the system whose effect on adsorption behavior is unknown: for stability mutants, we hypothesize that altered topology may inhibit optimal protein/surface interaction, thus artificially reducing (or promoting) extent of surface-induced perturbation. However, with naturally-occurring homologs, we cannot be certain that observed adsorption behavior is not due to differences in specific amino acid and surface interactions (due to the differences in primary structure). We argue that although both systems have some limitations, the use of physiologically-relevant systems which allows a wider range of thermostabilities to be studied provides valuable insight which may have been previously overlooked.

We also find interesting differences in the desorption behaviour of hAR and AdhD. One explanation is that desorption is sensitive to structural stability because the same intermolecular forces which drive protein folding in solution will determine whether desorption is energetically more favourable. However, we cannot be sure that the observed differences are not protein-dependent. In their natural environments, we know that these proteins are cystolic and may fold with the help of chaperones. Furthermore, thermal stress causes irreversible unfolding in hAR while having no effect on AdhD. Therefore, other intrinsic parameters, such as primary sequence may be the dominant factor in determining desorption behaviour.

For more insight into the role of surface adsorption as a catalyst for protein destabilization, we compare the denaturing effects of the surface to other well–known stresses. Figure S2-5 shows the far-UV CD spectra of hAR following thermal, chemical and surface-induced stress. Thermal effects results in almost complete loss in secondary structure, while both surface- and chemically-induced stress cause only partial structural loss. Such differences are likely due to the probability of breaking the hydrogen bonds which maintain secondary structure in the presence of various disrupting forces [88]. Interestingly, thermal vs. surface-induced stress have a markedly different effect on AdhD: while extreme temperature excursions cause essentially no structural alteration, the surface is capable of irreversibly perturbing its structure.

To the best of our knowledge, this study marks the first time that naturally occurring stability variants have been evaluated for interfacial behavior, by studying their differences and interdependencies along each step of the adsorption lifecycle. Our results show that there is little correlation between a protein's thermostability, surface affinity, and susceptibility to surface-induced unfolding. Additionally, we show interesting desorption behavior between the proteins and the importance of surface coverage in determining refolding pathway. Our results reveal that

role of thermostability in interfacial behavior may be less dominant than previously thought while protein surface properties may be a more important determinant of this behavior. These conclusions shed some doubt on the notion that improving thermostability is the main way to reduce the effects of adsorption-induced changes of proteins.

2.6. Acknowledgements

Becton Dickinson provided financial assistance for this work. We are grateful for the laboratory-related assistance of Ms. Sara Chuang, the guidance of Dr. Elliot Campbell, and critical review by Mr. Kevin Dooley.

2.7. Figures and Legends

Figure 2-1 - Structural comparison between AdhD and hAR

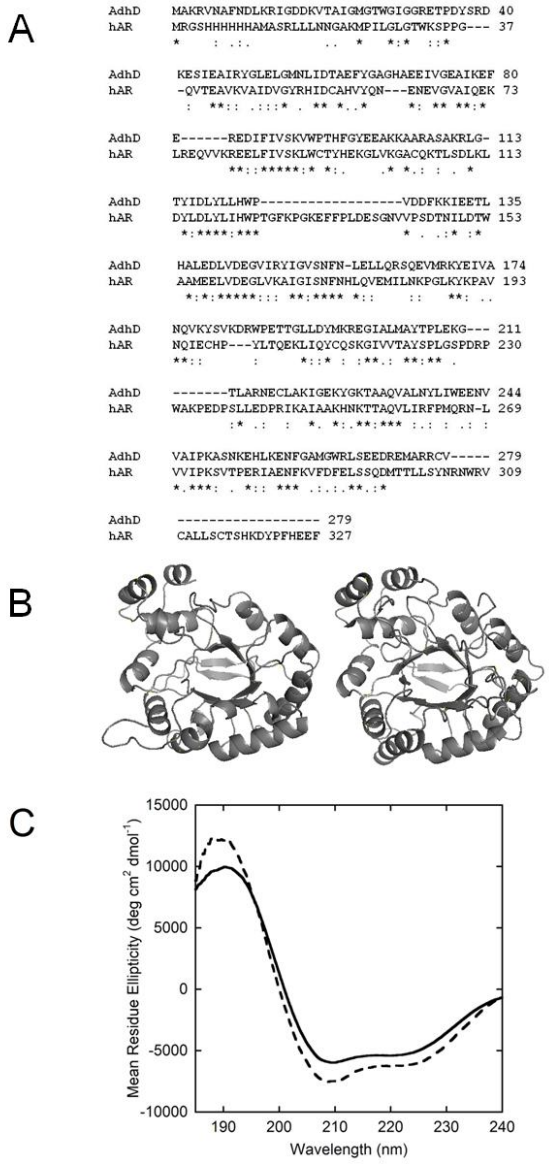

(A) Amino acid sequence alignment of AdhD and hAR showing < 30% sequence homology between the selected proteins; (B) 3-D homology model of AdhD (left) and crystal structure of hAR (PDB:2ACQ) (right) showing similarities in secondary and tertiary structure; (C) Far-UV CD spectra of native AdhD (——) and native hAR (– – –) quantitatively demonstrating the similarities in secondary structure between the two.

Figure 2-2 - Adsorption isotherms for AdhD and hAR

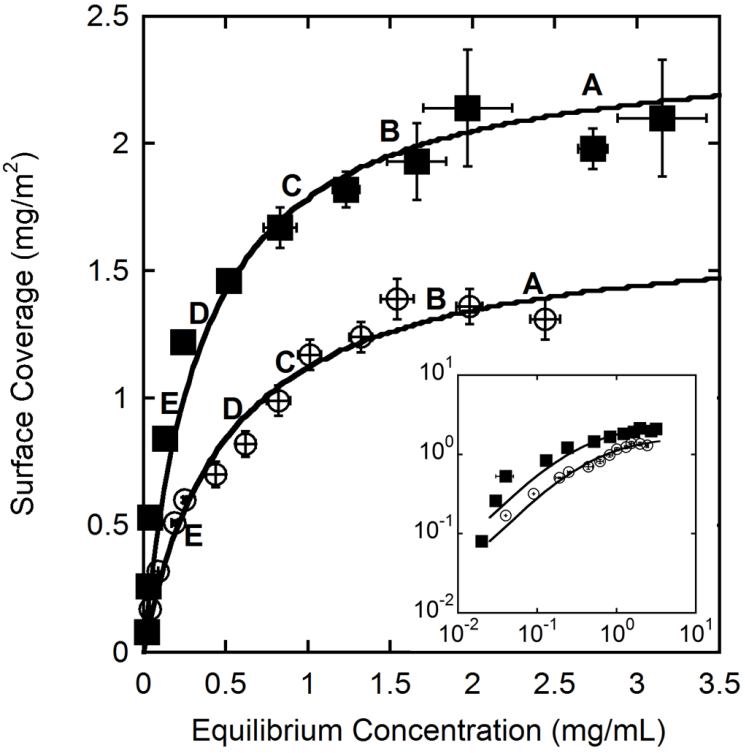

Adsorption isotherms for AdhD, ○ (K=0.50 mg mL^{-1}, Γ_{max} = 1.68 mg m^{-2}) and hAR, ■ (K=0.35 mg mL^{-1}, Γ_{max} = 2.40 mg m^{-2}) with least-squared fits to a Langmuir isotherm. Inset contains adsorption isotherms on logarithmic axes. Labels A-E indicate points selected for subsequent data sets. Error bars represent the standard deviation of three independent replicates. The inset provides a log-log plot of the data.

Figure 2-3 - Adsorbed spectra and deconvolutions for AdhD and hAR

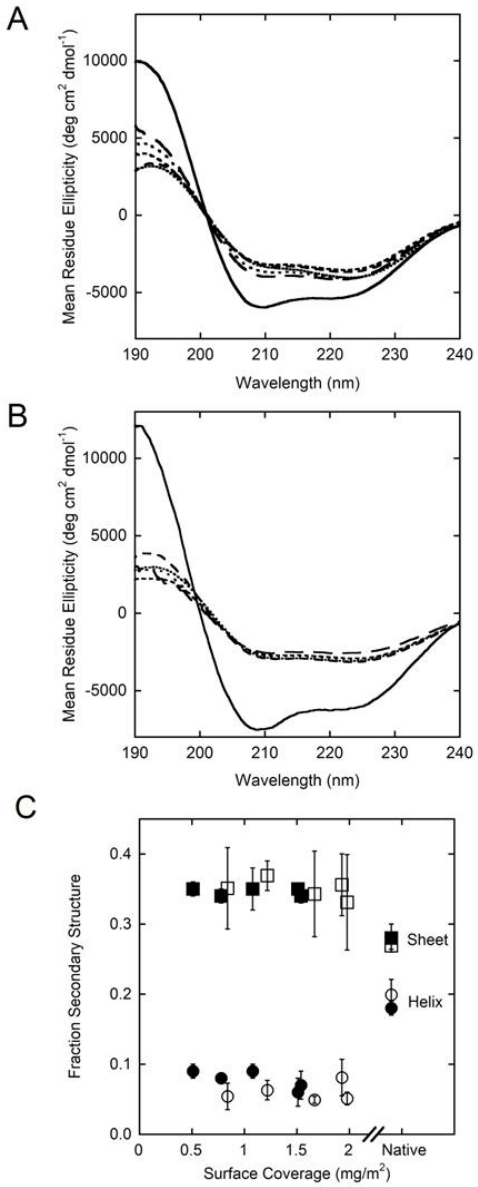

Adsorbed protein spectra for AdhD (A) and hAR (B) as compared to the native spectra (▬▬▬) of each protein. Starting with the highest surface coverage, the line types indicate (Surface coverage and C_{eq} follow each line type): ..... (AdhD: 1.54 mg m^{-2}, 2.44 mg mL^{-1}; hAR: 1.98 mg m^{-2}, 2.73 mg mL^{-1}), ••••••• (AdhD: 1.51 mg m^{-2}, 1.62 mg mL^{-1}; hAR: 1.93 mg m^{-2}, 1.66 mg mL^{-1}), ▬ ▬ ▬ (AdhD: 1.08 mg m^{-2}, 0.85 mg mL^{-1}; hAR: 1.67 mg m^{-2}, 0.83 mg mL^{-1}), ▬ ▬ ▬ (AdhD: 0.78 mg m^{-2}, 0.50 mg mL^{-1}; hAR: 1.22 mg m^{-2}, 0.24 mg mL^{-1}), and ▬▬ ▬▬ (AdhD: 0.51 mg m^{-2}, 0.24 mg mL^{-1}; hAR: 0.84 mg m^{-2}, 0.13 mg mL^{-1}); (C) Fraction of secondary structure that exists as α-helical (circle) and β-sheet (square) domains for AdhD (● and ■) and hAR (○ and □) for native protein and adsorbed protein.

Figure 2-4 - Desorption curves and desorption isotherms for AdhD and hAR

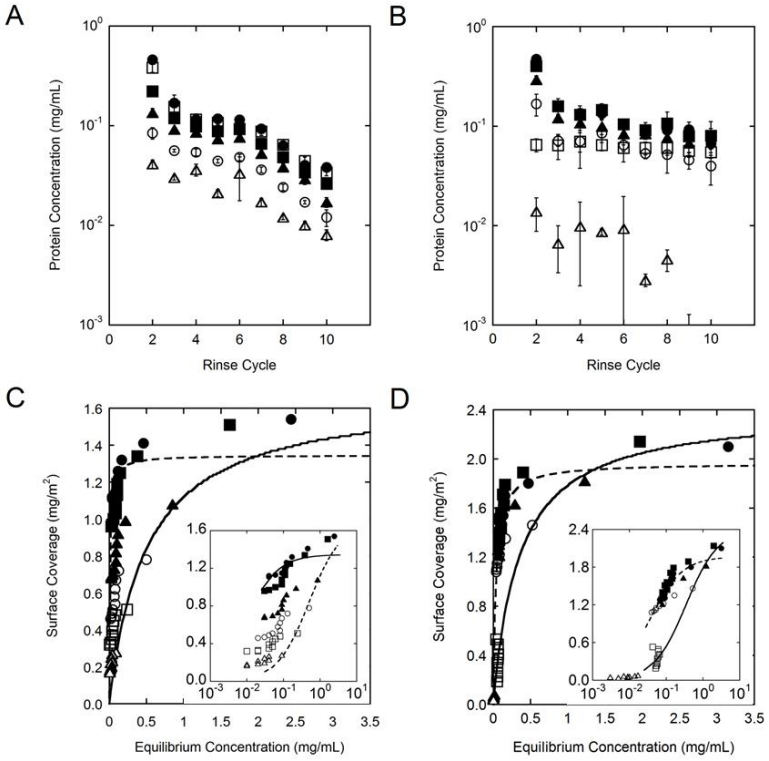

Desorbed protein concentration as a function of rinse cycle for (A) AdhD and (B) hAR. Data shown for rinse cycles 2-10. Protein:particle ratios corresponding to five different regions along the adsorption isotherm (as labeled A-E in Figure 2-2) were used (surface coverage and C_{eq} follow each sample). AdhD: ● Sample A: 1.4 mg m^{-2}, 1.9 mg mL^{-1}; ■ Sample B: 1.2 mg m^{-2}, 1.3 mg mL^{-1}; ▲ Sample C: 0.82 mg m^{-2}, 0.62 mg mL^{-1}; □ Sample D: 0.60 mg m^{-2}, 0.25 mg mL^{-1}; ○ Sample E: 0.32 mg m^{-2}, 0.09 mg mL^{-1}; hAR: ● Sample A: 2.1 mg m^{-2}, 3.2 mg mL^{-1}; ■ Sample B: 2.1 mg m^{-2}, 2.0 mg mL^{-1}; ▲ Sample C: 1.8 mg m^{-2}, 1.23 mg mL^{-1}; □ Sample D: 1.46 mg m^{-2}, 0.52 mg mL^{-1}; ○ Sample E: 0.53 mg m^{-2}, 0.04 mg mL^{-1}. Each point is the average of three distinct replicates and error bars represent their standard deviation. Not shown on the graphs is the limit of detection of each assay, as all concentration values shown are above this limit. Desorption isotherms are shown in (C) AdhD and (D) hAR. Data for all 10 cycles are depicted, and symbols are consistent with those used in A and B. The solid line represents the Langmuir fit for the adsorption isotherm data and the dashed line represents a Langmuir fit for the desorption data. Insets show the same data sets on a logarithmic x-axis.

Figure 2-5 - Desorbed protein CD spectra for AdhD and hAR

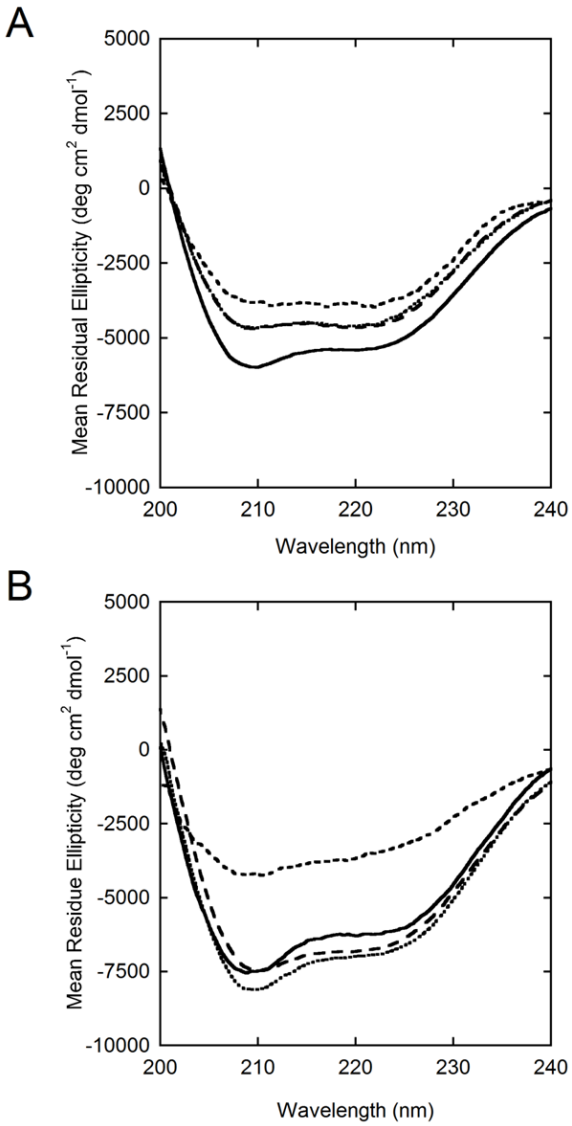

CD spectra of native protein (solid line) vs. desorbed protein (obtained from cycle 3 of the desorption experiments captured a surface coverages along the plateau value ..... , transition region ___ ___ and rising portion of the adsorption isotherm - - -) for (A) AdhD and (B)) hAR

Figure 2-6 - Desorbed protein kinetics for AdhD and hAR

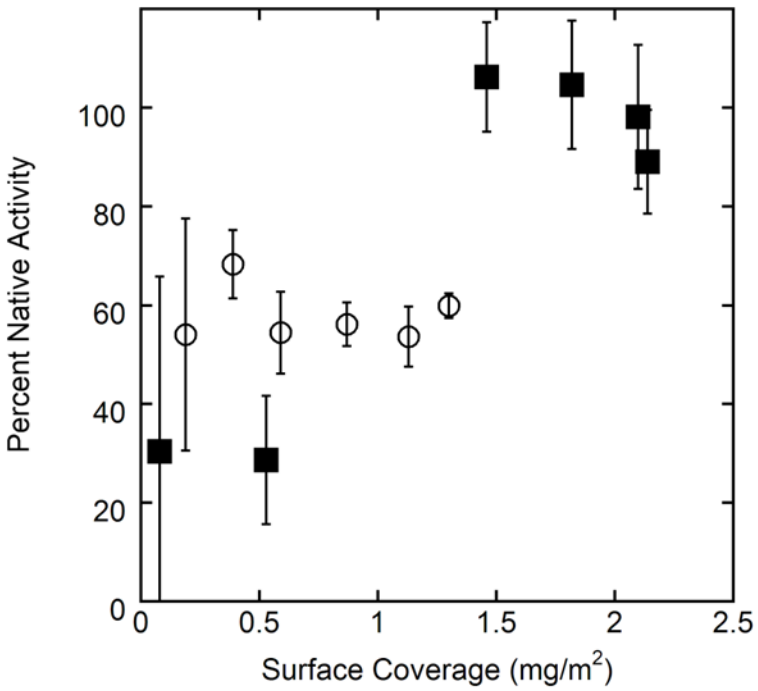

Kinetic data showing percent native activity for desorbed AdhD (○) and hAR (■) at various levels of surface coverage. Desorbed protein has been taken from the third rinse cycle of the desorption experiments. Error bars represent standard deviations of three independent samples. Coverages targeted are the same 5 data sets as have been used in Figure 2-4 and Figure 2-5, for direct comparison.

Figure 2-7 - Four-state adsorption/desorption model schematic

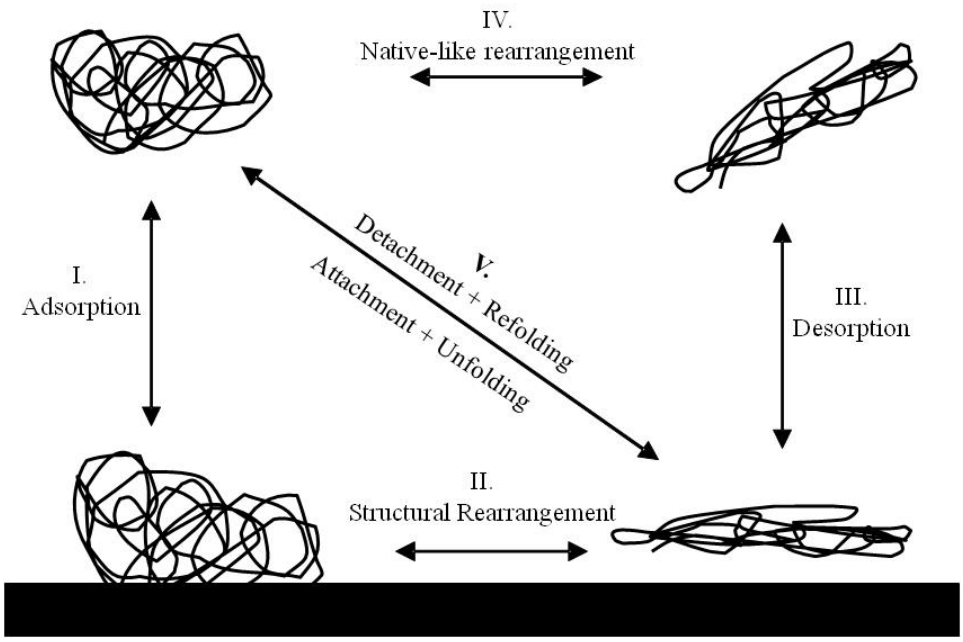

Classical 4-state kinetic model, representing the native state in bulk before adsorption, the adsorbed state before unfolding, followed by structural rearrangement while on the surface, desorption into bulk, and refolding into native-like state.

Table 2-1 - Secondary structure comparison between AdhD and hAR

	AdhD			hAR		
	Sequence Prediction[a]	**Homology Model[b]**	**CD[c]**	**Sequence Prediction[a]**	**Crystal Structure[d]**	**CD[c]**
Helix	0.41 (115)*	0.43 (118)	0.18	0.35 (112)	0.36 (119)	0.21
Sheet	0.14 (39)	0.14 (39)	0.28	0.13 (48)	0.12 (40)	0.27
Disordered	0.45 (125)	0.42 (115)	0.54	0.52 (154)	0.52 (169)	0.52

* Where applicable, the number of amino acids assigned to each domain is indicated in parentheses

[a]Predictions based on 6 different algorithms averaged together (JPred, Porter, PsiPred, Prof, SCRATCH, 3DJigsaw)

[b]Homology model obtained as previously described [22]

[c]Deconvolutions of CD Spectra performed using CDPro Software

[d]Crystal structure obtained from PDB file 2ACQ

2.8. Supplementary Information

Further Experimental Details:

Cloning. The following primers were used for the hAR cloning: The OE1_F primer was used with OE1_R to generate the first part of the gene, while OE2_F was used with the reverse primer OE2_R to generate the second part of the gene. The pieces were denatured, annealed ,and extended to yield the full-length hAR gene. This strategy introduced an *Nco*I restriction site (underlined in OE1F) and a *Hind*III restriction site (underlined in OE2R).

Table S2-1 - Oligonucleotide seuqences used for hAR cloning

Primer	Sequence
OE1_F	5'-AGCAGCCATGGCAAGCCGTCTCC-3'
OE1_R	5'-GGACACGTGGGCGGCAATGGAAGAGCTGGTGG-3'
OE2_F	5'-CCACCAGCTCTTCCATTGCCGCCCACGTGTCC-3'
OE2_R	5'-ATCGAAGCTTTCAAAACTCTTCATGGAAGG-3'

Protein Concentration. Standards for the BCA assays and protein samples for extinction coefficient measurements were made from purified lyophilized protein. 12 - 30 mL of purified protein were dialyzed against 2 L of 25 mM ammonium bicarbonate at 4^{o}C with buffer replacement every 8-12 hours. The dialyzed protein samples were then lyophilized for 36 hours. Pure lyophilized protein was weighed and resuspended to a known concentration.

Figure S2-1 - SWISS model output for AdhD and hAR

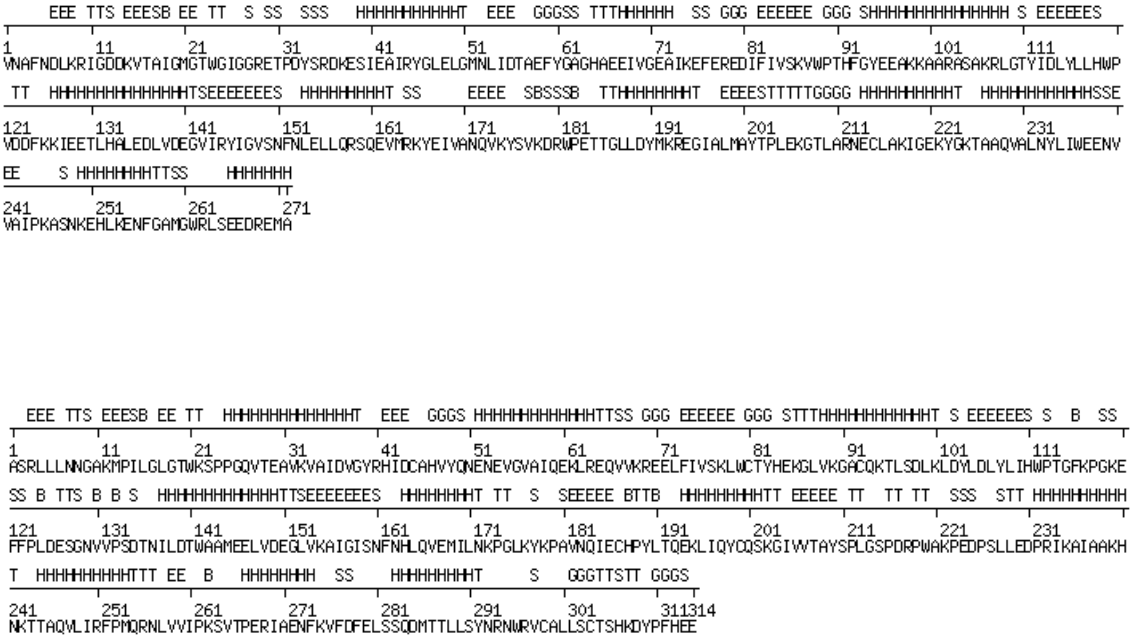

Secondary structure predictions generated by the SWISS model program for AdhD (top) and hAR (bottom) [89-91]

Figure S2-2 - Thermal denaturation curves for AdhD and hAR

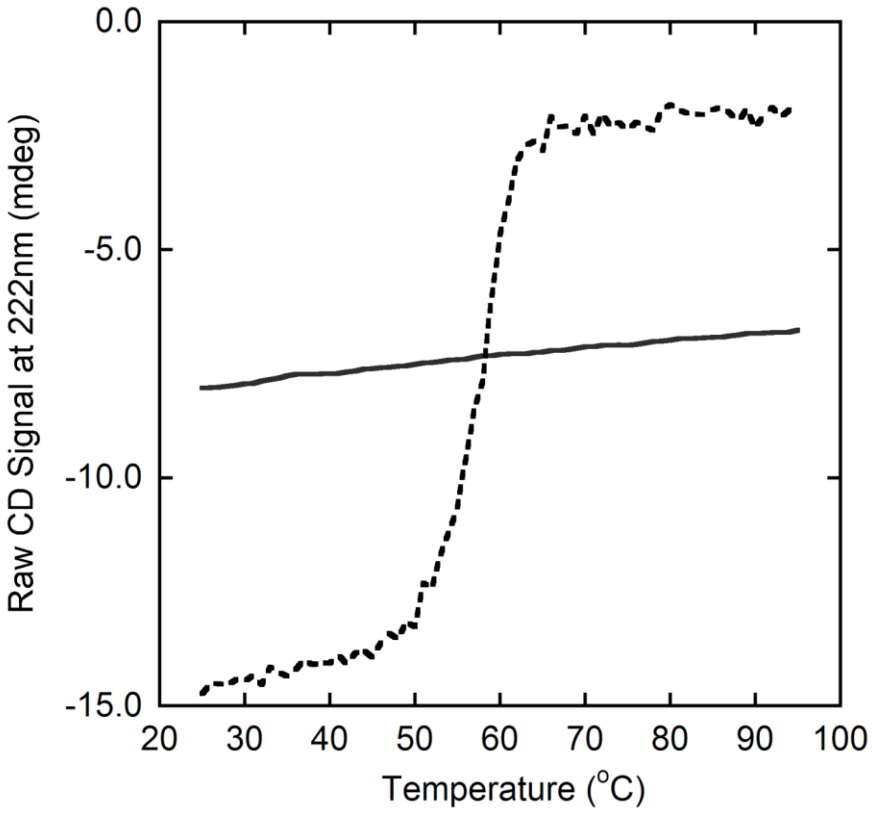

Melting curve of AdhD (solid line) and hAR (dashed line) as obtained by following the CD spectra of both proteins at 222nm between 25 and 95°C. Samples were run in 1mm cuvettes. Buffer used is 10mM sodium cacodylate buffer at pH=5 (AdhD) and pH=6.9 (hAR). Only hAR exhibits unfolding behavior under these conditions, and the midpoint temperature of a sigmoidal fit (T_m = 57°C) is assigned as the melting temperature of this protein.

Figure S2-3 - Spectra used for adsorbed structure calculations for AdhD and hAR

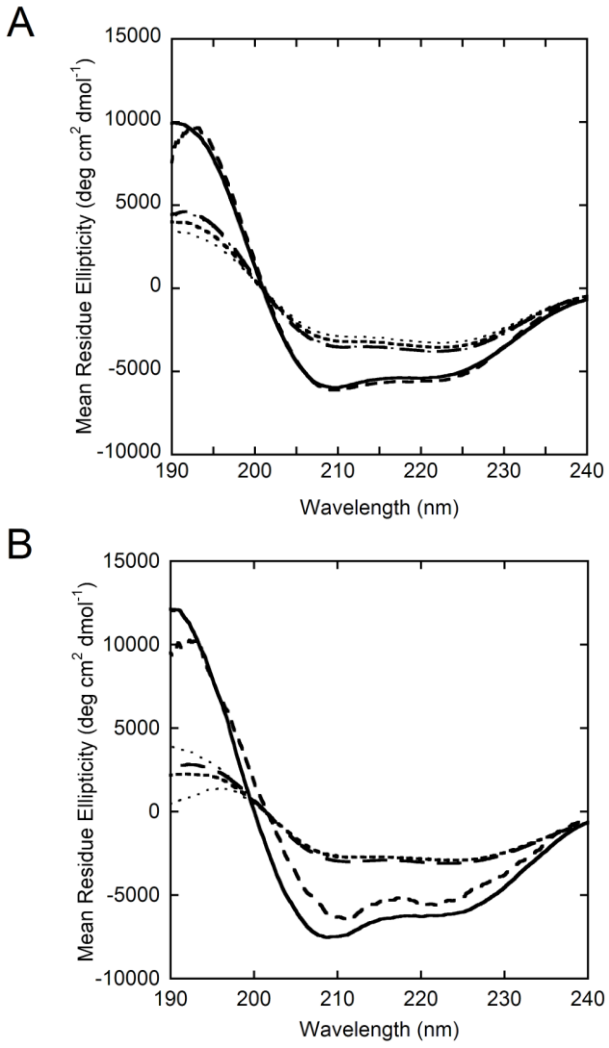

Spectra used for determining adsorbed protein structure for AdhD (A) and hAR (B). Spectra shown: native (▬▬▬), resuspended adsorbed protein-particle pellet (▬ ▬), supernatant from resuspended pellet (▬ ▬ ▬), adsorbed protein (▬ ▬ ▬ ▬), error in adsorbed spectrum (••••••••). Error bands are obtained by adding the standard deviations of three replicates to the average spectrum.

Figure S2-4 - Charge and hydrophobicity surface diagrams for AdhD and hAR

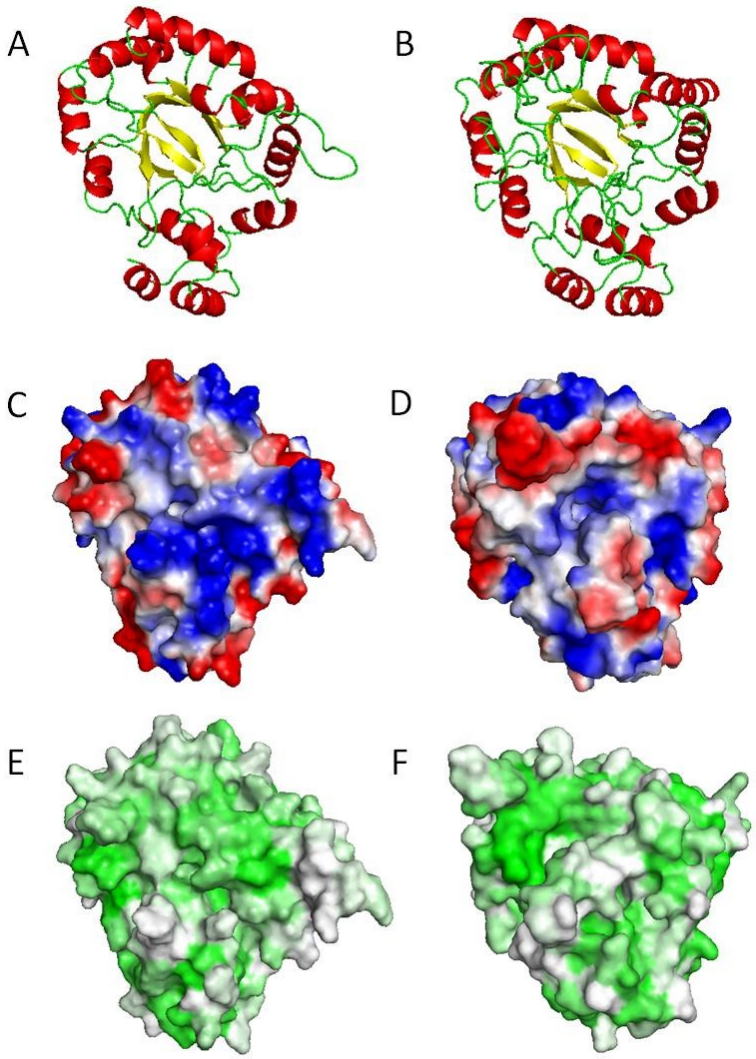

Cartoon diagrams for (A) AdhD and (B) hAR showing the similarities in secondary structure and surface representations of surface charge for (C) AdhD and (D) hAR and surface hydrophobicity for (E) AdhD and (F) hAR.

Figure S2-5 - Comparison of hAR spectra after denaturation by various means

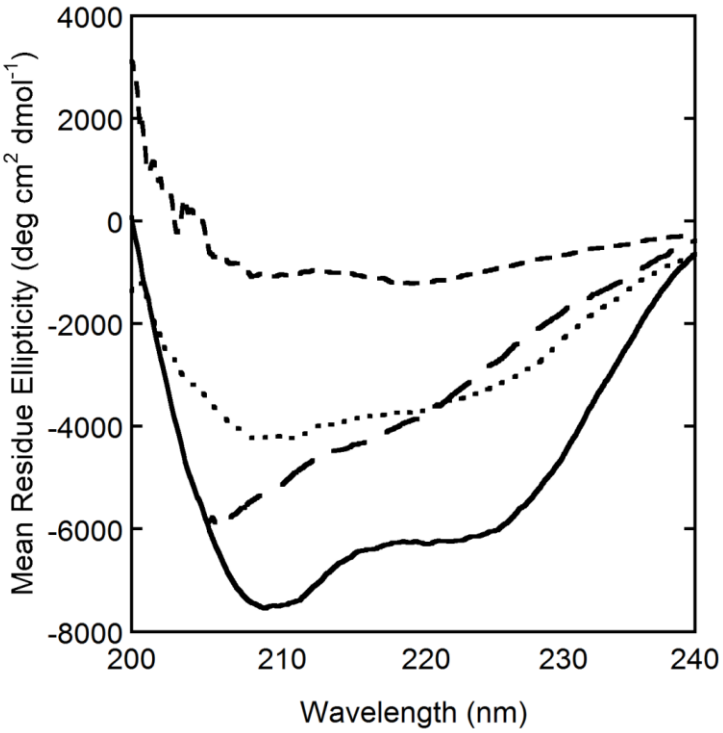

Far-UV CD spectra of haR in the native state (solid), following chemical denaturation by 6M GdHCl (▬ ▬), surface-induced denaturation, i.e. desorbed protein (••••••••) and following thermal denaturation upon heating to 95°C (▬ ▬ ▬ ▬).

Table S2-2 - Adsorbed spectra deconvolutions for AdhD and hAR

(A)

Surface Coverage (mg m^{-2})	Helix fraction	Sheet fraction	Random fraction
Native	0.20	0.27	0.51
1.98	0.05	0.33	0.49
1.93	0.08	0.36	0.47
1.67	0.05	0.34	0.50
1.22	0.06	0.37	0.52
0.84	0.05	0.35	0.48

(B)

Surface Coverage (mg m^{-2})	Helix	Sheet	Random
Native	0.18	0.28	0.50
1.54	0.07	0.34	0.53
1.51	0.06	0.35	0.51
1.08	0.09	0.35	0.49
0.78	0.08	0.34	0.52
0.51	0.09	0.35	0.52

Fraction of secondary structures of adsorbed protein spectra upon deconvolution of CD data for both AdhD (A) and hAR (B). This is a numerical representation of the data graphed in Figure 2-3.

Table S2-3 - Specific activities of desorbed AdhD and hAR

	Specific Activity (min^{-1})	
	AdhD	hAR
Published	60[a]	96[b]
Native	63	85
Point A	37 (1.30)	83 (2.10)
Point B	34 (1.13)	75 (2.14)
Point C	35 (0.87)	89 (1.82)
Point D	34 (0.59)	90 (1.46)
Point E	43 (0.39)	24 (0.53)
Point F	34 (0.19)	26 (0.08)

Specific activity values for AdhD (left column) and hAR (right column) of native protein and desorbed protein at various coverages. Surface coverage in mg m^{-2} is given in parentheses for each point. Values from literature for both [a]AdhD [68] and [b]hAR [92] are also reported.

3. Immobilization via Periplasmic Expression for Whole-cell Biocatalysis

3.1. Characterization of Carbonic Anhydrase-bearing Biocatalysts

Note: A version of this chapter entitled "Periplasmic expression of carbonic anhydrase in Escherichia coli: a new biocatalyst for CO2 hydration." is published in *Biotechnology and Bioengineering* (2013), volume 110, issue 7, pages 1865-1873, with co-authors Alissa Ah-Hyung Park and Scott Banta.

TNP designed and performed all experiments, analyzed the data, and wrote the manuscript.

3.1.1. Abstract

Carbonic anhydrase is a valuable and efficient catalyst for CO_2 hydration. Most often the free enzyme is employed which complicates catalyst recycling, and can increase cost due to the need for protein purification. Immobilization of the enzyme may address these shortcomings. Here we report the development of whole-cell biocatalysts for CO_2 hydration via periplasmic expression of two forms of carbonic anhydrase in *Escherichia coli* using two different targeting sequences. The enzymatic turnover numbers (k_{cat}) and catalytic efficiencies (k_{cat}/K_M) were decreased by an order of magnitude as compared to the free soluble enzyme, indicating the introduction of transport limitations. However, the thermal stabilities were improved for most configurations (>88% activity retention up to 95^{o}C for 3 of 4 whole-cell biocatalysts), operational stabilities were more than satisfactory (100% retention after 24 hours of use for all 4 whole-cell biocatalysts), and CO_2 hydration was significantly enhanced relative to the uncatalyzed reaction (~50-70% increase in $CaCO_3$ precipitate formed). A significant advantage of the whole-cell approach is that protein purification is no longer necessary, and the cells can be easily separated and recycled in future applications including biofuel production, biosensors, and carbon capture and storage.

3.1.2. Introduction

Carbonic anhydrases (CA; EC 4.2.1.1) are well-studied Zn-binding metalloenzymes that are nearly ubiquitous in nature [39, 42]. Among the fastest known enzymes, their primary catalytic function is the reversible hydration of carbon dioxide (CO_2) into bicarbonate (HCO_3^-) and carbonate (CO_3^{-2}) ions, as shown below [93]:

$$CO_2 + H_2O \rightleftharpoons H_2CO_3 \qquad (1)$$

$$H_2CO_3 \rightleftharpoons HCO_3^- + H^+ \qquad (2)$$

$$HCO_3^- \rightleftharpoons CO_3^{-2} + H^+ \qquad (3)$$

For most organisms, these reactions are important in complex processes such as respiration and photosynthesis [94]. However, the uncatalyzed reaction rate of this conversion is slow and the amount of bicarbonate ions formed is not enough to match the needs of the organism. Also, the accumulation of CO_2 within the organism is detrimental to its health [95]. Fortunately, carbonic anhydrases are able to catalyze this reaction with turnover rates ranging from 10^4-10^7 sec^{-1} [42] via the pathway shown below [41]:

$$EZnH_2O \rightleftharpoons EZnOH^- + H^+ \ (4)$$

$$EZnOH^- + CO_2 \rightleftharpoons EZnHCO_3^- \qquad (5)$$

$$EZnHCO_3^- + H_2O \rightleftharpoons EZnH_2O + HCO_3^- \ (6)$$

$$HCO_3^- \rightleftharpoons CO_3^{-2} + H^+ \qquad (3)$$

These enzymes have been organized into 3 main classes: α, β, and γ [96]. The α-class is comprised of all CAs found in mammals, including the 10 human isoforms that have been identified. The β-class, also called "plant-type carbonic anhydrases", consists of enzymes isolated and identified mainly from plants, but also from several bacterial and archaeal species. And, the γ-class, thought to be evolutionarily the oldest, is fairly unstudied since only one form

has been isolated and purified [97]. Additionally, δ- [98], ε- [99], and ζ-classes [100] have also been identified, but remain poorly studied as yet.

Previous work on CA has focused on the catalytic mechanism of the enzymes [39, 41, 101-106]. Other research pertains to the activators and inhibitors of CA [107-109] and the potential use of CAs as therapeutics [110, 111]. Within the last decade, researchers have been interested in carbon capture mediated by CA [47, 112-114]. Other industrial applications for the enzymes include any process in which CO_2 hydration or fixation rates need to be increased, such as engineering photosynthesis [48], biofuel production [49], and electrochemical biosensors [50].

In this study, a β-class (Cab from *Methanobacterium thermoautotrophicum*; PDB: 1G5C) and a γ-class (Cam from *Methanosarcina thermophile*; PDB: 1THJ) CA were separately expressed in the periplasm of *Escherichia coli* for use as whole-cell biocatalysts for carbon dioxide hydration. The crystal structure of Cab was resolved in 2001 and showed that Cab naturally dimerizes. Each monomer consists of a parallel β-sheet core surrounded by α-helices [115]. The structure and stability of Cab were characterized previously and the enzyme was found to be the most stable form of carbonic anhydrase ever isolated, but also among the slowest with turnover rates on the order of 10^4 sec^{-1} [42, 44]. The crystal structure of Cam was also determined previously and showed that the enzyme forms homotrimers which oligomerize into hexamers. The monomeric structure consists of a left-handed β-helix, a structure unlike any other identified form of carbonic anhydrase [42, 116]. Cam has also been previously characterized and also showed low activity relative to other carbonic anhydrases. It is natively expressed in the periplasm of the archaeabacteria from which it is derived [46, 51, 117]. This familiarity with the periplasmic space is beneficial since the likelihood of inactivation or inhibition due to the

oxidative environment found in the periplasm is reduced. The crystal structures of both enzymes can be seen in Figure 3-1.

The goal of this research was to characterize whole-cell biocatalysts containing periplasmically expressed CA. We hypothesized that the outer cell membrane of *E. coli* would present a transport barrier for the flux of reactant and product across the outer membrane. This would reduce the overall reaction rate, but should not affect the catalytic activity of the enzymes. Based on prior research [6], we also presumed that this immobilization technique would result in stabilization of the catalysts. Lastly, we compared the performance of the whole cell catalysts in a potential carbon capture and storage application.

3.1.3. Materials and Methods

Materials. Oligonucelotides were obtained from Integrated DNA Technologies (Coralville, IA). Restriction enzymes and T4 DNA Ligase were from New England Biolabs (Ipswich, MA). All other chemicals were purchased from Sigma-Aldrich (St. Louis, MO), unless otherwise indicated.

Cloning. The genes for Cab and Cam were synthesized and subcloned into the pBSK (BlueScriptII) cloning vector by Epoch Life Science (Sugarland, TX). The nucleotide and amino acid sequences for the two proteins can be seen in Figure S3-1. The genes were then amplified from this plasmid using oligonucleotides TP05/TP09, and TP03/TP10 for Cab and Cam, respectively. The amplified inserts were digested using restriction enzymes NdeI/HindIII. The inserts were then ligated into similarly digested pET-24a expression vector (Novagen, Gibbstown, NJ) using T4 DNA Ligase. This vector attaches a 6xHis tag to the C-terminus of the desired protein. The constructs were electroporated into BLR(DE3) *E. coli* cells (Novagen) and selected on agar plates containing 50 μg/mL kanamycin. A similar procedure was used to clone Cab and Cam into the pBAD/gIIIA periplasmic expression vector (Invitrogen, Grand Island, NY)

using primers TP11/TP12 and TP42/TP14 respectively and restriction enzymes KpnI/HindIII for Cab and SacI/KpnI for Cam. This vector fuses the gIII periplasmic leader peptide to the N-terminus of the desired protein and a myc epitope and 6xHis tag to the C-terminus. These constructs were also electroporated into BLR(DE3) cells and selected on agar plates containing 50 μg/mL ampicillin. As an alternative periplasmic expression system, Cab and Cam were cloned into the pAK100 vector, which fuses the pelB periplasmic leader peptide to the N-terminus of the desired protein and a myc epitope to the C-terminus. This was accomplished using primers TP34/TP35 and TP36/TP37 respectively and the restriction enzyme SfiI. These constructs were electroporated into BLR(DE3) cells and selected on agar plates containing 35 μg/mL chloramphenicol. Due to poor expression levels from this vector, the fusions were then cloned into the pET-24a vector using primers TP38/TP39 and TP40/TP41 respectively with restriction enzymes NdeI/HindIII. All primer sequences can be found in Table S3-1.

Protein Expression and Purification. Proteins were expressed at 37^{o}C in 1 L of Terrific Broth (TB) supplemented with 1 mM $ZnCl_2$ and the appropriate antibiotic (Amp or Kan). All cultures were inoculated with 5 mL overnight cultures. Expression was induced at OD_{600}=0.6 by adding 0.02% L-arabinose (pBAD) or 200 μM IPTG (pET). After 4 hours of expression, the cells were pelleted via centrifugation at 3,000xg for 10 minutes. The cells were resuspended in 100 mL of 20 mM Tris-HCl, 150 mM NaCl, and 40 mM imidazole at pH 7.4. Some cultures were stored at 4^{o}C for use as whole-cell biocatalysts. For purification, the resuspended cells were lysed by sonication for a total of 8 minutes. The lysate was clarified via centrifugation at 15,000xg for 30 minutes. The carbonic anhydrase was purified from the lysate using a HisTrap (GE Healthcare) column on a fast performance liquid chromatography (FPLC) system (GE). The protein was loaded and washed at 5 mL/min in binding buffer (20 mM Tris-HCl, 150 mM NaCl, 40 mM

imidazole, pH 7.4). Elution was achieved with a linear gradient of elution buffer (20 mM Tris-HCl, 150 mM NaCl, 500 mM imidazole, pH 7.4) over 20 column volumes. Fractions containing the protein were then pooled together and concentrated using an Amicon 10 kDa molecular weight cutoff (MWCO) centrifugal filter (Millipore, Billerica, MA). Protein concentrations were measured using the absorbance at 280 nm with extinction coefficients of 3013 M^{-1} cm^{-1} and 16735 M^{-1} cm^{-1} for Cab and Cam, respectively. These values represent the average between coefficients calculated based on the amino acid sequence as described previously [118] and using the ProtParam tool developed by the Swiss Institute of Bioinformatics (Lausanne, Switzerland).

Osmotic Shock Treatment. The periplasmic and cytosolic fractions of the whole-cell biocatalysts were separated using an osmotic shock protocol provided by Invitrogen. Briefly, cell pellets from just before induction (t=0 hours) and after expression (t=4 hours) were resuspended in Buffer OS1 (20 mM Tris-HCl, 2.5 mM EDTA, 20% sucrose, pH 8.0) to an OD_{600} of 5.0. The suspensions were incubated on ice for 10 minutes and then centrifuged for 1 minute at 13,000 rpm. The supernatant was decanted and the pellets were resuspended in Buffer OS2 (20 mM Tris-HCl, 2.5 mM EDTA, pH 8.0) to an OD_{600} of 5.0. After 10 minutes on ice, the suspensions were centrifuged for 10 minutes at 13,000 rpm. The supernatant contained the periplasmic fraction and was transferred to a fresh tube. The remaining pellet represented the cytosolic fraction.

Quantitative Western Blot Analysis. Protein samples were separated electrophoretically by size on a 4-12% Bis-Tris polyacrylamide gel. The proteins were transferred to a nitrocellulose membrane using a semi-dry blotting unit (Thermo Fisher Scientific, Waltham, MA). The transfer was performed using Towbin Buffer (25 mM Tris-HCl, 192 mM glycine, and 20% methanol). The blotted membrane was then transferred to a 50 mL centrifuge tube with the

blotted surface facing inwards. Blocking was performed using 1x phosphate buffered saline (PBS) containing 0.05% Tween-20 and 5% nonfat dry milk for 2 hours at room temperature (RT). The blocking solution was decanted and replaced with a primary antibody solution (PBS, 0.05% Tween-20, 2.5% nonfat dry milk, and 800 ng/mL anti-c-myc-FITC conjugated monoclonal antibody). The membrane was incubated in this solution for 16 hours at 4^{o}C and then rinsed 3 times for 10 minutes each at RT in PBS containing 0.05% Tween-20. Visualization was performed on a MAESTRO2 *In Vivo* Imaging System (CRI, Woburn, MA) using a 520 nm filter and a 200 msec exposure time. To quantify the visible bands, the intensity of each band was determined using the ImageJ software package (National Institute of Health; NIH, Bethesda, MD).

Carbonic Anhydrase Activity. The carbon dioxide hydration rates were determined by stopped-flow spectroscopy at 25^{o}C using a modified version of the changing pH indicator method [101], similar to an assay described previously [45]. A BioLogic stopped-flow apparatus (BioLogic, Claix, Isère, France) was used with a Jasco J-815 CD Spectrometer (JASCO, Easton, MD). Solutions of saturated CO_2 were prepared by bubbling compressed CO_2 into deionized water containing 55.6 μM *m*-cresol purple at 25^{o}C until it reached a pH of 3.91. The concentration of carbon dioxide was varied from 3 to 28 mM by mixing with N_2-saturated water with a similar concentration of *m*-cresol purple. Catalyst solutions were prepared in 100 mM Tris at pH 9.0. The absorbance at 578 nm was followed for the final solution consisting of 10 mM Tris with 50 μM *m*-cresol purple. Kinetic parameters (corrected for the uncatalyzed reaction) were determined by fitting the steady-state portion of each measurement to the differential form of the Michaelis-Menten equation using Berkeley Madonna software [119].

Biocatalyst Stability. Purified enzyme solutions and whole-cell biocatalyst suspensions in 100 mM Tris at pH 9.0 were incubated at temperatures varying from 25 to 95^{o}C for 15 minutes. After heating, the solutions were cooled on ice for 5 minutes. The activity of each solution was then measured using the stopped-flow method described above. The whole-cell biocatalysts were also tested for activity retention over a period of 24 hours. CO_2 was bubbled into cell suspensions in deionized water for 24 hours. Every 2 hours, the cells were pelleted and resuspended in fresh water to remove the accumulated bicarbonate and carbonate ions. Every 6 hours, a sample was removed and the cells were pelleted via centrifugation at 13,000 rpm for 1 minute. The supernatant was decanted and the pellets were resuspended in 100 mM Tris at pH 9.0. The activity and OD_{600} at each time point were measured to determine the CO_2 hydration rates of the whole-cells after extended use.

Precipitation. A catalyst solution containing either whole-cell biocatalysts or an equivalent amount of purified enzyme was added to a 15 mL centrifuge tube. Using a glass gas dispersion tube (Ace Glass, Vineland, NJ), compressed CO_2 gas was bubbled into each solution for 30 seconds at approximately 1 psi. This amount of time was determined to be optimal by measuring the pH curves of the various catalysts (Figure S3-2). After bubbling, calcium chloride ($CaCl_2$) and calcium carbonate ($CaCO_3$) were added to the solution to initiate the formation and precipitation of $CaCO_3$. $CaCl_2$ served as a Ca^{+2} ion source and the $CaCO_3$ served as seed particles for nucleation. The solutions were then allowed to sit at RT for 1 hour. Precipitate was collected and dried using spin columns (Epoch Life Science, Sugarland, TX) on a vacuum manifold (Qiagen, Valencia, CA). Each column was centrifuged at 5,000xg for 2 minutes to remove any residual water and weighed to determine the total mass. The masses of the empty

column, cells added, and $CaCO_3$ added were subtracted to determine the amount of $CaCO_3$ formed.

Statistical Analysis. Analysis of variance was performed using the General Linear Model on the precipitation data using the Minitab program (Minitab Inc., State College, PA). Post hoc analysis was done using the Tukey Method with a 95% confidence level.

3.1.4. Results

Plasmid Constructs. Both CA isoforms were successfully cloned into the pET-24a vector resulting in constructs pET-Cab and pET-Cam. After transformation, two colonies from each were selected for verification through DNA sequencing (GENEWIZ, South Plainfield, NJ) and creation of glycerol stocks. Also, two periplasmic leader peptides were successfully fused to Cab and Cam in the pBAD/gIIIA and pET-24a vectors. The resultant constructs (pBAD-gCab, pBAD-gCam, pET-pCab, and pET-pCam) were transformed and two colonies of each were selected for verification and creation of glycerol stocks. Whole-cell biocatalysts made using these constructs will be called BLR-gCab, BLR-gCam, BLR-pCab, and BLR-pCam.

Quantitative Western Blot Analysis. Western blot analysis was performed on samples obtained following osmotic shock. This was done to locate the enzyme within the cell and determine the amount of enzyme expressed per cell. Locating the protein was a qualitative observation made by comparing the intensity of visible bands in different lanes of the nitrocellulose membrane. For example, Figure 3-2 shows that for BLR-gCab, after 4 hours of expression a clear band is visible Lane 2 (periplasmic fraction) while nothing is visible in Lane 3 (cytoplasmic fraction) for the same timepoint. This suggests that a large fraction of the recombinantly expressed carbonic anhydrase exists in the periplasm. Any CA located in the cytosol was below the limit of

detection. Similar results were seen for BLR-gCam, BLR-pCab, and BLR-pCam (data not shown).

The amount of enzyme expressed per cell was calculated using a standard curve. Calmodulin was expressed using a control plasmid provided with the pBAD kit. Once it was purified and lyophilized, the protein was weighed to obtain a stock solution of known concentration. Dilutions of this stock were blotted using the protocol above (data not shown) and the concentration was plotted against band intensity and used to calculate the concentrations of gCab (352±17 fg/cell), gCam (50±3 fg/cell), pCab (661±26 fg/cell), and pCam (559±47 fg/cell) expressed in the periplasm.

Whole-cell Kinetics. Kinetic parameters for Cab and Cam purified from all three vectors can be found in Table 3-1 and Table 3-2, respectively. Whole-cell kinetic parameters are also presented on a per-cell basis. Purified enzyme kinetics were corrected for the uncatalyzed reaction rate while whole-cell kinetics were corrected for the reaction rates of BLR cells not expressing recombinant CA. Based on enzyme purified from pET-24a, Cab (1.6×10^4 sec^{-1}) has a lower turnover number than Cam (6.1×10^4 sec^{-1}) but also has a lower K_M (3.0 mM for Cab, 16 mM for Cam). This translates to a slightly higher catalytic efficiency for Cab (5.3×10^3 sec^{-1} mM^{-1}) as opposed to Cam (3.8×10^3 sec^{-1} mM^{-1}).

On a per cell basis, the kinetics of whole-cell biocatalysts generated using the pelB leader sequence have higher rates, and better efficiencies (reported as V_{max}/cell/K_M). This could be due to the higher expression levels seen with pelB, or perturbations in the outer membrane reducing the overall diffusion limitation of this system. A comparison of the whole-cell kinetics and purified enzyme can be seen in Figure 3-3. This figure was obtained using the measured kinetic

parameters, a fixed number of cells, and the equivalent concentration of purified enzyme based on the expression data above. This figure shows that the loss in reaction rate is approximately one order of magnitude. This loss in activity from the purified enzyme to the whole-cells indicates that the reaction is likely limited by the diffusion of reactant and/or product across the outer cell membrane of *E. coli*.

Biocatalyst Stability. As mentioned above, protein immobilization often serves as a method by which a protein or enzyme can be stabilized. The term "stability" is a broad term and can be divided into several different forms of stability. In this study, the thermal and operational stabilities were selected for measurement.

Thermal stability data is shown in Figure 3-4. Following incubation at 95^{o}C, gCab and pCab lost 15±3% and 13±3% of their original activities, respectively, while gCam and pCam lost 30±1% and 19±1%, respectively. Conversely, BLR-gCab and BLR-pCab only lost 3±1% and 1±2% of their original activities, respectively, and BLR-gCam only lost 12±3%. In these three cases, immobilization of the whole-cells stabilized the enzymes at high temperatures. However, BLR-pCam lost 35±2% of its original activity, the only case in which periplasmic expression did not improve the thermal stability of the enzyme.

After 24 hours of continuous use, the whole-cell biocatalysts also showed a high level of operational stability. The results of these experiments can be seen in Figure S3-3. On a per-cell basis, BLR-gCab, BLR-pCab, BLR-gCam, and BLR-pCam retained 106±3%, 109±1%, 95±2%, and 105±8% of their original activities, respectively, suggesting no loss of activity during this time period.

Precipitation. To investigate the carbon capture capabilities of the biocatalysts as a potential application, precipitation experiments were performed. Figure 3-5 shows the results for purified enzymes, whole-cell biocatalysts, and osmotically shocked whole-cell biocatalysts using the gIII peptide (Panel A) and the pelB peptide (Panel B). As controls, the uncatalyzed rate, untreated BLR cells expressing no recombinant CA, and osmotically shocked BLR cells expressing no recombinant CA were used. Since the experiments for each leader peptide were performed at different times, the controls were tested each time to insure the accuracy of the results.

For both sets of data, the controls within a given experiment all generated similar masses of $CaCO_3$. For the experiment using gIII, the amount precipitated was 0.07-0.08 g while for pelB about 0.09-0.1 g precipitated. This indicates that the host cells had very little effect on the amounts precipitated. Unsurprisingly, the purified enzymes for both cases precipitated the greatest masses at 0.14 g, 0.19 g, 0.17 g, and 0.24 g for gCab, gCam, pCab, and pCam, respectively. For the whole-cell biocatalysts, these masses decreased to 0.12 g, 0.11 g, 0.13 g, and 0.14 g for BLR-gCab, BLR-gCam, BLR-pCab, and BLR-pCam, respectively. Despite these reductions, the whole-cell values are greater than the controls. Degradation of the outer membrane through osmotic shock caused $CaCO_3$ to precipitate at higher levels than the whole-cell scenarios (0.14 g for BLR-gCab, 0.13 g for BLR-gCam, 0.13 g for BLR-pCab, and 0.14 g for BLR-pCam).

ANOVA was performed on the data using the General Linear Model to determine which factors had the greatest impact on the differences in $CaCO_3$ precipitated. Based on the F distributions for the three factors considered, namely the enzyme type, cell type, and the interaction between the two, p-values for these factors were all less than 0.001. These values indicate that it is extremely unlikely the observed results are due to chance. Post hoc analysis using the Tukey

method with a 95% confidence interval showed that there is a significant difference between the results obtained with CA and those obtained without CA. Also, there is a significant difference between using free enzyme and using whole-cell biocatalysts. However, osmotically shocked cells were not significantly different from whole-cells.

3.1.5. Discussion

Protein immobilization is a technique by which a protein of interest is attached to or entrapped in a solid support. By doing so, the stability of the enzyme can be improved [6]. As an added benefit, the physical size of the catalyst increases, simplifying separation of the catalyst from the reaction solution for recycling since separation of dissolved enzyme requires expensive and time-consuming unit operations. Immobilization of carbonic anhydrase has been studied in terms of adsorption to various solid surfaces [120], attachment of CA-enriched organisms to chitosan beads [121], immobilization via covalent coupling [122], and recently cell surface display through ice nucleating proteins [30]. However, periplasmic expression of CA in *E. coli* for use as a whole-cell biocatalyst has not yet been studied.

The use of *E. coli* as whole-cell biocatalysts has been previously studied [28], as has periplasmic expression of proteins [29]. In these studies, outer membrane permeability was documented as a potential limitation, and reduction in activity up to 2 orders of magnitude has been reported for whole-cell biocatalysts as opposed to free enzyme [38]. Despite these issues, the concomitant increase in stability obtained via immobilization and the elimination of protein purification may balance the activity losses, enhancing the suitability of these catalysts.

Cab and Cam were expressed in the periplasm of *E. coli* using the gIII and pelB signaling peptides fused to their N-termini. Relative to purified enzymes, the reaction rates of the whole-

cell biocatalysts decreased by between 1 and 2 orders of magnitude based on equivalent masses of enzyme, as expected [38]. This indicated that the overall CO_2 hydration reaction is likely diffusion-limited in the whole cells. This was expected due to the introduction of the outer membrane as a transport barrier.

Often, catalyst stability is measured in terms of long-term storage or shelf life [120]. In our experiments, we measured two forms of stability to determine the resistance of our catalysts to damage from both factors. Our results showed an improvement in thermal stability of the protein and retention of whole-cell activity after extended use, both of which are important for process integration [123]. Three of the four whole-cell biocatalysts exhibited more than 88% of their original activity after exposure to temperatures up to 95^{o}C. The fourth, BLR-pCam, lost 35% of its original activity, but also showed the best kinetics. It is possible that this effect is due to outer membrane perturbations that occur when using the pelB leader peptide with Cam. These results also imply that the activity and thermal stability of the whole-cell biocatalysts are linked and there is an apparent tradeoff between the activity and thermal stability of the catalysts that must be considered for use in a process.

All four whole-cell biocatalysts retained 100% of their original activity after 24 hours of use. We believe this stabilization of the enzymes in the cells is due to crowding in the periplasm. This would cause the entropic cost of protein unfolding within the periplasm to become unfavorable. Thus, a larger fraction of the immobilized proteins would remain folded at higher temperatures and for longer periods of time.

This crowding effect increases the attractiveness of periplasmic expression as a means of immobilization over other, more common immobilization techniques, such as adsorption to a

solid surface. Physisorption has been studied previously [16, 124] and was shown to cause proteins to lose structure when immobilized. In fact, as the available surface area to a protein molecule increases, so does the degree to which the protein unfolds [11]. Even very thermostable proteins experience this denaturation on the surface [125].

Finally, we demonstrated the use of whole-cell biocatalysts in carbon mineralization [126, 127], a potential carbon capture and storage application. While purified enzymes performed the best in these carbonate precipitation experiments, the additional cost of protein purification may limit the value of this approach. Statistical analysis of this data showed a significant improvement in the use of the whole-cell biocatalysts compared to the uncatalyzed reaction. However, significant improvement was not seen when using osmotically shocked cells, which should liberate the enzyme. This is most likely due to incomplete fracturing of the outer membrane of all cells, causing the diffusion barrier to persist. A more comprehensive economic analysis will be needed to truly gauge the benefit of using the whole cells.

Future directions should focus around improvement of the overall hydration reaction of the whole cells. This could potentially be accomplished by modifying the cell membrane to enhance permeability, artificially permeabilizing the outer membrane using various chemical agents, or by using different microorganisms as carriers.

3.1.6. Conclusions

By immobilizing Cab and Cam within the periplasm of *E. coli* cells, we have created new whole-cell biocatalysts for CO_2 hydration. While this introduces a transport barrier that reduces the activity as compared to the soluble enzymes, the whole cell approach increased thermal stability and should reduce catalyst costs. The cells were used to demonstrate carbon dioxide hydration

for a capture and mineralization application, and these catalysts may be valuable for other carbon capture scenarios.

3.1.7. Acknowledgements

The authors are grateful for the guidance and assistance of Mr. Edward J Swanson. This work was funded by ARPAe grant DE-AR0000100 from the US Department of Energy.

3.1.8. Figures and Tables

Figure 3-1 - Crystal structures of Cab and Cam

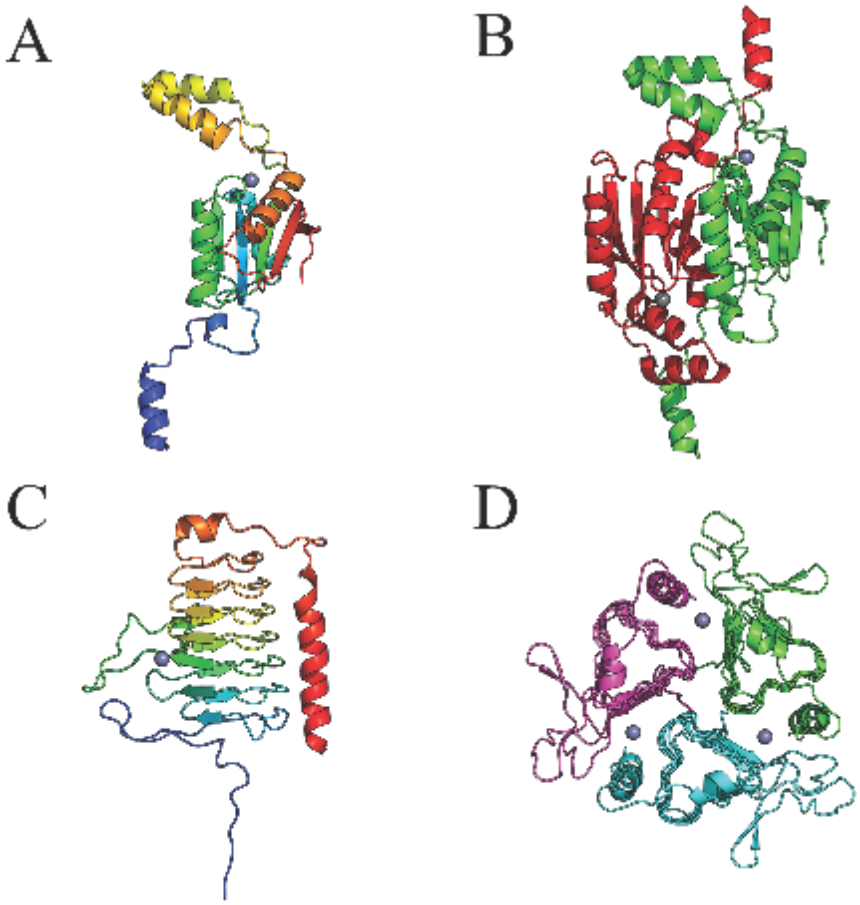

Crystal structures for the Cab (β-type; M. thermoautotriphicum; MW: 19.6 kDa; PDB:1G5C) (A) monomer and (B) dimer, and the Cam (γ-type; M. thermophila; MW: 23.0 kDa; PDB:1THJ) (C) monomer and (D) trimer. In the oligomer structures, each color represents one monomer, and the bound Zn+2 ions are represented by gray spheres

Figure 3-2 - Cell fraction western blot

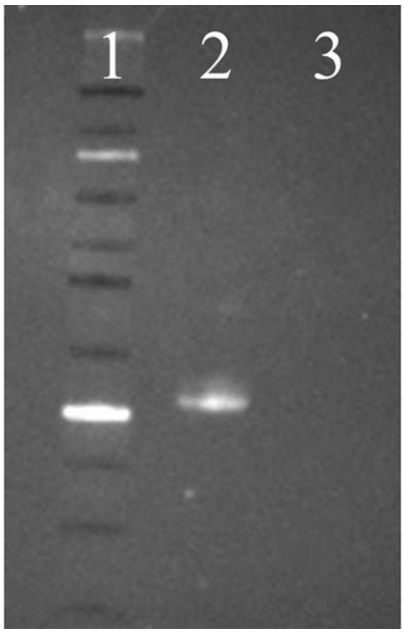

Nitrocellulose membrane showing BLR-gCab cellular fractions. Lanes 1-3 represent the molecular weight standard, periplasmic fraction after 4 hours of expression, and cytosolic fraction after 4 hours of expression. Membranes were labeled using an anti-myc-c-FITC conjugated antibody and visualized on a MAESTRO2 in vivo Imaging System. Similar results were achieved for BLR-gCam, BLR-pCab, and BLR-pCam.

Figure 3-3 - Difference in activity of free and immobilized enzyme

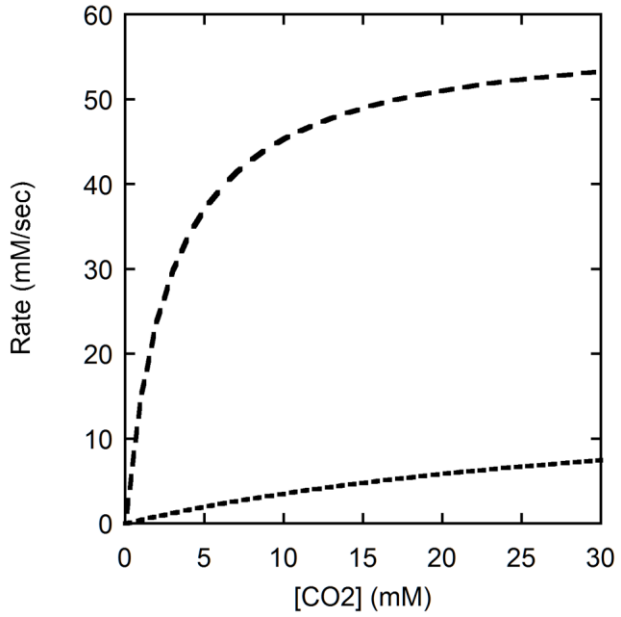

Comparison between purified enzyme (▬ ▬) and whole-cell biocatalysts (▪ ▪ ▪) using pCab. $5x10^7$ cells were used in order to obtain an equivalent concentration of 3.17 µM of purified enzyme.

Figure 3-4 - Thermal stability of biocatalysts

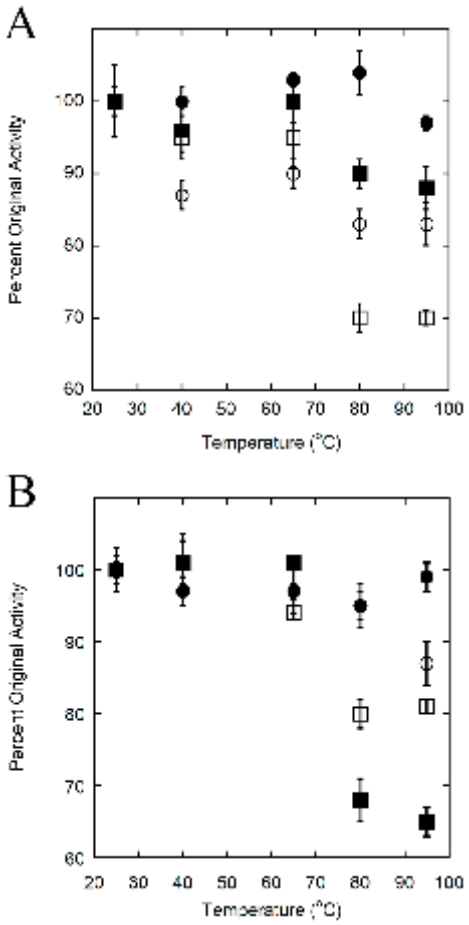

Thermal stability data for Cab and Cam expressed using the (A) gIII and (B) pelB leader peptides plotted as percent of original activity. For panel A, stabilities are reported for gCab (○), gCam (□), BLR-gCab (●), and BLR-gCam (■). Similarly for panel B, stabilities are reported for pCab (○), pCam (□), BLR-pCab (●), and BLR-pCam (■). Errors bars represent the standard deviations from the means.

Figure 3-5 - $CaCO_3$ precipitation

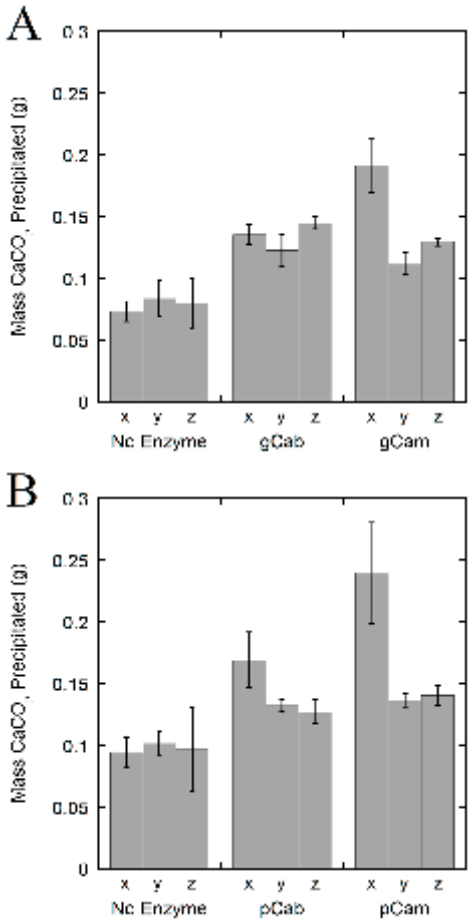

Masses of $CaCO_3$ precipitate formed in the absence of recombinantly expressed enzyme (control experiments), Cab, and Cam using the (A) gIII and (B) pelB leader peptides. For each catalyst, 3 configurations were tested: (x) free enzyme, (y) whole-cell biocatalysts, and (z) osmotically shocked whole-cell biocatalysts. Error bars represent the standard deviations from the means.

Table 3-1 - Purified enzyme and whole-cell kinetics for Cab variants

Catalyst	k_{cat} (sec^{-1})	K_M (mM)	k_{cat}/K_M (sec^{-1} mM^{-1})	V_{max}/cell (mM sec^{-1} $cell^{-1}$)	V_{max}/cell/K_M (sec^{-1} $cell^{-1}$)
Cab[a]	1.7×10^4	2.9	5.9×10^3	-	-
Cab	$1.6 \pm 0.1 \times 10^4$	3.0 ± 0.2	$5.3 \pm 0.3 \times 10^3$	-	-
gCab	$2.0 \pm 0.1 \times 10^4$	3.0 ± 0.1	$6.5 \pm 0.1 \times 10^3$	-	-
BLR-gCab	-	38 ± 5	-	$2.5 \pm 0.6 \times 10^{-7}$	$6.5 \pm 0.7 \times 10^{-9}$
pCab	$1.8 \pm 0.1 \times 10^4$	2.9 ± 0.1	$6.5 \pm 0.2 \times 10^3$	-	-
BLR-pCab	-	39 ± 4	-	$3.4 \pm 0.4 \times 10^{-7}$	$8.9 \pm 0.2 \times 10^{-9}$

[a]Previously published values [45]

"-" indicates parameter is not relevant to catalyst

All measurements were made in triplicate and error represents the standard deviation from the mean.

Table 3-2 - Purified enzyme and whole-cell kinetics for Cam variants

Catalyst	k_{cat} (sec^{-1})	K_M (mM)	k_{cat}/K_M (sec^{-1} mM^{-1})	V_{max}/cell (mM sec^{-1} $cell^{-1}$)	V_{max}/cell/K_M (sec^{-1} $cell^{-1}$)
Cam[a]	7.7×10^4	15	5.2×10^3	-	-
Cam	$6.1 \pm 3.0 \times 10^4$	16 ± 1	$3.7 \pm 1.7 \times 10^3$	-	-
gCam	$6.8 \pm 1.5 \times 10^4$	17 ± 1	$4.0 \pm 1.0 \times 10^3$	-	-
BLR-gCam	-	31 ± 3	-	$1.9 \pm 0.4 \times 10^{-7}$	$6.0 \pm 0.6 \times 10^{-9}$
pCam	$7.7 \pm 1.5 \times 10^4$	14 ± 1	$5.7 \pm 1.4 \times 10^3$	-	-
BLR-pCam	-	31 ± 3	-	$5.9 \pm 0.9 \times 10^{-7}$	$19 \pm 1.2 \times 10^{-9}$

[a]Previously published values [45]

"-" indicates parameter is not relevant to catalyst

All measurements were made in triplicate and error represents the standard deviation from the mean.

3.1.9. Supplementary Information

Figure S3-1 - Sequence information for Cab and Cam

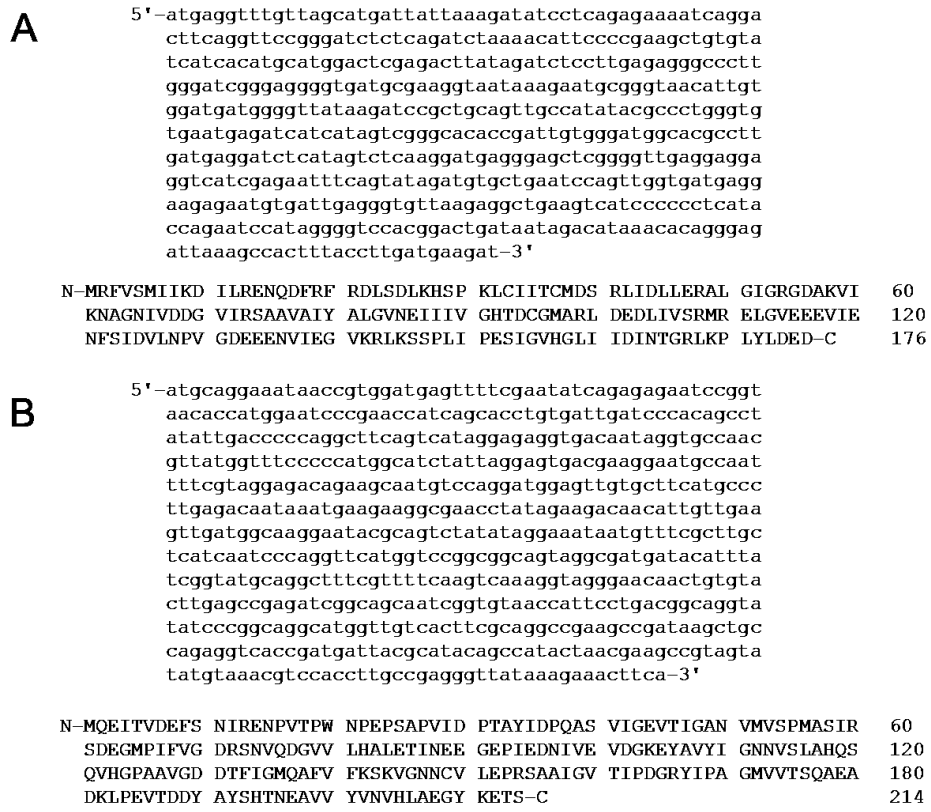

Nucleotide and amino acid sequences for WT (A) Cab and (B) Cam

Table S3-1 - Primer sequences used for Cab and Cam cloning

Primer	Description	Sequence
TP03	Cam Forward NdeI	AGT CAG CAT ATG CAG GAA ATA ACC GTG GAT
TP05	Cab Forward NdeI	AGT CAG CAT ATG AGG TTT GTT AGC ATG ATT ATT
TP09	Cab Reverse HindIII	AGT CAG AAG CTT TTT ATC TTC ATC AAG GTA AAG TGG
TP10	Cam Reverse HindIII	AGT CAG AAG CTT TTT TGA AGT TTC TTT ATA ACC CTC
TP11	Cab Forward KpnI	AGT CAG GGT ACC ATA TGA GGT TTG TTA GCA TGA TT
TP12	Cab Reverse HindIII	AGT CAG AAG CTT CCT TTA TCT TCA TCA AGG TAA AGT GG
TP14	Cam Reverse KpnI	AGT CAG GGT ACC CTT TTG AAG TTT CTT TAT AAC CCT C
TP42	Cam Forward SacI	AGT GAC TAG AGC TCA TGC AGG AAA TAA CCG
TP34	Cab Forward SfiI	AGT CAG GGC CCA GCC GGC CAT GGC GAG GTT TGT TAG CAT GAT TAT TAA A
TP35	Cab Reverse SfiI	AGT CAG GGC CCC CGA GGC CCC GCC ATC TTC ATC AAG GTA AAG TG
TP36	Cam Forward SfiI	AGT CAG GGC CCA GCC GGC CAT GGC GCA GGA AAT AAC CGT GGA T
TP37	Cam Reverse SfiI	AGT CAG GGC CCC CGA GGC CCC GCC TGA AGT TTC TTT ATA ACC CT
TP38	pelB-Cab Forward NdeI	AGT CAG CAT ATG AAA TAC CTA TTG CCT ACG
TP39	pelB-Cab Reverse HindIII	AGT CAG AAG CTT CAG GTC TTC CTC AGA GAT
TP40	pelB-Cam Forward NdeI	AGT CAG CAT ATG AAA TAC CTA TTG CCT ACG
TP41	pelB-Cam Reverse HindIII	AGT CAG AAG CTT CAG GTC TTC CTC AGA GAT

*Underlined sequences indicate restriction sites

Figure S3-2 - pH curves for free and immobilized enzymes

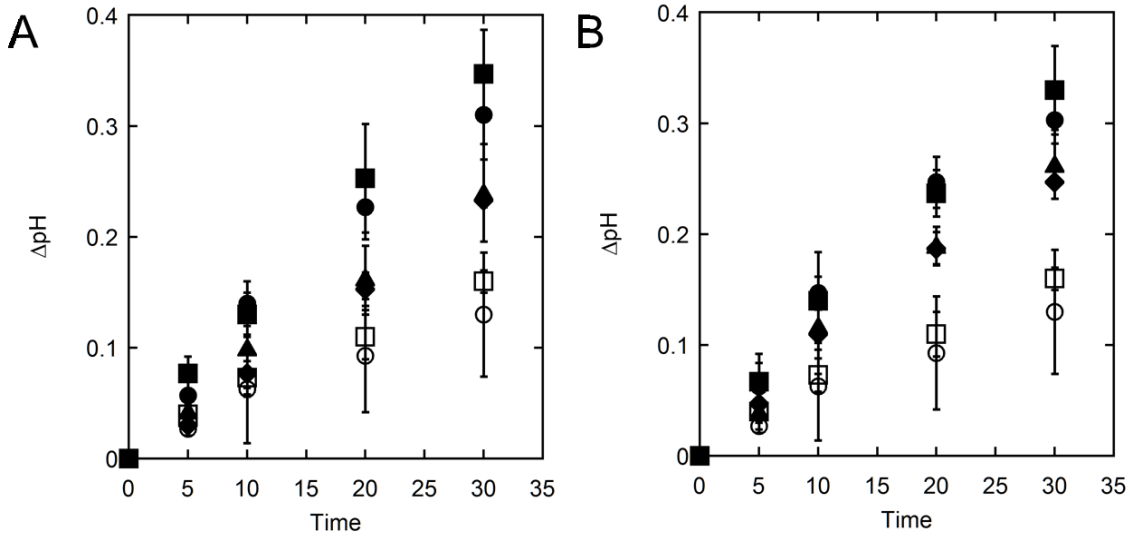

pH curves for Cab and Cam as purified enzymes and whole-cell biocatalysts using the (A) gIII and (B) pelB leader peptides. Panel A contains curves for the uncatalyzed reaction (○), BLR cells expressing no recombinant CA (□), gCab (●), gCam (■), BLR-gCab (◆), and BLR-gCam (▲). Similarly, panel B contains curves for the uncatalyzed reaction (○), BLR cells expressing no recombinant CA (□), pCab (●), pCam (■), BLR-pCab (◆), and BLR-pCam (▲). Error bars represent the standard deviations from the means.

Figure S3-3 - Activity retention after 24 hours

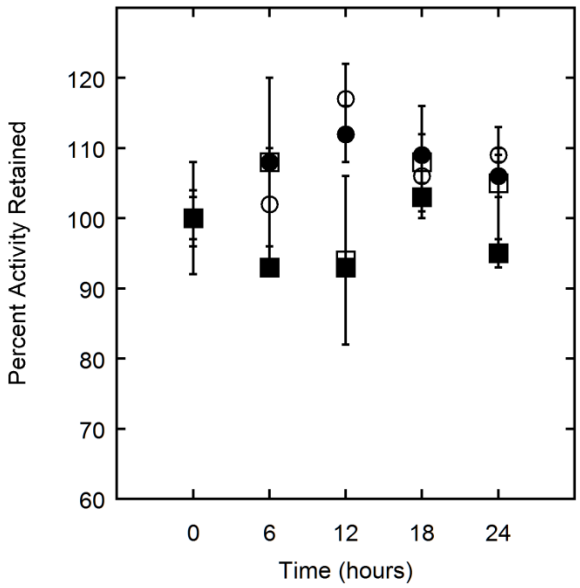

Retention of activity by BLR-gCab (●), BLR-gCam (■), BLR-pCab(○), and BLR-pCam (□) after 24 hours of catalysis plotted as a percentage of their initial whole-cell biocatalyst activities. Error bars represent the standard deviations from the means.

3.2. Operational Stability Measurements

Note: A version of this chapter entitled "An Automated Method for Measuring the Operational Stability of Biocatalysts with Carbonic Anhydrase Activity." is published in *Biochemical Engineering Journal* (2014), volume 82, pages 48-52, with co-authors Edward J Swanson, Alissa Ah-Hyung Park, and Scott Banta.

TNP designed and performed all experiments, analyzed the data, and wrote the manuscript.

3.2.1. Abstract

The operational stability of an enzyme can be quantified by its half-life, or the length of time after which 50% of its original activity has degraded. Ideally, continuous methods for measuring half-lives are preferred but they can be expensive and relatively low throughput. Batch methods, while simple, cannot be used for all enzymes. For example, batch reactions can be difficult when there is a gas phase reactant or when there is significant product or substrate inhibition. Here we describe a repeated-batch method for measuring the half-life of carbonic anhydrase (CA)-based biocatalysts by automated periodic switching between a forward and reverse reaction. This method is inexpensive and can be multiplexed for high-throughput analysis of enzyme variants. Several purified CA enzymes as well as whole-cell biocatalysts with engineered CA activity were evaluated with this method. The results indicate a significant increase in operational stability is achieved upon immobilization of CA in the cellular periplasm of *E. coli*.

3.2.2. Introduction

The stability of an enzyme or biocatalyst is a critical parameter. It can dictate the proper storage, optimal reaction conditions, and functional lifetime of a biocatalyst. However, the term "stability" covers a broad range of properties including thermal stability, pH stability, and operational (or kinetic) stability [123, 128-131]. The stability of an enzyme is dependent on several phenomena including the structure of the protein, hydrophobic interactions, ionic interactions, hydrogen bonding, and other weak interactions [132-135]. Previously, researchers have explored methods to stabilize enzymes via directed evolution [136], rational mutagenesis of

surface residues [137, 138], the introduction of non-native disulfide bonds [139], and various immobilization techniques [6]. In most of these studies, the thermal stability of the enzymes is being measured and is assumed to be related to the overall stability of the catalyst, including the operational stability. However, this may not always be a valid presumption since the thermal stability does not account for the reaction being catalyzed [130]. Instead, the operational stability should be measured independently.

Ideally, the operational stability would be measured in a continuous reactor system such as a plug-flow reactor (PFR) or continuous stirred tank reactor (CSTR) under the process conditions desired. Such experiments would yield relevant stability data for biocatalysts to be used in processes [130]. But, these experiments are expensive and low throughput. Conversely, simpler batch-wise measurements can be performed, and these experiments generally involve mixing a large amount of substrate with the enzyme and allowing the reaction to progress for many half-lives of the enzyme [140]. Batch measurements are typically less expensive, but cannot be used for all types of biocatalysts. For example, the batch method is limited when there is significant substrate or product inhibition, or when substrates cannot be added in large quantities at the onset of the reaction. Thus, a repeated-batch method provides a compromise between these approaches. In such a system, the activity of a biocatalyst is measured in a series of batch reactions within a fixed range of substrate concentration [130]. By comparing these activities, the point at which 50% of the activity has degraded can be identified as the half-life of the biocatalyst. Here we develop an automated repeated-batch method for measuring the half-lives of carbonic anhydrase (CA; EC 4.2.1.1) biocatalysts.

CAs are well-studied, Zn^{+2}-binding metalloenzymes that catalyze the reversible hydration of carbon dioxide (CO_2) to bicarbonate (HCO_3^-) and carbonate (CO_3^{-2}) ions [39] according to the mechanism shown below [41]:

$$EZnH_2O \rightleftharpoons EZnOH^- + H^+ \quad (1)$$

$$EZnOH^- + CO_2 \rightleftharpoons EZnHCO_3^- \quad (2)$$

$$EZnHCO_3^- + H_2O \rightleftharpoons EZnH_2O + HCO_3^- \quad (3)$$

$$HCO_3^- \rightleftharpoons CO_3^{-2} + H^+ \quad (4)$$

In this scheme, the reversible deprotonation of bicarbonate (Eqn 4) occurs spontaneously as a function of pH, and is not catalyzed by the enzyme. Nearly ubiquitous in nature, CAs are among the fastest known enzymes with turnover numbers (k_{cat}) ranging from 10^4-10^6 sec^{-1} [42, 96]. While most of the prior research on CA has focused on isolation and characterization of these enzymes, recent work has explored immobilization of CAs using yeast [141] and *E. coli* cells [30, 142] for use as whole-cell biocatalysts. These catalysts have the benefits of enzyme stabilization and enhanced recyclability, while maintaining CO_2 hydration activity. In addition to these studies, CA enzymes have been investigated as mediators for carbon capture modalities, specifically carbon mineralization [127]. This technique involves the conversion of CO_2 into carbonate ions and subsequent precipitation with divalent cations such as Ca^{+2}. For example, *in situ* carbon capture from the flue gas of coal-fired power plants has been proposed and studied as a potential industrial application of CA enzymes [143]. Other applications for CA enzymes include biosensors [50], CO2 fixation for artificial photosynthesis [48], and for biofuel production [49]. Despite the breadth of research performed on CAs, operational stabilities have not yet been reported. Some variants of CA possess alternative activities such as esterase activity [144] or peroxidase activity upon substitution of the bound Zn^{+2} ion with an Mn^{+2} ion [145]. For these special cases, measurement of the stability by a batch method would be possible.

However, most forms of CA do not possess these alternative activities, and these activities are not related to the hydration activity of CA. Thus, determining the operational stability of CA using esterase or peroxidase activity may not be possible, or may lead to irrelevant results.
In this report, a method for measuring the operational stability of CA-based biocatalysts is described. The CA isoforms measured were bovine carbonic anhydrase from erythrocytes (BCA), carbonic anhydrase beta (Cab from *Methanobacterium thermoautotriphicum*; PDB: 1G5C) [45], and carbonic anhydrase methanosarcina (Cam from *Methanosarcina thermophila*; PDB: 1THJ) [51]. In addition to the purified forms of these enzymes, Cab and Cam were also tested after immobilization via periplasmic expression using two different periplasmic leader peptides (gIII and pelB), as previously described, to generate whole-cell biocatalysts [142]. These biocatalysts were selected for the various benefits they present. BCA was chosen because it is a commercially available CA that has been studied by several groups in the past. Cab and Cam were selected because they differ in their intrinsic thermal stabilities. Further, since these two isoforms were used in whole-cell biocatalysts, they provide us with the opportunity to examine the versatility of our technology, as well as examine the effects of periplasmic immobilization on operational stability.

3.2.3. Materials and Methods

Materials. All chemicals, including BCA, were obtained from Sigma-Aldrich (St. Louis, MO) unless otherwise indicated. Nylon tubing and push-to-connect fittings and joints for all gas lines were purchased from McMaster-Carr (Robbinsville, NJ).

Cloning, Expression, and Purification. Cloning, expression, and purification of all constructs were described previously [142]. Cab and Cam used in these experiments were purified from the pET-24a vector with no periplasmic leader sequence. The whole-cell biocatalysts used were

BLR-gCab, BLR-pCab, BLR-gCam, and BLR-pCam where "g" indicates the gIII leader peptide is being used, while "p" indicates the pelB leader peptide is used [142].

Apparatus. A schematic of the apparatus can be seen in Figure 3-6A. The apparatus consists of 4 main components: an ethylene glycol-filled water bath with a 250 mL plastic bottle (reaction vessel) and two 1 L plastic bottles (saturation vessels), an OMEGA USB-4718 Data Acqusition Module (DAQ; OMEGA Engineering, Inc., Stamford, CT), gas flow from compressed prepurified N_2 and bone dry CO_2 cylinders (TechAir, White Plains, NY), and a LabView Virtual Instrument (VI; National Instruments, Austin, TX) to control gas switching and record data. The pressure at each regulator outlet is continuously monitored using a pressure transducer (Omegadyne Inc., Sunbury, OH) connected to the DAQ. For each gas, flow is routed through a 24V, 7W, 175 psi solenoid valve (Peter Paul Electronics Co., Inc., New Britain, CT) before being passed through a saturation vessel containing 950 mL deionized water (DI H_2O) using a stainless steel gas sparger (Valco Instruments Co., Inc., Houston, TX). This hydrates the gas to reduce liquid loss in the reaction vessel. The solenoid valves are connected to the DAQ and switching between the gases is done using a 12V, 15A power relay (Tyco Electronics Corp., Wilmington, DE), also connected to the DAQ. Other components wired to the DAQ are a PHB-213 pH meter (OMEGA Engineering, Inc., Stamford, CT) and an immersion thermocouple (McMaster-Carr, Robbinsville, NJ). The hydration containers are linked via a T-joint and attached to the output is a fritted glass sparger (ACE Glass, Inc., Vineland, NJ).

Stability measurements. The filled saturation vessels and reaction vessel containing 100 mL of 100 mM Tris-HCl pH 9.0 were placed in the glycol bath set to the desired temperature (30^{o}C for this study). The pH probe, thermocouple, and glass sparger were placed in the reaction vessel and the top was wrapped in Parafilm. This reduced the loss of volume by evaporation in the

reaction vessel. The VI was activated to initiate control over the apparatus. The relay was plugged in to start gas flow and the outlet pressure of each tank was adjusted to 6 psi. After the desired pH range was entered, data acquisition was started and the baseline was collected for 30-60 minutes, or until it stabilized. A pH range of 6.9-7.75 was chosen for this study for its consistency and reproducibility under the conditions used. This is within the effective range of Tris buffer which has an approximate pKa of 7.92 at 30°C. However, the pH bounds can be set to any values, as long as the pH probe and buffer being used are effective within that range. Then, the desired catalyst was added to the reaction vessel (15-38 μg/mL for purified enzymes or $4.6x10^8$-$1.2x10^9$ cells/mL for whole-cell biocatalysts). The reaction vessel was wrapped in Parafilm and the reaction was allowed to proceed for 24-48 hours. For each run, 2 data files were generated: a trace of pH against process time, and the temperature, pressure, and the upswing and downswing periods against process time. The "downswing period" was defined as the amount of time required to traverse the defined pH range during the forward reaction (CO_2 sparging). The "upswing period" is defined the same way, but for the reverse reaction (N_2 sparging). Sample data obtained using this system can be seen in Figure 3-6.

Data Analysis. To represent the operational stabilities of the biocatalysts tested, the half-life was selected as the relevant metric. For each biocatalyst, the plot of downswing period vs. process time was fit to the monoexponential decay equation:

$$\omega = \omega_0 + A(1 - e^{-kt}) \qquad (5)$$

where ω is the period at time t, ω_0 is the initial period, A is the amplitude constant, k is the decay constant, and t is the time. Using the least-squares method, ω_0, A, and k were varied to obtain the best fit. An example of this analysis can be seen in Figure 3-6C.

To obtain the half-lives from these fits, Equation 5 was rearranged to solve for *t* as a function of *k*:

$$t = -\frac{\ln(1-\chi)}{k} \qquad (6)$$

where χ is the fraction of activity lost (defined as $\omega - \omega_0/_A$) and has possible values of $0<\chi<1$. By substituting a value of 0.5 for χ, the resulting calculation yielded a value in hours representing the half-life of the biocatalyst.

Statistical Analysis. Half-life results were subjected to an Analysis of Variance (ANOVA) statistical test using the General Linear Model using the Minitab program (Minitab, Inc., State College, PA). Post-hoc analysis was performed using a 95% confidence level with the Tukey method.

3.2.4. Results

Apparatus Properties. Preparing the system for a new measurement takes approximately 60-80 minutes, including baseline acquisition. The system can run with high stability for up to 36 hours. After this time, drift in downswing period was sometimes observed, however experiments up to 48 hours were possible with this experimental design. Catalyst addition was performed in small increments (20-100 μL) to reduce foaming.

Purified Enzyme Stabilities. Three purified enzymes were explored: BCA (k_{cat}/K_M=1.7x10^4 mM^{-1} sec^{-1} [45]), Cab (k_{cat}/K_M=5.9x10^3 mM^{-1} sec^{-1} [51]), and Cam (k_{cat}/K_M=5.2x10^3 mM^{-1} sec^{-1} [146]). The half-lives of these enzymes can be seen in Table 3-3. All measurements were performed in triplicate. The errors in these values are the standard deviations from the means. Cab was found to have the longest half-life with a mean of 26 hours. ANOVA on the purified enzyme data indicated that the three enzymes are statistically significantly different. Post-hoc analysis revealed that the half-life of Cab is statistically significantly different from both Cam

(11 hours) and BCA (4.2 hours). Cam and BCA were not found to differ to a significant degree, likely due to the larger standard deviation in the Cam data.

Whole-Cell Biocatalyst Stabilities. Four whole-cell biocatalysts containing periplasmically-expressed CAs were evaluated: BLR-gCab ($V_{max}/K_M/cell$ =6.5x10^{-9} sec^{-1} cell^{-1}), BLR-pCab ($V_{max}/K_M/cell$ =8.9x10^{-9} sec^{-1} cell^{-1}), BLR-gCam ($V_{max}/K_M/cell$ =6.0x10^{-9} sec^{-1} cell^{-1}), and BLR-pCam ($V_{max}/K_M/cell$ =19x10^{-9} sec^{-1} cell^{-1}) [142]. The half-lives of these biocatalysts were found to be so long that they were not able to be estimated using the described apparatus. Throughout the range of stable operation of the apparatus, the whole-cell biocatalysts did not decay past the linear regime of the monoexponential decay function. The analysis method requires that the data reaches a plateau or at least contains an inflection point so that the data can be fit to equation 5. Several numerical methods were explored, however more data would be needed to accurately determine the fitting parameters. Thus, half-life data is not shown for these biocatalysts and they are all presumed to be much greater than 48hours. In order to quantify the half-lives of biocatalysts whose operational stabilities outlive the stability of the system, the apparatus would need to be modified to enable operation for longer periods of time.

3.2.5. Discussion

Operational vs. Thermal Stability. Cab was determined to have the highest operational stability of the purified enzymes which is not surprising as Cab is one of the most thermostable forms of CA reported [42]. These results appear to suggest a correlation between the thermal and operational stabilities of these biocatalysts. However, this relationship may not always hold, as thermal and operational stabilities can be influenced by different factors. [130, 131]. For example, we previously explored thermal stability of the Cam variant by incubation at 95^{o}C before measuring activity. This treatment caused similar effects in the free enzyme and whole

cell biocatalysts as purified Cam retained approximately 70-81% of its original activity and BLR-pCam retained 65% of its original activity [142]. This is in contrast to the present study where the half-life of BLR-pCam was greater than 24 hours while that of purified Cam was 11 hours.

Stabilization upon Immobilization. The results showed that the enzymes were both stabilized upon immobilization, as expected [6]. Although the full extent of this stabilization was not quantified, each enzyme experienced enhanced operational stability in the whole-cell configuration as opposed to their purified forms. One hypothesis for this stabilization effect is that the protein loading within the relatively small volume of the periplasm would cause molecular crowding [142]. This would increase the entropic cost of protein unfolding, thus increasing protein stabilization.

Metrics for Reporting Operational Stability. The operational stabilities of the biocatalysts in this study are reported in terms of half-lives. While this is among the more commonly reported metrics for the stability of a biocatalyst [131], this value has been criticized for its limited applicability [147] and its relevance to a process [130]. As a preferable alternative, presentation of activity vs. process time has been proposed [147]. Using our system, the downswing period data vs. time provides such a plot, as seen in Figure 3-6and Figure 3-7, and could also be used to describe the stability.

Another alternative metric could be obtained by first linearizing Equation 5 and plotting the period vs. time data according to this linearized form. By applying a linear fit, the slope of the line could be used to indicate the operational stability. A lower slope would indicate slower degradation of activity and thus a more stable biocatalyst. This would be especially useful for

the whole-cell biocatalysts for which the data does not contain an inflection point for fitting the monoexponential decay function.

Potential System Upgrades and Modifications. In order to measure half-lives of extremely stable catalysts, modifications to the apparatus would have to be made to extend the experimental times. This would include better control of environmental conditions to stabilize the system volume and other modifications to the system hardware.

In this report, only CA-based catalysts were tested. However, this apparatus could be used for other enzymes with a few modifications. Enzymes such as monodehydroascorbate reductase (EC 1.6.5.4), nitric oxide dioxygenase (EC 1.14.12.17), and sulfur oxygenase/reductase (EC 1.13.11.55) [148] could be characterized. Possible modifications include altering the gases to dictate reaction direction or using a different ion-selective electrode as opposed to a pH meter. Further, this apparatus could be modified to operate at a higher throughput. By using multiple reaction vessels, this method could be used as a screening method for exploring variants or mutants for increased operational stability, activity, etc.

Finally, we believe this technology can pave the way towards answering some fundamental questions about operational stability of biocatalysts, particularly those with CA activity. For example, using this method, the half-life could be determined as a function of temperature, pH, and reaction rate (by way of varying the substrate concentration). In doing so, the biocatalysts could be evaluated for their inherent properties, as well as their potential performance under operating conditions for implementation into a process. Such studies are rarely found in current literature, but with this method understanding the effects of environmental conditions on operational stability could be elucidated.

3.2.6. Conclusions

Described in this report is an automated method for measuring the operational stability of CA-based biocatalysts. Homogeneous (purified enzymes) and heterogeneous biocatalysts (whole-cells) were characterized using this method. By utilizing constant data monitoring and automatic switching between the forward and reverse reactions, long reaction times requiring little monitoring were possible. This repeated-batch method enables the simple and low-cost lab-scale testing of many enzymes, including CA. Our results found that Cab had the longest half-life compared to the other purified enzymes, and that immobilization of Cab and Cam in the periplasmic space extended the half-life beyond the limits of our experimental device. This repeated-batch method will be a useful tool for exploring different biocatalysts with CA or related activities.

3.2.7. Acknowledgements

We would like to thank Mr. Devante Bledsoe for his laboratory-related assistance. We also greatly acknowledge the financial support from ARPA-E (Department of Energy; Grant DE-AR0000100).

3.2.8. Figures and Tables

Figure 3-6 - Stability data collection and analysis

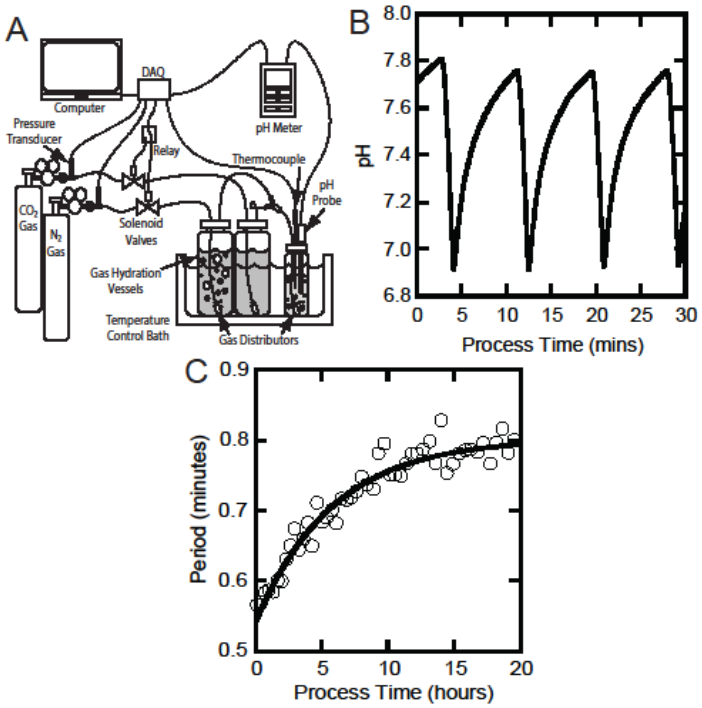

(A) Schematic representation of the apparatus showing all essential components. In this drawing, both electrical wiring (– –) and tubing for gas flow (——) are shown. (B) Trace of pH against process time with several cycles shown. (C) Downswing period (O ; forward reaction; CO_2 bubbling) against process time with monoexponential fit (——) used to calculate half-life for BCA. The period indicates the amount of time required to pass between the pH setpoints. Thus, the increase in period over time shown indicates a degradation of activity as time passes. In panel (C), only 50 of the data points are shown.

Figure 3-7 - Purified and immobilized enzyme stability traces

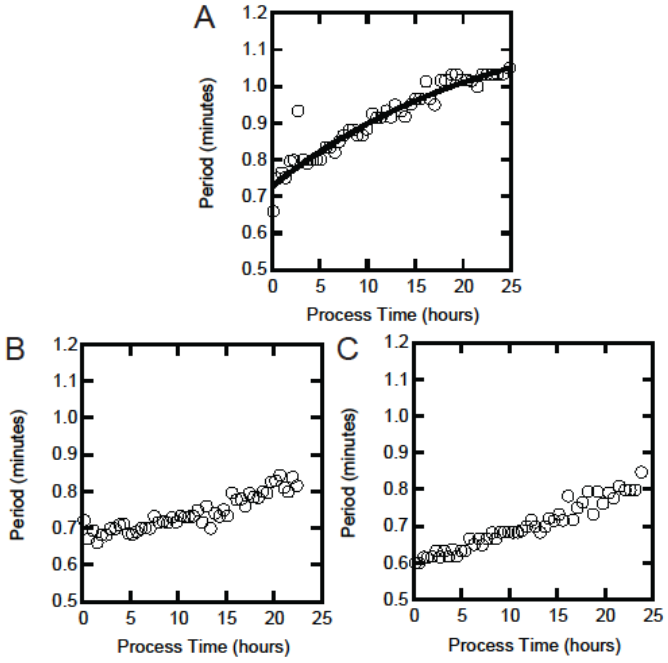

Downswing period (O ; forward reaction; CO_2 bubbling) against process time for (A) purified Cam, (B) BLR-gCam, and (C) BLR-pCam. The data for purified Cam (A) could be fit by a monoexponential equation and the fit to the data is shown (——). When Cam was stabilized upon immobilization, the data was linear (B & C) and could not be fit by the monoexponential, indicating half-lives beyond the capabilities of the experimental apparatus.

For all three plots, only 50 data points for the time range are shown.

Table 3-3 - Half-lives of purified enzymes

Biocatalyst	Half-Life (hours)[a]
BCA	4.2 ± 1.3
Cab	26 ± 5[b]
Cam	11 ± 5

[a]Measurements were performed in triplicate, errors represent standard deviations.

[b]Statistically significantly different from the other purified enzymes tested

4. Engineering Outer Membrane Permeability

Note: A version of this chapter will be included in a future manuscript, currently in review.

TNP designed and performed all experiments, analyzed the data, performed the quantitative analysis, and wrote the manuscript.

4.1. Abstract

The limited permeability of the *E. coli* outer membrane can significantly hinder whole-cell biocatalyst performance. In this study, the SARS coronavirus small envelope protein (SCVE) was expressed in *E. coli* cells previously engineered for periplasmic expression of carbonic anhydrase (CA) activity. This maneuver increased small molecule uptake by the cells, resulting in increased apparent CA activity of the biocatalysts. The enhancements in activity were quantified using methods developed for traditional heterogeneous catalysis. The expression of the SCVE protein was found to significantly reduce the Thiele moduli (ϕ), as well as increase the effectiveness factors (η), effective diffusivities (D_e), and permeabilities (P) of the biocatalysts. These catalytic improvements translated into superior performance of the biocatalysts for the precipitation of calcium carbonate from solution which is an attractive strategy for long-term sequestration of captured carbon dioxide. Overall, these results demonstrate that synthetic biology approaches can be used to enhance heterogeneous catalysts incorporated into microbial whole-cell scaffolds.

4.2. Introduction

Gram-negative bacteria, such as *Escherichia coli*, have been previously shown to be less permeable than gram-positive bacteria, largely due to their outer membrane [149]. The native permeability through the outer membrane arises from porin proteins. The hydrophobic transmembrane α-helical domains of these proteins form tightly associated trimeric bundles that

form non-specific molecular transport channels [150-155]. Monomeric molecular weights of native porins can range from 28 to 48 kDa [154]. Common porins include OmpF, OmpC, and PhoE. Among all of the proteins within a cell, these are often the most prevalent on a mass basis. They typically form 10^5 channels per cell or more [152]. Transport through these channels is highly dependent on the properties of the solute, including physical size, charge, and hydrophobicity. In general, a typical porin generates a pore roughly 0.9-1.1 nm in diameter, and excludes molecules above 0.6 kDa [150, 155]. In addition to porins, specific channels also exist in the outer membrane for the transport of maltose and maltodextrans (LamB), nucleotides (Tsx), and ferrichrome (FhuA), among others [151].

Despite the presence of native porins, several chemical [156-159], biological [156, 157, 160-163], and genetic[156, 164-167] treatments have been explored for outer membrane permeabilization. In most cases, these experiments were performed to better understand the structure and function of the outer membrane. More recent studies have examined the impact of permeabilization on biocatalysis [168], as well as other whole-cell bioprocesses such as nutrient uptake [38]. One promising approach is the use of viroporins, which are a diverse class of viral proteins that further permeabilize the membranes of host cells [169-171]. Some viroporins encoded by bacteriophages are also referred to as holins [172]. Viroporins are similar to porins in that they oligomerize within the membrane to form pores, and this oligomerization often occurs between the hydrophobic, transmembrane, α-helical domains of the proteins [170]. Archetypal viroporins include the Picornavirus P2B, HCV p7, IAV M2, and HIV-1 Vpu proteins [171]. Viroporins also possess similar exclusion sizes to porins, only allowing diffusion of small molecules [173]. The recombinant expression of viroporins in E. coli has been previously studied by several research groups, as indicated above. In these previous studies, the primary focus was the

structure of the protein and the pore formed by oligomerization of the transmembrane domains. Characterization of the effects of introducing these new pores into the outer membrane was largely limited to the diffusion of various small molecules across the membrane.

As the field of synthetic biology matures, it is becoming clear that we are just beginning to understand of the extent to which biological systems and parts can be designed, modified and utilized to address critical needs. Recent examples include engineering of advanced batteries from biological templates, enzymatic biomaterials, biological logic gates, and many other advances are clearly on the horizon. Here we explore the use of synthetic biology to create heterogeneous catalysts for the capture of carbon dioxide, which will be critical as we move towards the capture and utilization of carbon dioxide, or even the permanent sequestration of carbon dioxide from the atmosphere. To accomplish this goal we have previously expressed CA enzymes in the periplasm of E. coli, and here we report on the improvements in this system that can be obtained by reducing transport limitations via further genetic manipulation of the cells.

In this study, the SARS (severe acute respiratory syndrome) coronavirus envelope (SCVE) protein was evaluated for its ability to permeabilize the outer membrane of *E. coli*. The 76 amino acid SCVE protein is predominantly hydrophobic and each monomer contains one transmembrane domain, which when expressed on its own, can oligomerize into dimeric, trimeric, or pentameric bundles [174]. However, when the full protein is expressed, only homopentamers are observed *in vivo* [175]. These bundles were determined to be formed due to two cysteines at positions 40 and 44. Mutations at these sites rendered the protein inactive and unable to form transmembrane pores [173]. Inhibition of pore formation was also seen in the presence of hexamethylene amiloride (HMA) [176]. The pores formed by the SCVE protein are estimated to have a radius of about 0.6 nm [174], and preferentially facilitate transport of

monovalent cations as opposed to monovalent anions [177]. Recently, SCVE was expressed in *E. coli* and was shown to improve the diffusion of two different small molecules across the outer membrane [173]. Therefore recombinant expression of SCVE is a promising approach for modulating transport across the outer membrane of *E. coli*.

Whole-cell biocatalysts containing carbonic anhydrase (CA; EC 4.2.1.1) as their enzymatic component have recently emerged as a cost-effective method for catalyzing the hydration reaction of carbon dioxide (CO_2) [30, 141, 142, 178]. CAs are Zn^{+2}-binding metalloenzymes that are able to reversibly catalyze the hydration of aqueous CO_2 via the reaction mechanism below, where "EZn" represents the enzyme molecule and the bound Zn^{+2} ion [39, 41]:

$$EZnH_2O \rightleftharpoons EZnOH^- + H^+ \quad (1)$$

$$EZnOH^- + CO_2 \rightleftharpoons EZnHCO_3^- \quad (2)$$

$$EZnHCO_3^- + H_2O \rightleftharpoons EZnH_2O + HCO_3^- \quad (3)$$

$$HCO_3^- \rightleftharpoons CO_3^{-2} + H^+ \quad (4)$$

Two isoforms of CA were selected for this study: carbonic anhydrase beta (Cab; *Methanobacterium thermoautotriphicum*; PDB 1G5C) [45] and carbonic anhydrase methanosarcina (Cam; *Methanosarcina thermophila*; PDB 1THJ) [51]. We have previously reported the periplasmic expression of these isoforms in *E. coli*, resulting in functional whole cell biocatalysts, however the activity was decreased as compared to the activity of the purified enzymes due to membrane transport limitations [142].

Therefore, in this study the whole-cell biocatalysts were modified by SCVE expression and subsequently characterized. Disruption of the outer membrane resulted in increased uptake of

the small molecule NPN, but also slowed the growth of the cells, indicating diminished cell health. The improvement in a CA-based biocatalyst upon SCVE expression was evaluated by kinetic and functional activity. Expression of SCVE resulted in an increase in per-cell apparent activity as well as an increase in carbonate precipitation with both isoforms of periplasmically expressed CA.

The ability to separately alter activity and transport in the whole cells via genetic engineering opens the door to better biocatalyst design, and thus we explore the impact of the permeabilization on heterogeneous catalysis via estimation of the Thiele modulus and effectiveness factor for the system.

4.3. Materials and Methods

Materials. Chemicals were obtained from Sigma-Aldrich (St. Louis, MO), unless otherwise stated. Custom oligonucelotides were synthesized by Integrated DNA Technologies (IDT; Coralville, IA). Enzymes used in cloning were purchased from New England Biolabs (NEB; Ipswich, MA). Isopropyl β-D-1-thiogalactopyranoside (IPTG) was obtained from Promega Corp. (Madison, WI). BLR(DE3) *E. coli* cells were from Novagen (Billerica, MA).

Cloning. The SCVE gene was synthesized by Epoch Life Science (Sugarland, TX). Oligonucleotides TP55 and TP56 were used to amplify the gene. The PCR product was then digested using the BamHI and EcoRI restriction enzymes. The destination vector pET-2Z (Plasmid 29776; Addgene, Cambridge, MA) was similarly digested and gel-extracted. The digested SCVE fragments were ligated into the digested pET-2Z vector using T4 DNA Ligase, resulting in the plasmid pET2Z-SCVE. BLR(DE3) *E. coli* cells were transformed with this plasmid by electroporation and selected on agar plates containing 50 μg/mL spectinomycin. The

pET2Z-SCVE plasmid was also transformed into BLR-gCab or BLR-gCam cells and selected on agar plates containing 50 μg/mL spectinomycin and 50 μg/mL ampicillin. The SCVE DNA and amino acid sequences, as well as the two primer sequences used for cloning can be found in Table S4-1and Table S4-2.

Protein Expression. SCVE was expressed at 37^{o}C in 10 mL of Luria Broth (LB) supplemented with 50 μg/mL spectinomycin. Cells containing gCab or gCam as well as SCVE were expressed in similar conditions, but also contained 50 μg/mL ampicillin. Cultures were inoculated by diluting overnight cultures at a 1:50 ratio. SCVE expression was induced with1 mM IPTG at OD_{600}=0.6. Induction of gCab and gCam was performed by concurrently adding 0.02% L-arabinose and 1 mM $ZnCl_2$. After 4 hours of expression, the cultures were pelleted by centrifugation at 3,000xg for 10 minutes. The pellets were resuspended in the buffer appropriate for the various assays described below.

NPN Assay. Several versions of a 1-N-phenylnaphthylamine (NPN) uptake assay have been described previously [179-181]. The basic principle is substrate fluorescence upon interaction with the inner lipid membrane and an increase in diffusivity would result in an increase in fluorescence. Here, the whole-cell biocatalysts were resuspended in 5 mM HEPES pH 7.2. A stock solution of NPN containing 5 mM NPN in acetone was diluted to 50 μM in 5 mM HEPES pH 7.2. In a black 96-well plate, 50 μL of 5 mM HEPES pH 7.2 and 100 μL of the cell suspensions were mixed. To initiate the reaction, 50 μL of the diluted NPN solution was added to the wells. After incubation at 25^{o}C for 3 minutes, the fluorescence was measured using excitation and emission wavelengths of 355 nm and 405 nm, respectively, in a SpectraMax M2 spectrophotometer (Sunnyvale, CA).

Kinetic Assays. The stopped-flow kinetic assay used was previously described [142]. Briefly, solutions of 55.6 μM *m*-cresol purple were saturated with CO_2 and N_2 via bubbling of each compressed gas through a glass gas dispersion tube (Ace Glass, Vineland, NJ) at 25°C. These solutions were mixed to vary the concentration of CO_2 from 3 to 28 mM. The whole-cell biocatalysts were diluted in 100 mM Tris at pH 9.0. The concentration of cells in each solution was determined by measuring their optical densities at 600 nm. Using a BioLogic stopped-flow apparatus (BioLogic, Claix, Isère, France) attached to a Jasco J-815 CD Spectrometer (JASCO, Easton, MD), the absorbance at 578 nm was monitored. The data was fit to the differential form of the Michaelis-Menten equation using the Berkeley Madonna software [119]. Each measurement was baseline-corrected by the activity of BLR cells expressing no recombinant CA.

$CaCO_3$ Precipitation. The precipitation assay used was previously described [142]. Briefly, 5 mL of 1 M Tris pH 9.0 was placed in a 15 mL centrifuge tube (Corning, Inc., Tewksbury, MA). After adding the biocatalyst being tested, compressed CO_2 gas was bubbled through each solution for 30 seconds using a glass gas dispersion tube. Immediately after bubbling, calcium chloride ($CaCl_2$) and calcium carbonate ($CaCO_3$) were added to the solution. After incubation at 25°C for 1 hour, the suspension was passed through a spin column (Epoch Life Science, Sugarland, TX) on a vacuum manifold (Qiagen, Valencia, CA). Once they dried, the columns were weighed to determine their total mass. The amount of $CaCO_3$ generated in each sample was determined by subtracting the initial mass of the spin column, the mass of cells added, and the mass of $CaCO_3$ added.

Statistical Analysis. Analysis of variance (ANOVA) was performed using the Minitab program (Minitab Inc., State College, PA). The general linear model (GLM) and the Tukey Method were both used to evaluate the data.

4.4. Results

Expression of SCVE. The SCVE gene was cloned into the pET-2Z vector and this was transformed into BLR(DE3) cells, as well as cells containing CA-encoding plasmids using orthogonal antibotics for selection. The presence of both plasmids in the cells was verified by PCR amplification of both genes. The three whole-cell biocatalysts were named BLR-SCVE, BLR-gCab/SCVE, and BLR-gCam/SCVE. Differential induction of the two different transgenes was accomplished with IPTG for SCVE and arabinose for CA.

Growth Inhibition Curves. To demonstrate the effect of SCVE expression on cell viability and growth rates, the OD at 600nm of the induced and uninduced cultures were measured every hour for 4 hours Figure 4-1). As expected [173], the induced cultures exhibited slower growth as compared to uninduced controls. After 4 hours, the uninduced control cells reached a mean OD_{600} of 3.6. Conversely, BLR-SCVE, BLR-gCab/SCVE, and BLR-gCam/SCVE reached mean final OD_{600} values of 2.7, 2.0, and 2.3, respectively. The diminished growth is indicative of SCVE protein expression.

NPN Permeability. The NPN assay was used to quantify small molecule transport across the outer membrane. The uptake factors, calculated by dividing the background-corrected fluorescence value of each sample by the background corrected fluorescence of NPN alone [179], of induced and uninduced cells harboring the pET2Z-SCVE plasmid can be seen in Figure 4-2. Native BLR cells harboring no recombinant plasmids yielded an uptake factor of 8.0 ± 0.3. BLR-SCVE, BLR-gCab/SCVE, and BLR-gCam/SCVE cells exhibited uptake factors of 9.4 ± 0.2, 9.1 ± 0.5, and 8.5 ± 0.2, respectively. ANOVA on this data indicated a statistically significant difference between the uptake factors of the control cells and each of the permeabilized cells. Post-hoc analysis revealed no statistically significant difference between

BLR-SCVE and BLR-gCab/SCVE cells. These results confirmed that small molecule transport across the outer membrane of *E. coli* cells was enhanced after expression of the SCVE protein.

Enhanced CA Activity. To determine the effect of the SCVE proteins on CA-activity of the whole-cell biocatalysts, apparent activity measurements were performed. The Michaelis-Menten kinetic parameters for native and altered whole-cell biocatalysts can be seen in Table 4-1 - Kinetic parameters w/ and w/o SCVE. The apparent parameters for unpermeabilized BLR-gCab and BLR-gCam were previously published [142]. The rates of the cells expressing the SCVE protein were corrected for the reaction rates of BLR-SCVE cells, which contain no recombinant CA. For the 4 whole-cell biocatalysts evaluated, almost no difference in the apparent K_M was seen (38 mM for BLR-gCab and BLR-gCab/SCVE; 31 mM for BLR-gCam and 34 mM for BLR-gCam/SCVE). Conversely, the per-cell rates of the cells expressing SCVE were higher (3.2×10^{-7} mM sec^{-1} $cell^{-1}$ for BLR-gCab/SCVE and 2.7×10^{-7} mM sec^{-1} $cell^{-1}$) than the unpermeabilized controls (2.5×10^{-7} mM sec^{-1} $cell^{-1}$ for BLR-gCab and 1.9×10^{-7} mM sec^{-1} $cell^{-1}$ for BLR-gCam). These results translate into 29% and 45% enhancements in apparent rate for BLR-gCab/SCVE and BLR-gCam/SCVE cells, respectively, as compared to BLR-gCab and BLR-gCam cells, respectively. Since Cam is the more active CA isoform, it is reasonable to expect cells harboring Cam to experience a larger degree of enhancement upon permeabilization. Also, due to lower levels of protein loading in these cells [142], it is not surprising that the apparent kinetic values do not exceed those of BLR-gCab/SCVE. For both Cab and Cam, these results indicate an increase in diffusion rates of substrate and product across the outer membrane produces increases in the overall apparent reaction rates.

Increased Functional Activity. A model system for carbon mineralization was explored to demonstrate the functional utility of the biocatalysts. Carbon mineralization is a process by

which CO2 is converted to carbonate ions, which combine with divalent cations and precipitate as a thermodynamically stable salt [141]. The mineralization capabilities for the biocatalysts generated in this study were determined by converting gaseous CO2 into calcium carbonate. The masses of $CaCO_3$ precipitated in the presence of various whole-cell biocatalysts can be seen in Figure 4-3. BLR and BLR-SCVE cells expressing no recombinant CA exhibited similar amounts of precipitation, with means of 0.14 and 0.13 g, respectively. The remaining whole-cells yielded mean masses of 0.17, 0.18, 0.23, and 0.24 g of $CaCO_3$ precipitated for BLR-gCab, BLR-gCam, BLR-gCab/SCVE, and BLR-gCam/SCVE, respectively. These values represent improvements in carbon mineralization of 35% and 33% for BLR-gCab and BLR-gCam, respectively, upon SCVE expression.

Two-way ANOVA on this data revealed that cells expressing recombinant CA exhibited statistically significantly higher levels of precipitation than those containing no CA. Also, whole-cell biocatalysts expressing the SCVE protein were found to be statistically significantly different from cells not expressing the protein. Post-hoc analysis revealed no statistical significance in the difference between BLR-gCab/SCVE and BLR-gCam/SCVE, BLR-gCab and BLR-gCam, or BLR and BLR-SCVE cells. These results definitively show an improvement in CO_2 hydration and mineralization upon concomitant expression of CA and SCVE.

4.5. Discussion

The ability to modify both the activity and transport in the biocatalysts allows for the characterization of the system using classical methods developed in the heterogeneous catalysis literature. The effectiveness factor (η) [182] is defined as the whole-cell activity divided by the activity of an equivalent amount of enzyme with no transport barrier. In order to determine the equivalent amount of enzyme for a given number of whole-cell biocatalysts, previously

published values for periplasmic enzyme loading were used [142]. The effectiveness factor can also be used to calculate the Thiele modulus (ϕ), a dimensionless parameter that relates the diffusivity and reaction rate of a catalyst [182].

The Thiele modulus is obtained by performing a dimensionless shell balance on the catalyst considering both diffusion and reaction within the shell. Assuming a spherical catalyst with Michaelis-Menten kinetics, the non-dimensionalized differential equation resulting from this derivation is:

$$\frac{d^2\psi}{d\lambda^2} + \frac{2}{\lambda}\frac{d\psi}{d\lambda} - \phi^2 \frac{\psi}{1+\beta\psi} = 0 \qquad (5)$$

where:

$$\phi = R\sqrt{\frac{V_{max}}{D_e K_M}} \quad (6)$$

and:

$$\beta = \frac{C_S}{K_M} \qquad (7)$$

In Equations 5-7, ψ is the non-dimensionalized concentration (C/C_S), λ is the non-dimensionalized radius (r/R), R is the radius of the catalyst, D_e is the effective diffusivity of the catalyst, and C_S is the bulk concentration of reactant (CO_2) in the extracellular space. Equation 5 can be solved numerically to determine the non-dimensionalized concentration profile in the periplasm for each biocatalyst. For a full derivation of these expressions and the concentration profiles for each whole-cell biocatalyst evaluated, please refer to the Supplementary Information.

To obtain a value for ϕ, the following relationship between the effectiveness factor and Thiele modulus was used [183]:

$$\eta = \left(\frac{3\sqrt{2}}{\phi}\right)\frac{1+\beta}{\beta}\sqrt{\beta - \ln(1+\beta)} \qquad (8)$$

Once the Thiele modulus was calculated, Equation 6 was solved for D_e, which was then calculated. It should be noted here that in these derivations, the specific effects of the outer membrane and periplasmic space are not decoupled. Instead, the membrane and periplasm are considered together, so the parameters calculated are for the overall system. Further, bulk diffusion of the substrate to the surface of the particle was not considered when calculating the effectiveness factor. It was assumed that this bulk diffusion exists in both the whole-cell and free enzyme scenarios and this would cancel each other out. Thus, η only applies to substrate molecules that have reached the biocatalyst interface, not all of the substrate molecules in the reaction solution.

The last parameter calculated to describe the whole-cell biocatalysts was the permeability (P) of the outer membrane to CO_2. The theoretical permeability of BLR-gCab and BLR-gCam was calculated by [184]:

$$P = \left(\frac{D}{d}\right)\left(\frac{a_0}{A}\right)\left(\frac{a}{a_0}\right) \qquad (9)$$

where D is the free diffusivity of CO_2 (1.94×10^3 μm^2/sec) [185], d is the membrane thickness (7.8×10^{-3} μm) [186], a_0 is the cross-sectional area of all of the pores present in the outer membrane (0.113 μm^2) [184], A is the total surface area of the outer membrane (3.00 μm^2) [184], and a/a_0 is the Renkin correction factor, a relationship between the effective pore area (a) and a_0. It was calculated using [184]:

$$\frac{a}{a_0} = \left[1 - \left(\frac{r_{CO2}}{R_p}\right)^2\right] * \left[1 - 2.104\left(\frac{r_{CO2}}{R_p}\right) + 2.09\left(\frac{r_{CO2}}{R_p}\right)^3 - 0.95\left(\frac{r_{CO2}}{R_p}\right)^5\right] \quad (10)$$

where r_{CO2} is the solute radius and R_p is the pore radius (5.8 Å) [184]. The solute radius of CO_2 was calculated by:[187]

$$r_{CO2} = \sqrt[3]{\frac{3M}{4\pi\rho N_A}} \quad (11)$$

where M is the molecular weight of the solute (44 g/mol), ρ is the density of a solution of the solute being evaluated ($\rho_{CO2} = \rho_{H2O}$ = 1 g/mL), and N_A is Avogadro's number. Once P was calculated for BLR-gCab and BLR-gCam, it was used to calculate P for the cells expressing the SCVE protein. To do so, the following expression was used to determine a partition coefficient (K) as a function of D_e for both biocatalysts [188].

$$P = \frac{KD_e}{d} \quad (12)$$

Then, using the D_e for each SCVE-expressing biocatalyst and its corresponding K, the permeability for the permeabilized cells was calculated. Table 4-2 contains the values for η, ϕ, D_e, and P for the 4 whole-cell biocatalysts quantified using these calculations.

The calculations show an increase in effectiveness factor of about 100% upon permeabilization with SCVE expression for biocatalysts containing both Cab and Cam. This roughly translates into a 50% reduction in the Thiele modulus, a 3.5-fold increase in diffusivity, and an increase in permeability of about 2.5-fold. The biocatalyst found to have the highest permeability was BLR-gCam/SCVE, for which P was found to be approximately 4.4 x 10^3 µm/sec. The calculated permeability was used to estimate the expression yield necessary to obtain such a value. By using the properties of an SCVE-generated pore described above, it was estimated that the

expression yield would be 18 mg of SCVE per L of culture in order to achieve this permeability. Previously published reports have shown recombinant porin expression yields of 20-25 mg/L of culture in *E. coli* [189, 190]. Another report of outer-membrane protein expression showed a yield of 12 mg/L of culture after purification [191]. Given that the protein recovery from each step required in protein purification could be as low as 70% [192], the actual yield could be much higher. Finally, the expression of native outer membrane proteins such as OmpA, OmpX, and OmpT have been shown to reach yields of 150-170 mg/L of culture in *E. coli* [193]. Thus, the estimated protein yield seems reasonable and consistent with values found by other groups.

4.6. Conclusions

Recombinant expression of the SCVE viroporins in *E. coli* resulted in the improvement of CA-based whole-cell biocatalysts. By introducing additional pores to the outer membrane of the cells, the diffusivity of small molecules across the outer membrane was enhanced. This translated into increased apparent catalytic activity. These improvements were measured experimentally, the data from which was then used to quantify the enhancement using principles of diffusion-reaction systems. This system could very easily be applied to other biocatalysts whose catalytic components (most commonly enzymes) are relegated to the periplasmic space of the cell. Overall this work demonstrates that synthetic biology techniques can be used to design and build improved heterogeneous catalysts which will facilitate applications such as carbon capture and sequestration.

4.7. Acknowledgements

We would like to thank the US Department of Energy for financially supporting this work (ARPA-e DE-AR0000100).

4.8. Figures and Tables

Figure 4-1 - Growth retardation curves w/ and w/o SCVE

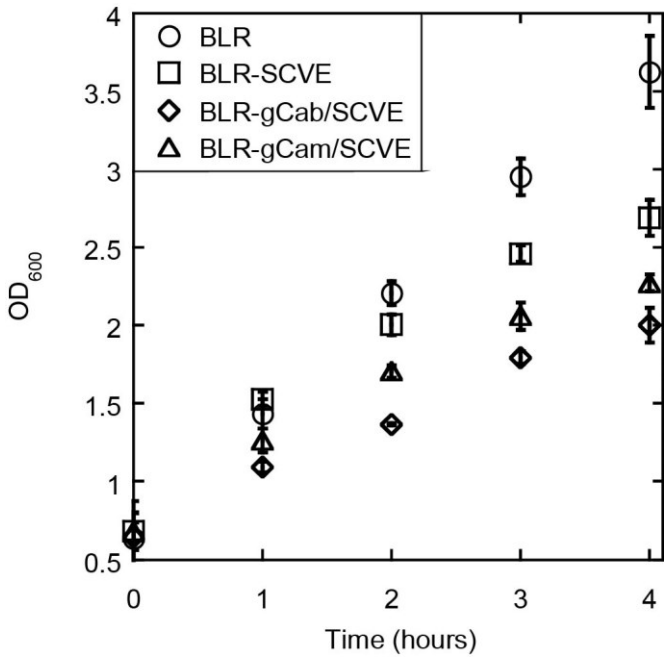

Growth retardation curves presented as OD_{600} vs. Time post-induction for all whole-cell biocatalysts evaluated. All measurements were performed in triplicate, with the error bars representing the standard deviations from the means.

Figure 4-2 - NPN Uptake Factors w/ and w/o SCVE

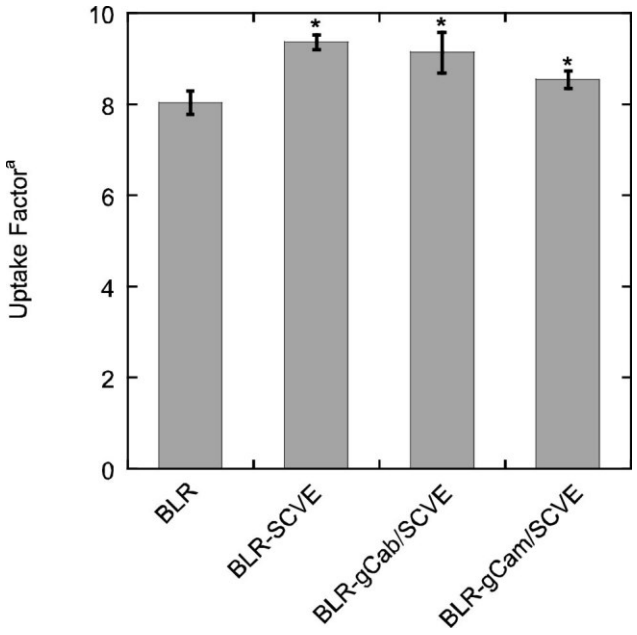

1-N-phenylnaphthylamine (NPN) uptake factors for the various whole-cell biocatalysts evaluated. Uptake factors are defined as the fluorescence of the biocatalyst divided by the fluorescence of the NPN solution alone. All measurements were performed in triplicate, with the error bars representing the standard deviations from the means.

Figure 4-3 - CaCO3 precipitation w/ and w/o SCVE

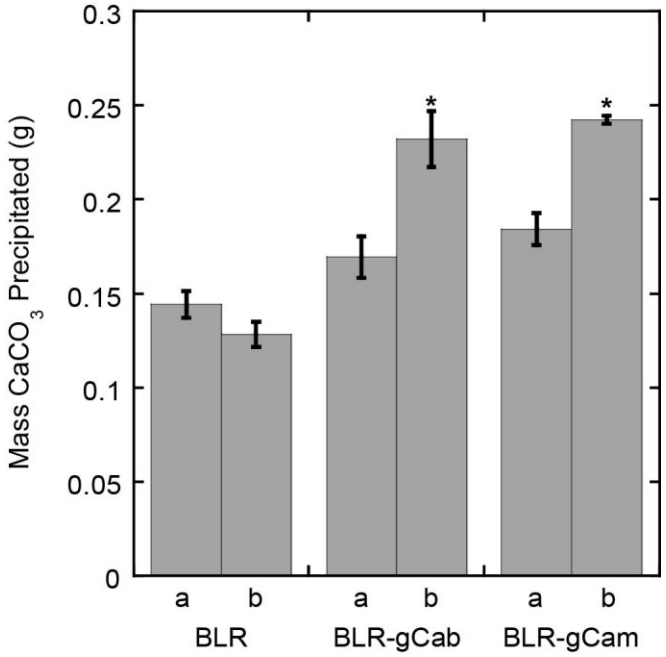

*Indicates statistically significant increase in uptake factor relative to controls

Calcium carbonate ($CaCO_3$) precipitation amounts for the various whole-cell biocatalysts evaluated. In each case, the cells were tested (a) without SCVE expression, and (b) with SCVE expression. All measurements were performed in triplicate, with the error bars representing the standard deviations from the means.

*Indicates statistically significant improvement in precipitation relative to controls.

Table 4-1 - Kinetic parameters w/ and w/o SCVE

Catalyst	V_{max}/cell (mM sec^{-1} $cell^{-1}$)	K_M (mM)	V_{max}/K_M/cell (sec^{-1} $cell^{-1}$)
BLR-gCab[a]	$2.5 \pm 0.6 \times 10^{-7}$	38 ± 5	6.5×10^{-9}
BLR-gCab/SCVE	$3.2 \pm 0.4 \times 10^{-7}$	38 ± 2	8.4×10^{-9}
BLR-gCam[a]	$1.9 \pm 0.4 \times 10^{-7}$	31 ± 3	6.0×10^{-9}
BLR-gCam/SCVE	$2.7 \pm 0.5 \times 10^{-7}$	34 ± 2	8.0×10^{-9}

[a]Previously published values [45]

Measurements were performed in triplicate, with errors indicating standard deviations from the means.

Table 4-2 - Calculated diffusion-reaction parameters w/ and w/o SCVE

Catalyst	η	ϕ	D_e (μm^2 sec^{-1})	P_{CO2} (μm sec^{-1})
BLR-gCab	0.21	22	0.83×10^{-3}	1.7×10^{3}
BLR-gCab/SCVE	0.43	11	2.9×10^{-3}	4.1×10^{3}
BLR-gCam	0.28	17	2.0×10^{-3}	1.7×10^{3}
BLR-gCam/SCVE	0.58	8.1	7.3×10^{-3}	4.4×10^{3}

4.9. Supplementary Information

Table S4-1 - Nucleotide and amino acid sequences for SCVE

Polymer	Sequence
Nucleotide Sequence	**5'-**atgtatagctttgtgagcgaagaaaccggcaccctgattgtgaacagcgt gctgctgtttctggcgtttgtggtgtttctgctggtgaccctggcgattc tgaccgcgctgcgcctgtgcgcgtattgctgcaacattgtgaacgtgagc ctggtgaaaccgaccgtgtatgtgtatagccgcgtgaaaaacctgaacag cagcgaaggcgtgccggatctgctggtg**-3'**
Amino Acid	**N-**MYSFVSEETG TLIVNSVLLF LAFVVFLLVT LAILTALRLC AYCCNIVNVS LVKPTVYVYS RVKNLNSSEG VPDLLV**-C**

Table S4-2 - Primers for SCVE cloning

Primer	Description	Sequence
TP55	SCVE Forward BamHI	AGT GAC GGA TCC ATG TAT AGC TTT GTG AGC
TP56	SCVE Reverse EcoRI	AGT GAC GAA TTC TTA CAC CAG CAG ATC C

*Underlined sequences indicate restriction sites

Derivation for obtaining Thiele Modulus with Michaelis-Menten Kinetics

The following derivation is adapted from one that has been previously published for porous spherical catalysts with first-order kinetics [182].

Figure S4-1 - Diagram of shell for Thiele modulus derivation

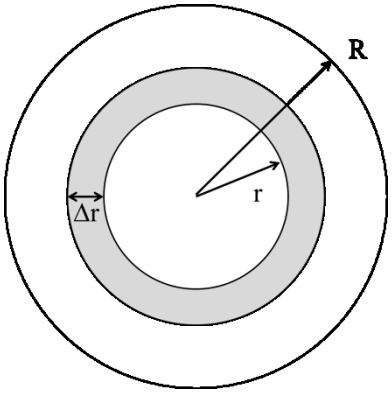

Reaction/Diffusion Shell Balance

$$W_{Ar}4\pi r^2|_r - W_{Ar}4\pi r^2|_{r+\Delta r} + r_S 4\pi r^2 \Delta r = 0 \quad (1)$$

Divide the whole equation by $4\pi\Delta r$ and take the limit as $\Delta r \to 0$

$$\frac{d}{dr}(W_{Ar}r^2) + r_S r^2 = 0 \quad (2)$$

Fick's Law of Diffusion:

$$W_{Ar} = -D_e \frac{dC}{dr} \quad (3)$$

Substitute Equation 3 into Equation 2:

$$\frac{d}{dr}\left(-D_e r^2 \frac{dC}{dr}\right) + r_S r^2 = 0 \quad (4)$$

Differentiate the first term of Equation 4 and simplify to remove coefficient of second derivative:

$$-2rD_e \frac{dC}{dr} - D_e r^2 \frac{d^2C}{dr^2} + r_S r^2 = 0 \quad (5)$$

$$\frac{d^2C}{dr^2} + \frac{2}{r}\frac{dC}{dr} - \frac{r_S}{D_e} = 0 \quad (6)$$

Set the boundary conditions to be:

$$\frac{dC}{dr} = 0 \text{ @ } r = 0; C = C_S \text{ @ } r = R \quad (7)$$

In order to obtain the Thiele Modulus from Equation 6, it first needs to be nondimensionalized using the variables:

$$\psi = \frac{C}{C_S};\ \lambda = \frac{r}{R} \quad (8)$$

Nondimensionalizing the boundary conditions as well yields:

$$\frac{d\psi}{d\lambda} = 0 \text{ @ } \lambda = 0; \psi = 1 \text{ @ } \lambda = 1 \quad (9)$$

Use the chain rule to obtain equivalent differentials to those in Equation 6:

$$\frac{dC}{dr} = \frac{dC}{d\lambda}\frac{d\lambda}{dr} = \frac{d\psi}{d\lambda}\frac{dC}{d\psi}\frac{d\lambda}{dr} = \frac{C_S}{R}\frac{d\psi}{d\lambda} \quad (10)$$

$$\frac{d^2C}{dr^2} = \frac{d}{dr}\left(\frac{dC}{dr}\right) = \frac{d}{d\lambda}\frac{d\lambda}{dr}\left(\frac{C_S}{R}\frac{d\psi}{d\lambda}\right) = \frac{C_S}{R^2}\frac{d^2\psi}{d\lambda^2} \quad (11)$$

Nondimensionalize the Michaelis-Menten equation:

$$r_S = \frac{V_{max}C}{K_M + C} = \frac{V_{max}C_S\psi}{K_M + C_S\psi} = \frac{V_{max}\psi}{K_M/C_S + \psi} = \frac{C_S}{K_M}\frac{V_{max}\psi}{1 + \psi C_S/K_M} = \frac{C_S}{K_M}\frac{V_{max}\psi}{1 + \beta\psi} \quad (12)$$

Where:

$$\beta = \frac{C_S}{K_M} \quad (13)$$

Substitute Equations 10, 11, and 12 into Equation 6:

$$\frac{C_S}{R^2}\frac{d^2\psi}{d\lambda^2} + \frac{2}{\lambda R}\frac{C_S}{R}\frac{d\psi}{d\lambda} - \frac{1}{D_e}\frac{C_S}{K_M}\frac{V_{max}\psi}{1 + \beta\psi} = 0 \quad (14)$$

Simplify to remove the coefficient of the second derivative as before to obtain:

$$\frac{d^2\psi}{d\lambda^2} + \frac{2}{\lambda}\frac{d\psi}{d\lambda} - \phi^2\frac{\psi}{1 + \beta\psi} = 0 \quad (15)$$

Where the Thiele Modulus is represented by:

$$\phi = R\sqrt{\frac{V_{max}}{D_e K_M}} \quad (16)$$

This expression for the Thiele Modulus was confirmed with another previously published derivation, achieved by a different method [194].

The following numerical approach for solving Equation 15 (a non-linear second-order differential equation) is adapted from a method previously published [183]. To numerically solve the equation, it must first be split into 2 first-order differential equations. A new variable must be introduced to do so:

$$z = \frac{d\psi}{d\lambda} \quad (17)$$

Thus,

$$\frac{dz}{d\lambda} = \frac{d^2\psi}{d\lambda^2} = -\frac{2}{\lambda}z + \phi^2\frac{\psi}{1+\beta\psi} \quad (18)$$

This transformation also requires transforming the boundary conditions:

$$z = 0 \ @ \ \lambda = \frac{R_C}{R}; \psi = 1 \ @ \ \lambda = 1 \quad (19)$$

where R_C/R is the lower boundary that defines the start of the periplasmic space. For this solution, this parameter was set at 0.9, indicating that the periplasm's thickness is the outer 10% of the cell's radius. The boundary value problem defined by Equations 17, 18, and 19 was solved using the MATLAB software (R2009b, MathWorks, Natick, MA). The code used, which appears in Figure S4-2, is a modified version of previously written code [195].

Figure S4-2 - MATLAB code used to solve 2nd order BVP

```
function bvp4
%x represents lambda, y represents psi
xlow=0.9; xhigh=1;  %sets shell across which profiles are calculated
solinit=bvpinit(linspace(xlow,xhigh,10),[0 1]); %defines mesh and initial
guesses
sol=bvp4c(@bvp4ode,@bvp4bc,solinit);
xint=linspace(xlow,xhigh,20);  %defines linspace for solution
Sxint=deval(sol,xint);         %evaluates solution
plot(xint,Sxint(1,:))   %plots psi vs lambda
%--------------------
function dydx=bvp4ode(x,y)  %defines ODEs
a=22;   %thiele modulus - varies by biocatalyst
b=0.87; %beta as defined in Equation 13 - varies by biocatalyst
dydx(1,1)=y(2); %the first first-order ODE
dydx(2,1)=-(2/x)*y(2)+(a^2)*(y(1)/(1+b*y(1))); %the second first-order ODE
%--------------------
function res=bvp4bc(ya,yb)  %defines boundary conditions
res=[yb(1)-1 ya(2)];        %bc's described by equations that equal 0
```

Equation being solved is defined in Equation 15 above.

The resulting solution for each of the 4 biocatalysts tested can be seen in Figure S4-3. In this plot, biocatalysts with higher diffusivities, and thus higher overall reaction rates, result in flatter nondimensionalized concentration profiles. This is because with increased permeability, the periplasmic and extracellular spaces are able to more easily equilibrate, and thus the gradient between the two spaces is decreased.

Figure S4-3 - Concentration profiles for cells w/ and w/o SCVE

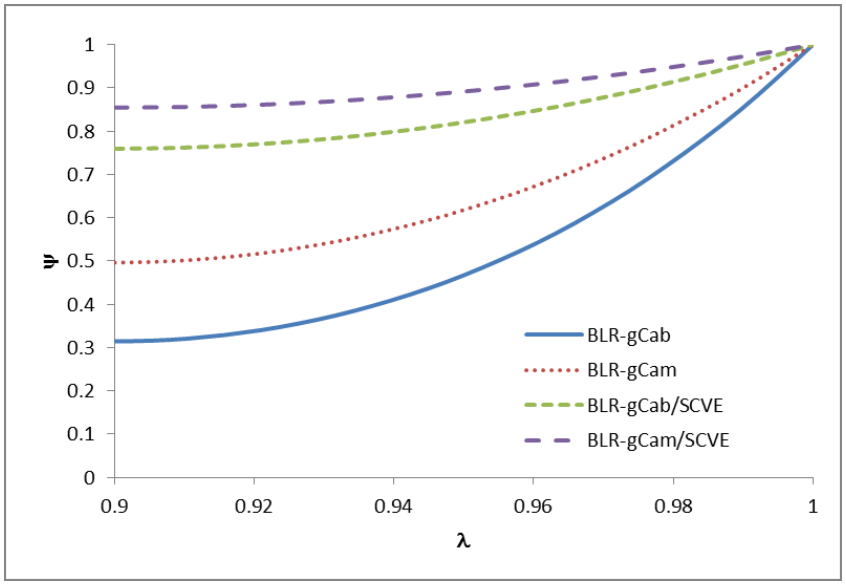

Nondimensionalized concentration profiles for unpermeabilized and permeabilized whole-cell biocatalysts

Derivation for relationship between η and ϕ with Michaelis-Menten Kinetics

To begin, we define the effectiveness factor in general terms:

$$\eta = \frac{Overall\ Reaction\ Rate}{Reaction\ Rate\ without\ Diffusion\ Barrier} \quad (20)$$

Next, apply those terms to our whole-cell biocatalysts.

$$\eta = \frac{Whole-cell\ Activity}{Equivalent\ Enzymatic\ Activity} \quad (21)$$

Substituting expressions for each term:

$$\eta = \frac{\frac{A_p}{V_p} D_e \left.\frac{dC}{dr}\right|_{r=R}}{\frac{V_{max} C_s}{K_M + C_s}} \quad (22)$$

Where Ap and Vp are the surface area ($4\pi R^2$) and volume ($4\pi R^3/3$), respectively. Substituting in these expressions and simplifying gives:

$$\eta = \frac{3D_e}{RV_{max}} \frac{K_M + C_s}{C_s} \left(\left.\frac{dC}{dr}\right|_{r=R} \right) \quad (23)$$

In order to simplify this expression further, we need an expression for the final term. To obtain such an expression, we begin with the same shell balance above:

$$W_{Ar} 4\pi r^2|_r - W_{Ar} 4\pi r^2|_{r+\Delta r} + r_S 4\pi r^2 \Delta r = 0 \quad (1)$$

Divide by $4\pi r^2 \Delta r$, take the limit as $\Delta r \to 0$, substitute Fick's Law of Diffusion for W_{Ar} and the Michaelis-Menten rate equation for r_S:

$$D_e \frac{d^2 C}{dr^2} = \frac{V_{max} C}{K_M + C} \quad (24)$$

Using the chain rule, apply the transformation:

$$\frac{d^2 C}{dr^2} = \frac{1}{2} \frac{d}{dC} \left(\frac{dC}{dr} \right)^2 \quad (25)$$

Substituting this expression into Equation 24 and simplifying the expression gives:

$$d \left(\frac{dC}{dr} \right)^2 = \frac{2V_{max}}{D_e} \frac{C}{K_M + C} dC \quad (26)$$

Taking the integral of both sides and rearranging the integrand yields:

$$\left(\frac{dC}{dr}\right)^2 = \frac{2V_{max}}{D_e}\int \frac{C/K_M}{1+\frac{C}{K_M}}dC \quad (27)$$

In order to integrate this function, a *u*-substitution must be used where:

$$u = {}^{C}/_{K_M}\,; du = \frac{1}{K_M}dC \quad (28)$$

Making this substitution gives:

$$\left(\frac{dC}{dr}\right)^2 = \frac{2V_{max}}{D_e}\int \frac{u}{1+u}K_M dC = \frac{2V_{max}K_M}{D_e}\int \frac{u}{1+u}dC \quad (29)$$

Integrate this expression, re-substitute for *u*, and take the square root of each side:

$$\frac{dC}{dr} = \left(\frac{2V_{max}K_M}{D_e}\left[\frac{C}{K_M} - \ln\left(1+\frac{C}{K_M}\right)\right]\right)^{1/2} \quad (30)$$

In order to substitute this expression into the one for η, it needs to be evaluated at $r=R$ where $C=C_s$:

$$\left.\frac{dC}{dr}\right|_{r=R} = \left(\frac{2V_{max}K_M}{D_e}\left[\frac{C_s}{K_M} - \ln\left(1+\frac{C_s}{K_M}\right)\right]\right)^{1/2} \quad (31)$$

Substitute Equation 31 into Equation 23 and then substitute Equation 13 where necessary:

$$\eta = \frac{3D_e}{RV_{max}}\frac{1+\beta}{\beta}\left(\frac{2V_{max}K_M}{D_e}[\beta - \ln(1+\beta)]\right)^{1/2} \quad (32)$$

Simplifying this expression gives:

$$\eta = \frac{3\sqrt{2}}{R}\left(\frac{D_e K_M}{V_{max}}\right)^{1/2}\frac{1+\beta}{\beta}([\beta - \ln(1+\beta)])^{1/2} \quad (33)$$

Finally, substitute Equation 16 into Equation 33:

$$\eta = \frac{3\sqrt{2}}{\phi}\frac{1+\beta}{\beta}([\beta - \ln(1+\beta)])^{1/2} \quad (33)$$

5. Improved Functionality of Whole-cell Biocatalysts

Note: A version of this chapter entitled "Surface display of small peptides on Escherichia coli for enhanced calcite (CaCO3) precipitation rates." has been accepted for publication in *Biopolymers: Peptide Science* (2014) and is currently in press.

TNP designed and performed all experiments, analyzed the data, and wrote the manuscript.

5.1. Abstract

Mineralization has emerged as a promising strategy for long-term carbon sequestration. These processes involve carbon dioxide hydration followed by mineral precipitation. We have explored the production of whole-cell biocatalysts engineered with carbonic anhydrase (CA) activity to accelerate the CO_2 hydration reaction. In this study, short polypeptides were displayed on the surface of *E. coli* cells and whole-cell biocatalysts containing periplasmically expressed CAs in an attempt to enhance calcite mineral formation. It was found that cells co-expressing recombinant periplasmic CA and surface-displayed GPA peptide (PEVPEGAFDTAI) outperformed other peptide-expressing biocatalysts evaluated in terms of the amount of precipitate formed, as well as the overall formation rate of solids. Cells expressing the Cab CA isoform (BLR-pCab) and Cam isoform (BLR-pCam) with the surface-displayed GPA peptide exhibited 36% and 67% improvements in precipitation amounts, as well as 18% and 60% improvements in overall formation rates, respectively, over similar biocatalysts without GPA expression. These results demonstrate that synthetic biology approaches can be used to create novel biocatalysts with the ability to enhance both catalysis and precipitation activities.

5.2. Introduction

There has been recent interest in the development of chemical processes using ambient CO_2 but the hydration of CO_2 can be a rate limiting step in liquid-phase reactions. We have been interested in the mineralization of CO_2, a process in which gaseous CO_2 is captured and stored in

mineral carbonates, primarily calcite ($CaCO_3$) [196-198]. One method to accelerate CO_2 hydration is through the use of carbonic anhydrases (CA; EC 4.2.1.1) [143], a class of enzymes able to hydrate CO_2 into HCO_3^- and CO_3^{-2} [41]. CAs are ubiquitous metalloenzymes with bound Zn^{+2} ions that are responsible for this activity, which can have rate constants as high as 10^4-10^6 sec^{-1} [42]. Several groups have used CAs to generate whole-cell biocatalysts in yeast [141] and *E. coli* [30, 142, 178] for carbon mineralization. In many of these studies, the biocatalysts have been shown to increase the amount of calcite formed. However, we believe there is an opportunity for further improvement by enhancing calcite precipitation rates in addition to the amount of precipitate generated.

The precipitation of a solid compound can usually be divided into three distinct processes: supersaturation of the solution, nucleation, and growth [199]. Once the concentration of a given compound exceeds its solubility at a set of conditions (supersaturation), interactions between the dissolved molecules result in a phase transition from an aqueous to a solid state (nucleation) [200]. Subsequently, these nucleated molecules form "active sites" on which additional molecules spontaneously deposit (growth) [199]. In general, precipitation is a thermodynamic process by which the Gibbs free energy of a supersaturated solution is minimized. Although there are entropic penalties associated with this organization of molecules, the energetic benefits outweigh these effects [200].

Efforts to manipulate calcite precipitation have previously employed natural proteins from sea creatures [201, 202], as well as synthetic materials [199], and peptides, primarily poly-aspartate [203, 204] which has a strong negative charge, but others as well [205]. When added to a solution containing calcium and carbonate ions, these materials were able to alter the morphology of the crystals formed, but in many cases the precipitation rates were decreased.

However, immobilization of poly-aspartic acids on a solid support made of chitosan was shown to improve the rate of calcite formation [202]. Further, yeast surface display of the GPA peptide, which is derived from the calcium-binding site of glycophorin A [206] was shown to increase the amount of precipitate formed, but the kinetics of this process were not evaluated [141].

In this study, a poly-aspartate 20-mer (D20), the GPA peptide, and the FLK peptide were immobilized on the surface of *E. coli* cells via fusion to the C-terminus of the eCPX protein [207]. The FLK peptide is a 12-mer peptide with 4 repeats of the amino acid sequence FLK [141]. This peptide has a net positive charge, and was used as a negative control. A FLAG peptide tag was fused to each peptide for verification of successful surface expression and thus cells expressing the FLAG tag alone were also investigated. The eCPX protein used for cell-surface display was created via circular permutation of the native OmpX membrane protein, which allows both termini of the eCPX protein to be exposed to the extracellular space. We hypothesize that expression of these peptides on the surface of the bacteria cells places them in a region of high $CO3^{-2}$ concentration, enabling them to enhance the amount and formation rate of calcite crystals. Of the peptides cloned, all but D20 successfully expressed under the conditions used. Of those that expressed, the highest level of calcite precipitation was seen in the presence of the GPA peptide. This fusion was then also expressed in whole-cell biocatalysts containing the Cab (Methanobacterium thermoautotriphicum; PDB:1G5C) [45] and Cam (Methanosarcina thermophila; PDB:1THJ) [51] isoforms of CA periplasmically expressed using the pelB leader peptide. These biocatalysts were named BLR-pCab and BLR-pCam [142]. Using these surface-modified whole-cell biocatalysts, the precipitation amounts and overall formation rates were improved to a significant degree over their unmodified counterparts.

5.3. Materials and Methods

Materials. All chemicals were purchased and used without further purification from Sigma-Aldrich (St. Louis, MO), unless specified. Oligonucleotides were obtained from Integrated DNA Technologies (Coralville, IA). SfiI and T4 DNA ligase were purchased from New England Biolabs (Ipswich, MA). BLR(DE3) *E. coli* cells were purchased from Novagen (Billerica, MA). Isopropyl β-D-1-thiogalactopyranoside (IPTG) was purchased from Promega (Madison, WI).

Cloning. Forward primer TP49 was used to amplify the eCPX gene from the pB33eCPX vector (Plasmid 23336; Addgene, Cambridge, MA) with reverse primer TP50, TP57, TP58, or TP59, which fused the D20, FLAG, GPA, or FLK peptide, respectively, to the C-terminus of the eCPX protein with a linker (N-GGQSGQ-C). The oligonucleotides also fused a FLAG tag to the D20, GPA, and FLK peptides with a linker (N-GGGS-C). Thus, the constructs created were of the form: eCPX-GGQSGQ-peptide-GGGS-FLAG, as shown in Figure 5-1. The only exception was the construct made using TP49/TP57, which contained no peptide, but did contain the FLAG tag. This construct was of the form: eCPX-GGQSGQ-FLAG. The oligonucleotide sequences can be seen in Table S5-1 along with the amino acids sequences of each peptide. The amplified fragments and pB33eCPX vector were digested with SfiI, gel extracted, and ligated together. The plasmid was electroporated into BLR(DE3) cells and selected on agar plates supplemented with 35μg/mL chloramphenicol. The pB33eCPX-GPA plasmid was also transformed into BLR-pCab and BLR-pCam cells and selected on agar plates containing 35 μg/mL chloramphenicol (Cm) and 50μg/mL kanamycin (Kan).

Expression. Protein expression was performed at 37^{o}C in 10mL of Luria Broth (LB) supplemented with the appropriate antibiotic(s). For cells expressing CA and eCPX simultaneously, 1mM $ZnCl_2$ was also added to the media. A 1:50 dilution of an overnight

culture was induced with 0.04% L-arabinose at OD_{600nm}=0.6. If present, CA was induced simultaneously with 200μM IPTG. After 4 hours of expression, the cells were harvested by centrifugation at 5000xg for 5min. The pellets were resuspended in 1M Tris pH 9.0, henceforth referred to as T9.

Precipitation Assay. The precipitation assay used was a modification to an assay previously described [142]. Briefly, CO_2 was bubbled through 5mL of T9 containing the whole-cell biocatalyst in for 30s. $CaCl_2$ (0.5mL of 0.5g/mL in T9) was immediately added to the tube. After 1 hour at 25°C, the precipitate was separated from the solution and dried on a vacuum manifold (Qiagen, Valencia, CA) using spin columns (Epoch Life Science, Sugarland, TX). The mass of precipitate formed was calculated by subtracting the masses of the empty column and cells added, which are determined before bubbling, from the final mass of the column.

Overall Formation Rate Assay. Whole-cell biocatalysts were diluted to an OD_{600nm}=0.3 in T9. In a 1cm cuvette, 1mL of this suspension was mixed with 1 mL of 3M $CaCl_2$ in T9. The cuvette was placed in a Jasco J-815 CD Spectrometer (JASCO, Easton, MD) fitted with a Peltier temperature control stage (set to 25°C with stirring) and monochromator. After adding 1mL of CO_2-saturated ddH_2O to the cuvette, the absorbance at 600nm was monitored for 10min. The resulting curves were fit to the Hill equation, as described in section 3.3.

Statistical Analysis. Analysis of variance (ANOVA) using the General Linear Model and post-hoc analysis using the Tukey method were performed using the Minitab program (Minitab, Inc., State College, PA).

5.4. Results

eCPX Expression. The FLAG, D20, GPA, and FLK peptides were all successfully fused to the 3' end of the eCPX gene and confirmed by DNA sequencing. All constructs followed the scheme

shown in Figure 5-1. The FLAG peptide was fused to the D20, GPA, and FLK peptides for confirmation of expression. All fusions were made to the C-terminus of the eCPX protein so that only fully expressed and translocated fusions would result in surface-displayed peptide. All 4 plasmids were electroporated into BLR(DE3) cells. After transformation, the FLAG, GPA, and FLK peptides were all successfully expressed, as confirmed by flow cytometry (Figure S5-1). Under the conditions tested, the D20 peptide was not found to be displayed on the surface of the cells as determined by the lack of detection of the FLAG peptide. This may be due to inefficiencies with translocation of poly-aspartic acid through the inner and outer membranes. For BLR-pCab and BLR-pCam cells transformed with the pB33eCPX-GPA plasmid, PCR amplification was used to verify the presence of both plasmids. Expression of eCPX was again confirmed by flow cytometry (Figure S5-2). The biocatalysts generated were called BLR-FLAG, BLR-GPA, BLR-FLK, BLR-pCab/GPA, and BLR-pCam/GPA. Expression was selectively induced by using L-arabinose for the eCPX fusions, and IPTG for the CAs.

$CaCO_3$ Precipitation. The amount of calcite precipitate formed in the presence of the 3 surface-displayed peptides evaluated can be seen in Figure 5-2A. This assay measured the amount of hydrated CO_2 that can be converted to calcite by the various immobilized peptides. Native BLR cells, BLR-FLAG, BLR-GPA, and BLR-FLK cells generated 0.08, 0.11, 0.11, and 0.09 g of $CaCO_3$, respectively. ANOVA on this data showed no statistically significant difference between BLR and BLR-FLK cells, as expected due to the positive charge of the FLK peptide. This analysis also revealed no statistically significant difference between BLR-FLAG and BLR-GPA cells, both of which were significantly better than BLR cells. Thus, the GPA peptide was selected for further experimentation.

The amount of precipitate formed in the presence of the whole-cell biocatalysts with and without surface-displayed GPA can be seen in Figure 5-2B. Using BLR cells, the GPA peptide increased the amount of calcite formed by 38% over unmodified cells. Similarly, display of the GPA peptide in BLR-pCab and BLR-pCam cells enhanced precipitation by 36% and 59%, respectively, over their unmodified counterparts. Two-way ANOVA on this data revealed that the GPA peptide and recombinant CA each had a statistically significant impact on the amount of calcite precipitated. Further, this analysis also showed a statistically significant difference between the cells expressing both the GPA peptide and CA, and those possessing one or none of these modifications. However, neither factor was a greater contributor to the improvement in precipitation than the other; both were necessary to achieve the maximum enhancement.

$CaCO_3$ Formation Rates

As a proxy for direct measurement of precipitation rates, the solution turbidity against time was measured. Although methods exist that can specifically measure calcium ion concentrations within a solution, such methods can be noisy and are highly dependent on the calibration method used. Thus, turbidity was used as a quick and simple method for tracking solids formation and this was accomplished by measuring the absorbance at 600 nm. In this method, the absorbance at 600 nm was used as an indicator of solids formation. To quantify the rate of turbidity change, the raw absorbance data was fit to the sigmoidal Hill equation below [208]:

$$A_{600} = (A_{600})_0 + \frac{(A_{600})_{Amp} t^{\alpha}}{{t_m}^{\alpha} + t^{\alpha}} \quad (1)$$

where A_{600} is the absorbance at 600nm, $(A_{600})_0$ is the initial absorbance, $(A_{600})_{Amp}$ is the amplitude of the absorbance change, t is the time, t_m is the time where the slope is the greatest, and α is the Hill coefficient. An example of the raw data and fit can be seen in Figure 5-3. The t_m was

selected for comparison of the various samples. A lower value in this parameter indicated an enhancement in formation rate since the maximum slope was achieved at an earlier time. The results of this analysis can be seen in Table 5-1. From this experiment, a 5% reduction in t_m was observed upon expression of GPA on BLR cells. In BLR-pCab and BLR-pCam cells, the respective t_m's were reduced by18% and 60%. For comparison, the GPA peptide was previously displayed on the surface of yeast cells and was shown to improve the CaCO3 mineralization rate by 30% over yeast cells displaying no peptide [141]. However, these results are not directly comparable to those reported in this study due to differences in the experimental methods. Two-way ANOVA on this data showed a statistically significant difference between cells expressing the GPA peptide and those without any surface-displayed peptide. It also demonstrated a significant difference between cells with and without recombinant CA. Further, the isoform of CA had a statistically significant impact on the change in turbidity. As above, the effects of recombinant CA and surface-displayed GPA were not additive; the maximum enhancement observed with both modifications was greater than the sum of the individual improvements.

5.5. Discussion

Synthetic biology is rapidly gaining interest due to the opportunity it presents to design and implement biological systems in research and industrial applications. In this work, we created novel whole-cell biocatalysts for carbon mineralization, an emerging technology with the potential for a significant environmental impact. We show improved precipitation of calcium carbonate through surface-display of small peptides on *E. coli* cells containing periplasmically-expressed CA enzymes. In doing so, we demonstrate the incorporation of multiple genetic

modifications can be used to significantly enhance the functional activity of a whole-cell biocatalyst.

Four peptide sequences were evaluated, and the cells expressing the GPA peptide were found to produce the highest amount of calcite precipitation. Interestingly, the amount was not significantly different from what was seen with the cells expressing the FLAG sequence alone, which was included as a negative control. This result was surprising since the FLAG tag had not been previously identified as a potential peptide for precipitation enhancement. However, given its aspartic acid content (62.5%), it is not completely unexpected. It is also interesting to note that when fused to another peptide, namely the GPA or FLK peptides, the FLAG tag does not seem to enhance the precipitation capabilities of the peptide. For example, if the FLAG tag conferred an improvement in precipitation, a significant difference between BLR-FLK cells and BLR cells would be expected. We speculate that when it is farther from the surface of the cell, the FLAG tag can experience a wider variety of conformations, causing the probability of binding a calcium ion to be decreased. However, when expressed alone it is not as flexible and is able to facilitate $CaCO_3$ formation.

The results demonstrate that the immobilization of the GPA peptide on the surface of BLR-pCab and BLR-pCam cells yielded the best-performing whole-cell biocatalysts and there may be several reasons for the observed improvements. Since precipitate growth is relatively spontaneous (mostly dependent on saturation conditions of the solution), supersaturation and nucleation are most likely the rate-limiting steps of precipitation. In our biocatalysts, the surface-displayed GPA peptide could enhance nucleation of $CaCO_3$, resulting in the onset of precipitation. We speculate that immobilization of the unstructured peptides on the cell surface could cause a reduction in the entropic flexibility of the peptide. With one end fixed, the number

of conformations available to the peptide are limited, which may increase the probability of a peptide-calcium interaction. This interaction could then cause the nucleation of initial calcite crystals upon which subsequent molecules can deposit.

Further, given that the enzymes are located inside the periplasm, it can be assumed that the highest concentration of carbonate ions would be near the surface of the cell. Thus, immobilizing the GPA peptide at the cell surface likely positions it in a region with supersaturation above that of the bulk conditions. With nucleation and growth occurring in close proximity to the CA catalysts of the system, transport distances are reduced which translates into an improvement in the overall formation rate, as indicated by a lower t_m in our analysis above.

A significant advantage to using whole cell systems for biotransformations is the low cost, as there is no need to purify the enzymes or the peptides for subsequent applications. However there are a few potential limitations of this approach. For example, peptide stability could be problematic in various environmental conditions, especially at high pH. And blocking of the peptides could occur as calcite crystals form near the surface of the cell.

Future work on this technology could include scale-up of the experiments to bench- or pilot-scale reactors. These experiments would provide some insight as to the feasibility of incorporation into an actual process. And, in-depth characterization of the structure of the crystals formed with and without the biocatalysts present would be an interesting next step. This could serve to identify alternate uses for the surface-displayed peptides in terms of manipulating the morphology of the precipitated CaCO3.

5.6. Conclusions

The use of whole cell biocatalysts in carbon mineralization processes is being explored and these cells can be engineered to facilitate several steps in this process. We have previously

demonstrated that periplasmic expression of CA enzymes can enhance CO_2 hydration, and here we show that the concomitant addition of the GPA peptide can also enhance calcite precipitation amounts and rates. By localizing the peptides to the surface of the cells, the peptides are likely operating in a region of high supersaturation leading to increased performance. The whole cells will be attractive new biocatalysts for carbon sequestrion and this work further demonstrates the power of synthetic biology for making improved biocatalytic systems.

5.7. Acknowledgements

The authors would like to thank the US Department of Energy for funding this work through ARPA-e Grant DE-AR0000100.

5.8. Figures and Tables

Figure 5-1 - Schematic of eCPX constructs

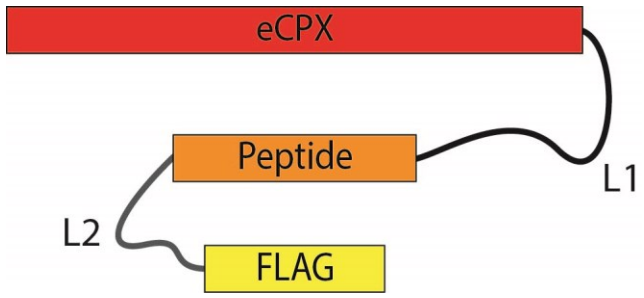

General schematic of eCPX constructs generated. The N-terminus of the eCPX protein was left unaltered, with all fusions made to the C-terminus of the protein. The linker L1 (N-GGQSGQ-C) was used between eCPX and the D20, GPA, and FLK peptides. The L2 linker (N-GGGS-C) was inserted between the peptides and the FLAG tag, which was used to confirm expression of the fusion. For the construct containing only the FLAG tag without a peptide, FLAG was fused to eCPX with the L1 linker and L2 was omitted.

Figure 5-2 - Amount of CaCO3 precipitation w/ and w/o eCPX-peptides

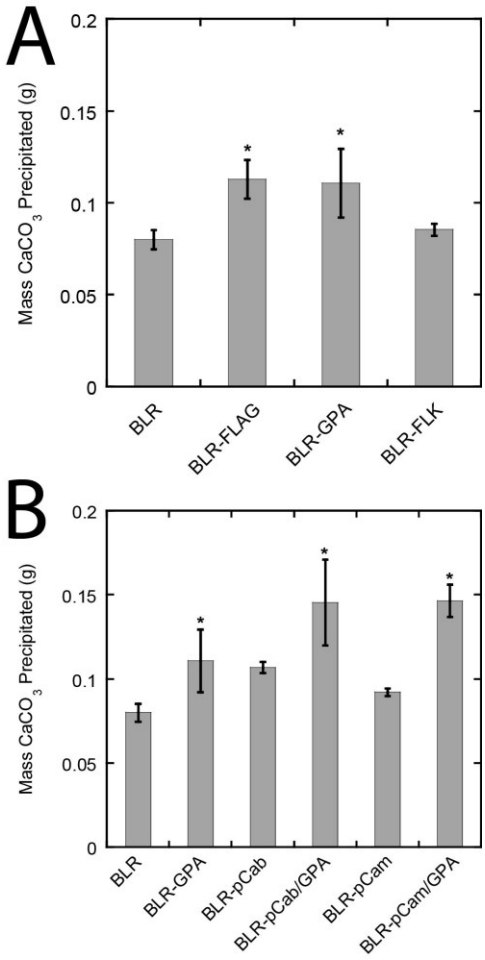

Mass of $CaCO_3$ precipitated in presence of (A) BLR cells with no peptide, FLAG, GPA, or FLK surface-displayed and in the presence of (B) BLR, BLR-pCab, and BLR-pCam cells with and without surface-displayed GPA peptide. All measurements were performed at least in triplicate, and the error bars represent the standard deviations from the mean values.

*Indicates statistically significant difference in precipitation amount from unmarked data sets

Figure 5-3 - Turbidity vs. time example data and fit

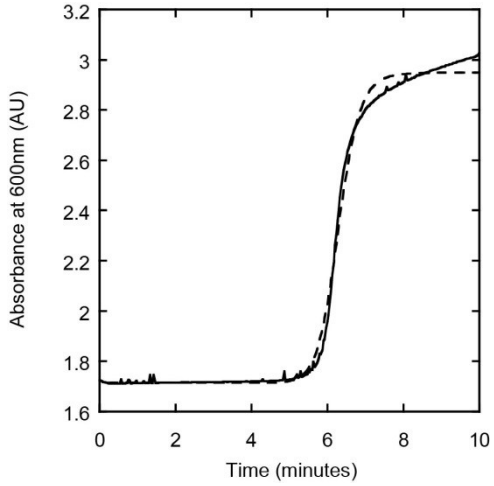

$CaCO_3$ precipitation measured by the absorbance at 600 nm (▬) and the Hill Equation fit to the data (▬ ▬ ▬) against time for one replicate using BLR cells. Similar curves were obtained and fit in the same manner for BLR, BLR-GPA, BLR-pCab, BLR-pCab/GPA, BLR-pCam, and BLR-pCam/GPA cells, as shown in Figure S5-3-Figure S5-8.

Table 5-1 - t_m for various whole-cell biocatalysts evaluated

Whole-Cell Biocatalyst	GPA	t_m (min)
BLR	-	6.3 ± 0.2
BLR	+	6.0 ± 0.3
BLR-pCab	-	5.6 ± 0.3
BLR-pCab	+	4.6 ± 0.2[a]
BLR-pCam	-	5.5 ± 0.4
BLR-pCam	+	2.2 ± 0.1[a]

t_m = Time required to achieve maximum rate of turbidity change
All measurements were performed in triplicate and errors represent the standard deviations from the means
[a]Indicates statistically significant difference from corresponding whole-cell biocatalysts without GPA expression

5.9. Supplementary Information

Table S5-1 - Oligonucleotide sequences for eCPX cloning

Oligonucleotide	Description	Sequence
TP49	eCPX Forward Primer	5'-TCG CAA CTC TCT ACT GTT TCT CCA TAC CCG-3'
TP50	Reverse Ultramer (FLAG) (N-DYKDDDDK-C)	5'-AGT CAG GGC CAC CTT GGC CTT ATT ATT TGT CAT CAT CGT CTT TAT AAT CCT GGC CGC TCT GGC CGC CGC TTG CAG TAC GGC TTT TCT CGG TGT AA-3'
TP57	Reverse Ultramer (D20-FLAG) (N-$(D)_{20}$-C)	5'-AGT CAG GGC CAC CTT GGC CTT ATT ATT TGT CAT CAT CGT CTT TAT AAT CGC TGC CGC CGC CAT CGT CAT CGT CAT CAT CGT CAT CGT CAT CAT CGT CAT CGT CAT CGT CAT CAT CGT CAT CGT CAT CCT GGC CGC TCT GGC CGC CGC TTG CAG TAC GGC TTT TCT CGG TGT AA-3'
TP58	Reverse Ultramer (GPA-FLAG) (N-PEVPEGAFDTAI-C)	5'-AGT CAG GGC CAC CTT GGC CTT ATT ATT TGT CAT CAT CGT CTT TAT AAT CGC TGC CGC CGC CAA TCG CGG TAT CAA ACG CGC CTT CTG GCA CTT CCG GCT GGC CGC TCT GGC CGC CGC TTG CAG TAC GGC TTT TCT CGG TGT AA-3'
TP59	Reverse Ultramer (FLK-FLAG) (N-$(FLK)_4$-C)	5'-AGT CAG GGC CAC CTT GGC CTT ATT ATT TGT CAT CAT CGT CTT TAT AAT CGC TGC CGC CGC CTT TCA GGA ACT TGA GAA ATT TCA GGA ATT TCA GAA ACT GGC CGC TCT GGC CGC CGC TTG CAG TAC GGC TTT TCT CGG TGT AA -3'

TP49 does not contain a recognition site for SfiI. This is because it is upstream of the eCPX gene and the 5' SfiI recognition site in the plasmid. The SfiI recognition sites in TP43, TP57, TP58, and TP59 are underlined.

Figure S5-1 - Flow cytometry confirming expression of peptides

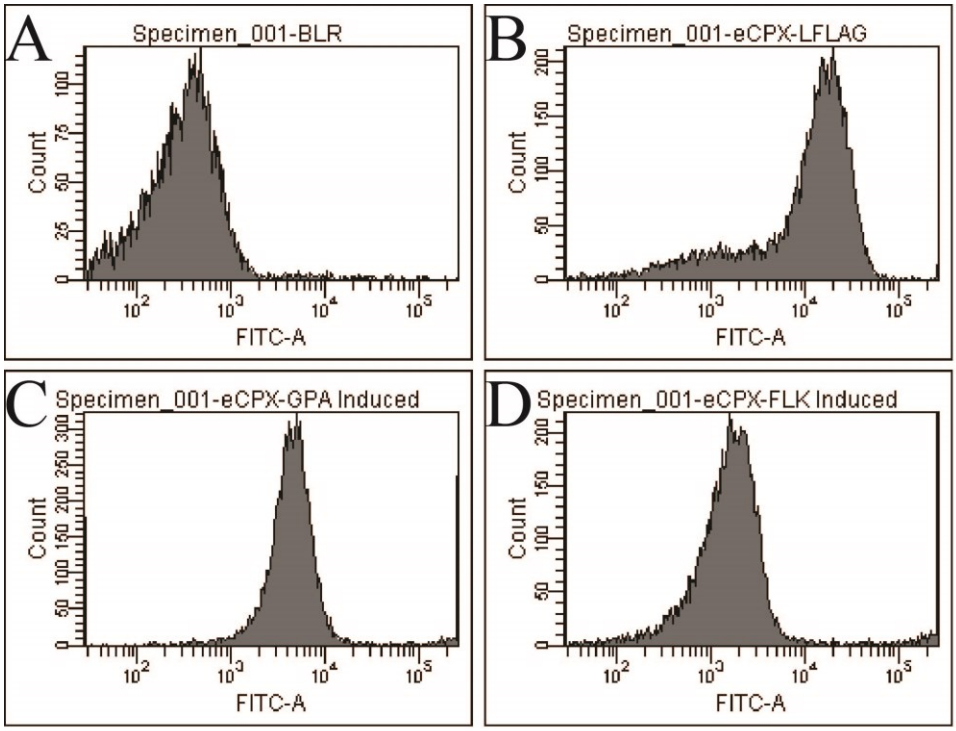

Flow cytometry of cells labeled with anti-FLAG-FITC conjugated monoclonal antibody. After expression, 0.5 mL of the cell culture was centrifuged at maximum speed (13000 rpm) for 1 minute. The pellet was then washed 2 times with 1xPBS by resuspending the cells in the buffer and then pelleting them via centrifugation. The washed pellet was resuspended in 0.5 mL 1xPBS supplemented with 2.5 µL of the antibody and 5 µL of 100xBSA. After incubation at room temperature for 20 minutes with gentle agitation, the cells were washed twice with 1xPBS. The washed pellet was resuspended in 2 mL of 1xPBS and analyzed on a FACSCanto II Flow Cytometer (BD Biosciences, Franklin Lakes, NJ). (A) BLR, (B) BLR-FLAG, (C) BLR-GPA, and (D) BLR-FLK cells labeled with anti-FLAG-FITC antibody.

Figure S5-2 - Flow cytometry confirming GPA expression

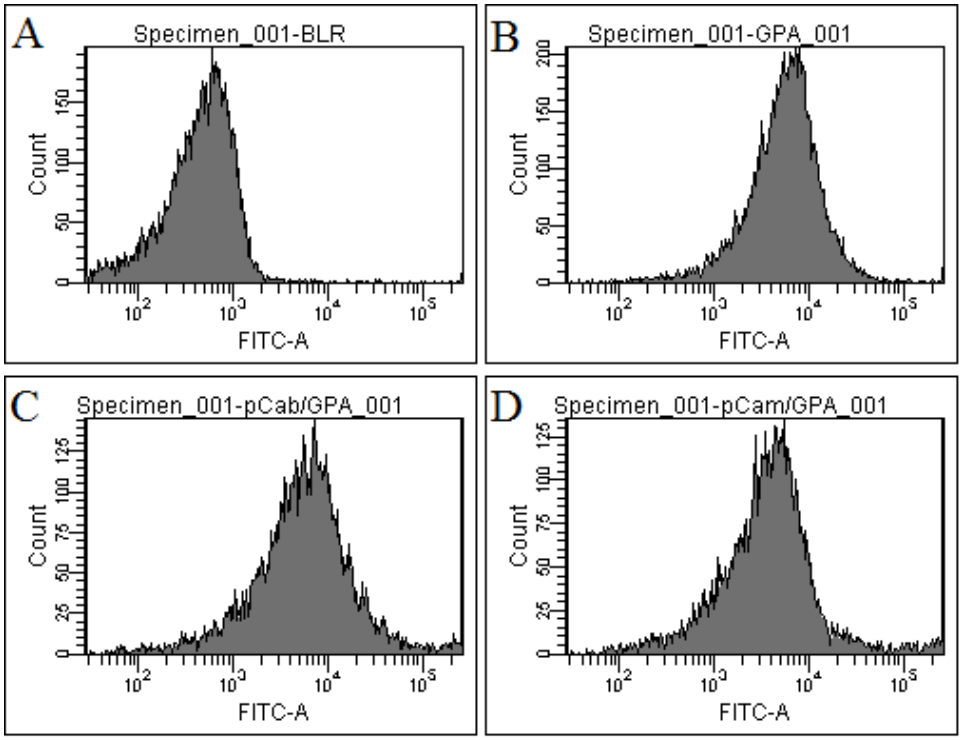

Flow cytometry of (A) BLR, (B) BLR-GPA, (C) BLR-pCab/GPA, and (D) BLR-pCam/GPA cells labeled with anti-FLAG-FITC antibody using the protocol described in Figure S1.

Figure S5-3 - $CaCO_3$ Formation Rate Data for BLR cells

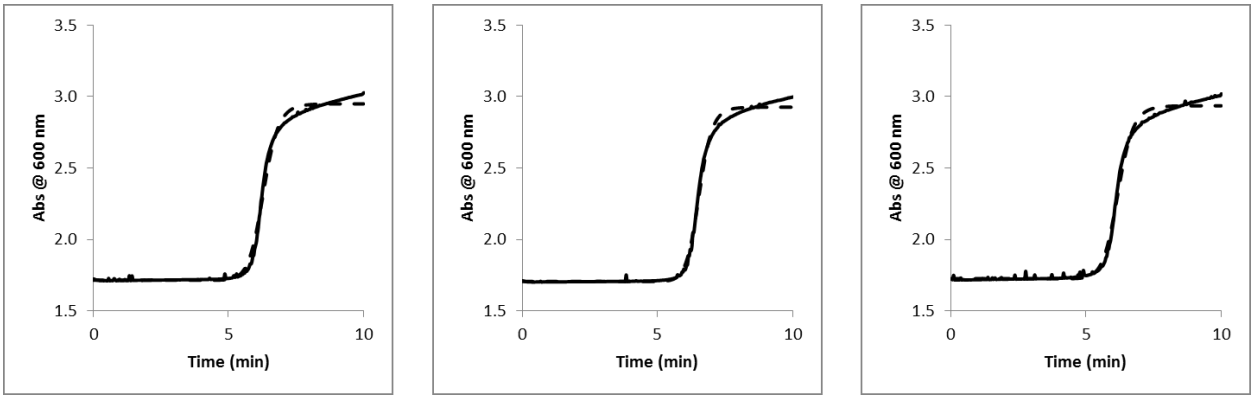

Turbidity (Abs @ 600 nm) against time (solid lines) and Hill fits (dashed lines).

Figure S5-4 - $CaCO_3$ Formation Rate Data for BLR-GPA cells

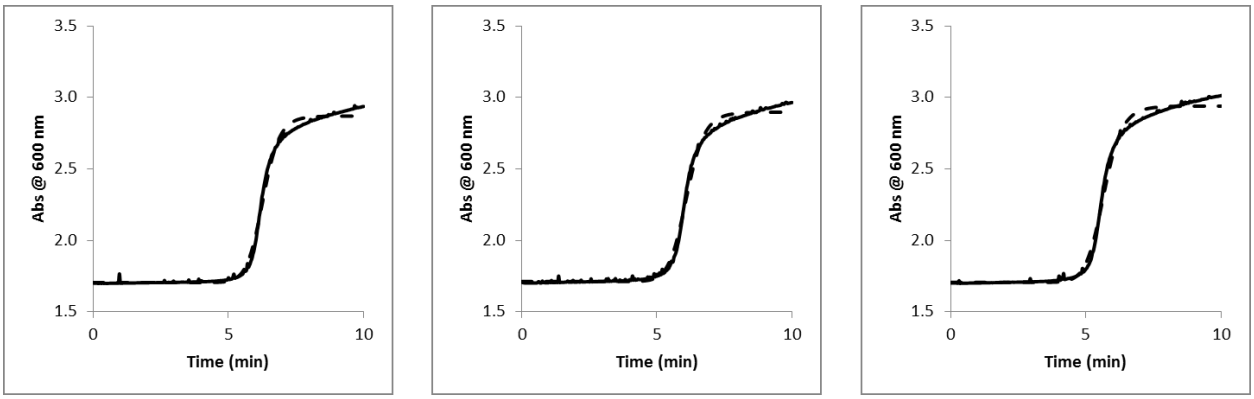

Turbidity (Abs @ 600 nm) against time (solid lines) and Hill fits (dashed lines).

Figure S5-5 - $CaCO_3$ Formation Rate Data for BLR-pCab cells

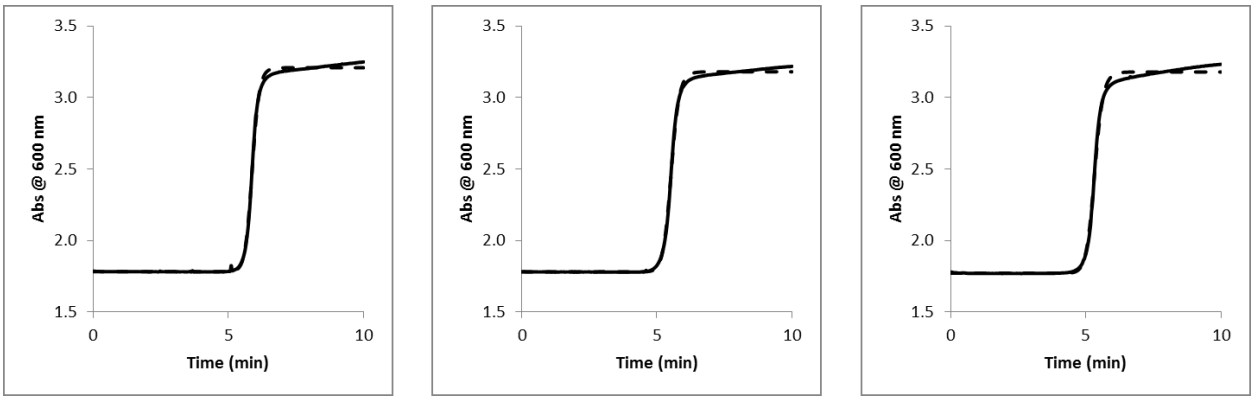

Turbidity (Abs @ 600 nm) against time (solid lines) and Hill fits (dashed lines).

Figure S5-6 - $CaCO_3$ Formation Rate Data for BLR-pCab/GPA cells

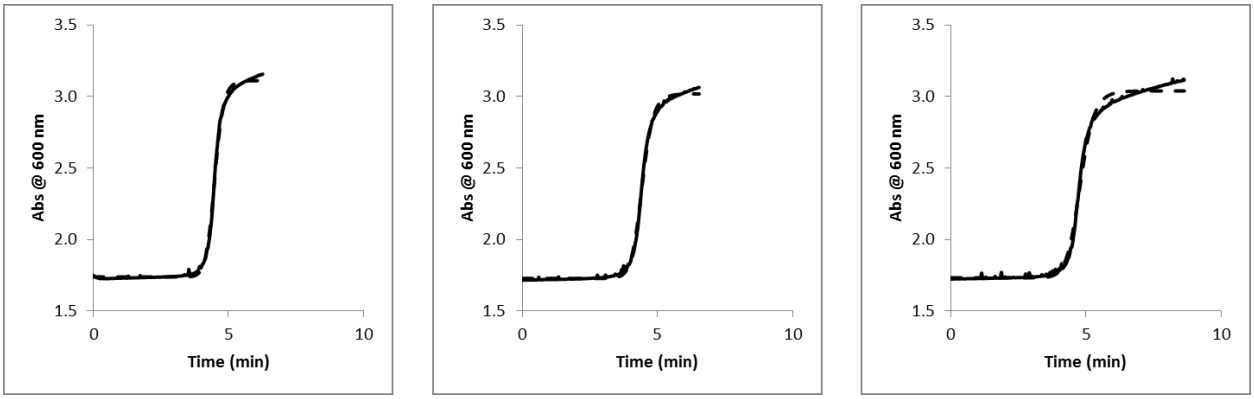

Turbidity (Abs @ 600 nm) against time (solid lines) and Hill fits (dashed lines).

Figure S5-7 - $CaCO_3$ Formation Rate Data for BLR-pCam cells

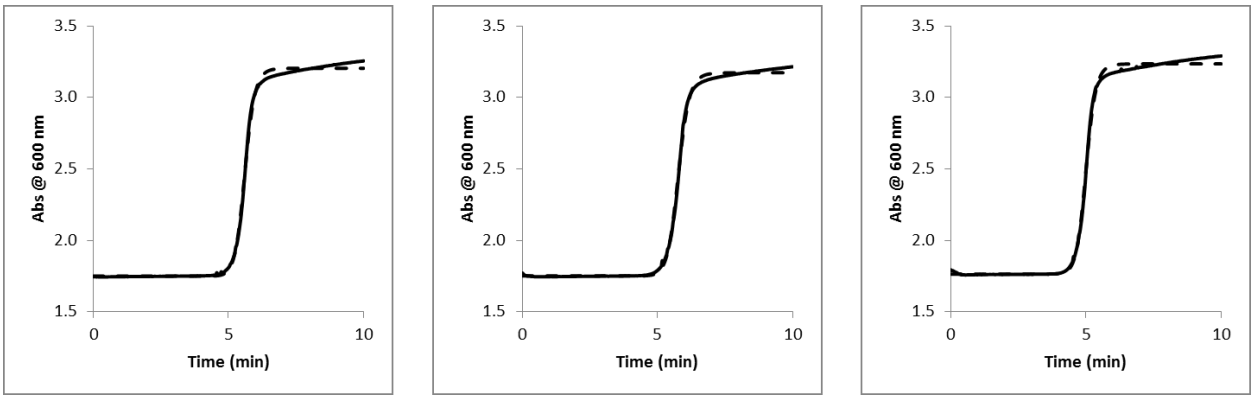

Turbidity (Abs @ 600 nm) against time (solid lines) and Hill fits (dashed lines).

Figure S5-8 - $CaCO_3$ Formation Rate Data for BLR-pCam/GPA cells

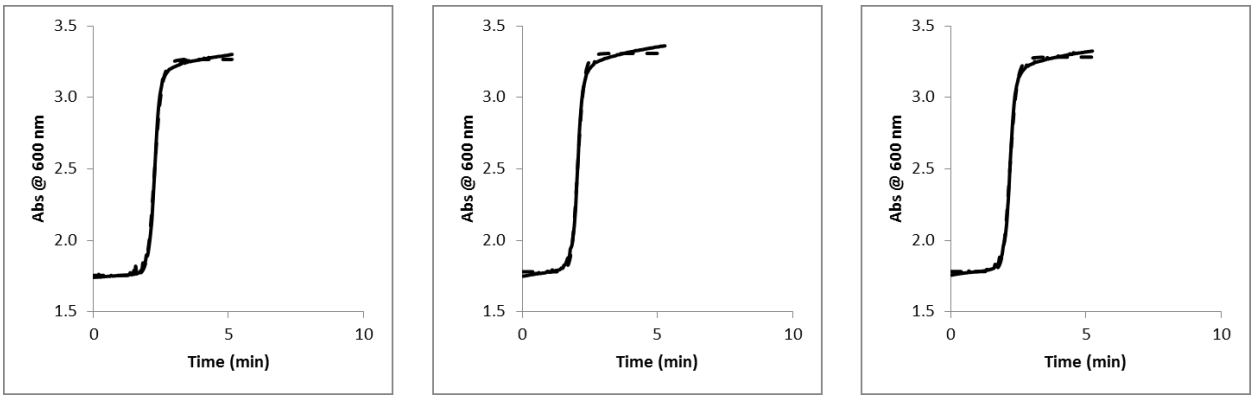

Turbidity (Abs @ 600 nm) against time (solid lines) and Hill fits (dashed lines).

6. Summary and Future Work

6.1. Summary

In this dissertation we have outlined our efforts towards understanding and engineering heterogeneous biocatalysis using two different enzyme immobilization techniques. Heterogeneous biocatalysis provides many advantages over homogeneous biocatalysis including enhanced stability, improved recyclability, and reduced cost. Each of these benefits contributes to the attractiveness of these biocatalysts for both research and industrial applications.

In Chapter 1, we examined the governing principles and current literature behind two enzyme immobilization techniques: adsorption to a solid surface and whole-cell biocatalysis. We began by discussing the link between protein folding and surface adsorption, in that the same forces that contribute to protein folding are also responsible for allowing a protein to adsorb onto a surface. In both cases, the goal is to minimize the Gibbs Free Energy of the system. The current literature in this field has examined adsorption behavior, desorption behavior, the effects of particle curvature, and the effects of engineered thermal stability, among other topics. We felt there was a gap in this body of work, in which naturally-evolved proteins with similar structures but vastly different thermal stabilities were used. As such, we described a system in which AdhD and hAR, two members of the AKR superfamily could be used to explore just that.

Further into Chapter 1, we discussed several techniques by which an enzyme could be immobilized onto or within the host cell in which it was expressed. One of the major advantages to this approach is that protein purification is not required since immobilization is often performed in parallel with expression. Cytosolic expression, periplasmic expression, and surface display were all examined as possibilities, with advantages and disadvantages to each provided.

Due to these comparisons, periplasmic expression was selected as the immobilization modality for this work. The enzyme selected as a model for this work was carbonic anhydrase, a family of Zn^{+2}-binding metalloenzymes capable of catalyzing the reversible hydration of CO_2. From this family, 2 were selected, namely Cab and Cam, for their individual characteristics that could prove beneficial to the generation of an efficient, stable whole-cell biocatalyst.

In Chapter 2, we addressed the gap in current adsorption literature described above. Using AdhD and hAR, we were able to determine how adsorption behavior varies with intrinsic native stability, as opposed to engineered stability. From this work, it was determined that even a protein with extremely high thermal stability (AdhD) is susceptible to significant surface-induced structural rearrangement, regardless of surface coverage. This surprisingly coincided with hAR's adsorption behavior, so much so that both proteins exhibited similar structures in their respective adsorbed states. Conversely, their desorption behaviors did vary. AdhD, while never returning to native form, regained the same amount of structure and activity upon desorption in a surface coverage-independent manner. The properties of desorbed hAR, however, were dependent on surface coverage such that proteins desorbed from lower coverages refolded to a lesser degree and thus exhibited slower kinetics relative to native enzyme. From these findings we concluded there is less correlation between thermostability and adsorption behavior than previously thought.

As an alternative to adsorption, whole-cell biocatalysis was explored, beginning with Chapter 3.1. Cab and Cam were periplasmically expressed using the gIII and pelB periplasmic leader peptides. The pelB system showed higher expression levels and whole-cell kinetics for both enzymes. There was no difference in activity retention after 24 hours between the two peptides. There was also no observed difference in the amount of carbonate precipitated in the presence of cells

harboring CA. Finally, the whole-cell biocatalysts containing Cab were more stable than purified Cab, retaining almost 100% of their native activity at 95^{o}C. A similar result was seen with BLR-gCam, but BLR-pCam did not follow this trend, losing about 35% of its native activity at 95^{o}C. We hypothesized that in cells expressing pCam, there was some amount of membrane perturbation that increased the overall reaction rate (BLR-pCam exhibited the highest activity of the 4 whole-cell biocatalysts), but also reduced the stabilizing effects of immobilization. These experiments showed that we were able to successfully create and characterize heterogeneous biocatalysts in the form of whole-cells. However, for complete characterization, there was still one parameter missing: operational stability.

In current literature, there are several methods by which to measure the operational stability of a biocatalyst. However, CA-based biocatalysts are much more difficult to characterize by these methods so we took it upon ourselves to develop a new method for this purpose. In Chapter 3.2, we presented a repeated-batch method that employed automatic switching between the forward and reverse reactions for CA-based biocatalysts. In this way, the activity of the biocatalysts was tracked over time and used to determine the operational stability. This data was used to calculate the half-lives of both homogeneous and heterogeneous biocatalysts with CA activity. Cab was found to have the longest half-life of the purified enzymes, and all 4 of the whole-cell biocatalysts evaluated were stable for far longer than the limit of stable operation for the method, further supporting the theory of enzyme stabilization upon immobilization.

Moving forward from simply characterizing the whole-cell biocatalysts, we sought to introduce modifications to the cells to improve their kinetic and functional activities. In Chapter 4, the envelope protein from SARS coronavirus was recombinantly expressed in the biocatalysts. This protein (SCVE) was previously shown to permeabilize the outer membranes of *E. coli* cells.

Upon expression, SCVE increased outer membrane permeability to a small molecule (NPN) and improved the overall reaction rate of CO_2 hydration in the presence of the biocatalysts. After characterization, the η, ϕ, D_e, and P for both the unmodified and modified biocatalysts were calculated and compared. This analysis showed an approximate doubling in effectiveness factor, and halving of the Thiele modulus.

The second modification to the whole-cell biocatalysts was to express Ca^{+2}-binding peptides on the outer surface of the cells using the eCPX system. This work was described in Chapter 5. The eCPX protein is a modified version of the OmpX transmembrane protein such that its termini are exposed to the extracellular space. Several peptides were fused to the exposed C-terminus and evaluated for their ability to precipitate $CaCO_3$. We found that surface-displayed GPA peptide in conjunction with periplasmic CA generated the most precipitate, and also significantly enhanced the calcite precipitation rate in the presence of our whole-cell biocatalysts.

6.2. Future Work

Although we were able to accomplish a considerable amount surrounding heterogeneous biocatalysts, there is always the opportunity to expand upon the work completed. In this final section of this dissertation, we present some areas for further exploration in order to gain further understanding of immobilization, or to engineer even better biocatalysts.

Area 1: Combined effects of thermal stability and surface properties on adsorption behavior

In order to supplement the work performed using AdhD and hAR, we believe that performing these same experiments on more substrates would provide additional information as to the full impact of intrinsic thermal stability on adsorption behavior. As discussed in Chapter 1, groups

have explored the effects of surface curvature on the structural rearrangement of adsorbed protein molecules. However, perhaps the impact of curvature are not as pronounced for proteins with higher native thermostability. Also, determining the effects of surfaces with varying charges or hydrophobicities would further characterize the adsorption behaviors of proteins with different thermal stabilities.

Area 2: Combining whole-cell modifications to improve overall functionality

In Chapters 4 and 5, we examined outer membrane permeabilization and outer membrane functionalization, respectively. These modifications were shown to improve the kinetic and functional activities when used individually. Perhaps combining these two systems into one whole-cell biocatalyst would provide an additional benefit that is greater than the sum of the two parts individually. Given the changes observed in the presence of each modification, it is not unreasonable to assume that improving the kinetic activity and precipitation capabilities of a whole-cell biocatalyst would yield the greatest improvement over the unmodified biocatalyst.

Area 3: Engineering whole-cells as analogs for metabalons

In biochemical pathways, metabolons are complexes of enzymes in which each enzyme is responsible for a specific segment of the pathway [209-211]. These complexes can involve any number of enzymes, depending on the complexity of the pathway. Most commonly, these metabolons are formed by fusing the various proteins together [212, 213]. However, using what we have learned about whole-cell biocatalysis, we believe that a cell could be used as a scaffold for metabolon formation. By co-expressing multiple proteins in a single cell, we could introduce novel function to the cell to bring a metabolic pathway to completion. Further, the cell provides the unique opportunity of being able to compartmentalize the enzymes such that we could have

enzymes in the cytosol, periplasm, and exposed to the extracellular matrix to drive the reaction from within the cell towards secretion, or vice versa. To catalyze a biochemical reaction, this scheme would allow us to take advantage of the concept of substrate channeling [214], in which the intermediates of a reaction are shuttled from one enzyme to another along the conversion pathway.

Creating a metabolon within the cell also would allow us to harness the differences in various promoters to our advantage. By placing more active enzymes under weaker promoters and less active enzymes under stronger promoters, the disparity in kinetics could be normalized so that the reaction is as close to equilibrium as possible. Using these principles and techniques, we could engineer cells to act as metabolons for a wide variety of reactions and pathways.

7. References

[1] A. Illanes, Enzyme biocatalysis: principles and applications, Springer Verlag, 2008.

[2] D.J. Pollard, J.M. Woodley, Biocatalysis for pharmaceutical intermediates: the future is now, TRENDS in Biotechnology, 25 (2007) 66-73.

[3] R.A. Gross, A. Kumar, B. Kalra, Polymer synthesis by in vitro enzyme catalysis, Chemical Reviews, 101 (2001) 2097-2124.

[4] I. Chibata, T. Tosa, T. Sato, Biocatalysis: immobilized cells and enzymes, Journal of molecular catalysis, 37 (1986) 1-24.

[5] F. Shu, G. Wilson, Rotating ring-disk enzyme electrode for surface catalysis studies, Analytical Chemistry, 48 (1976) 1679-1686.

[6] C. Mateo, J.M. Palomo, G. Fernandez-Lorente, J.M. Guisan, R. Fernandez-Lafuente, Improvement of enzyme activity, stability and selectivity via immobilization techniques, Enzyme and Microbial Technology, 40 (2007) 1451-1463.

[7] L. Gianfreda, M.R. Scarfi, Enzyme stabilization: state of the art, Molecular and cellular biochemistry, 100 (1991) 97-128.

[8] W. Norde, Adsorption of proteins from solution at the solid-liquid interface, Advances in Colloid and Interface Science, 25 (1986) 267-340.

[9] W. Norde, J.P. Favier, Structure of adsorbed and desorbed proteins, Colloids and Surfaces, 64 (1992) 87-93.

[10] J. Andrade, V. Hlady, Protein adsorption and materials biocompatibility: a tutorial review and suggested hypotheses, Biopolymers/Non-Exclusion HPLC, (1986) 1-63.

[11] T. Zoungrana, G.H. Findenegg, W. Norde, Structure, stability, and activity of adsorbed enzymes, Journal of colloid and interface science, 190 (1997) 437-448.

[12] A.A. Vertegel, R.W. Siegel, J.S. Dordick, Silica nanoparticle size influences the structure and enzymatic activity of adsorbed lysozyme, Langmuir, 20 (2004) 6800-6807.

[13] M. Lundqvist, I. Sethson, B.H. Jonsson, Protein adsorption onto silica nanoparticles: conformational changes depend on the particles' curvature and the protein stability, Langmuir, 20 (2004) 10639-10647.

[14] J.C. Fröberg, T. Arnebrant, J. McGuire, P.M. Claesson, Effect of structural stability on the characteristics of adsorbed layers of T4 lysozyme, Langmuir, 14 (1998) 456-462.

[15] M.H. Tian, W.K. Lee, M.K. Bothwell, J. McGuire, Structural stability effects on adsorption of bacteriophage T4 lysozyme to colloidal silica, Journal of Colloid and Interface Science, 200 (1998) 146-154.

[16] V. Hlady, J. Buijs, Protein adsorption on solid surfaces, Current opinion in biotechnology, 7 (1996) 72-77.

[17] F. Felsovalyi, P. Maniagalli, C. Bureau, S. Kumar, S. Banta, The Reversibility of Lysozyme on Silica, Langmuir, 27 (2011) 11873-11882.

[18] C.M. Dobson, Protein folding and misfolding, Nature, 426 (2003) 884-890.

[19] C.K. Bower, S. Sananikone, M.K. Bothwell, J. McGuire, Activity losses among T4 lysozyme charge variants after adsorption to colloidal silica, Biotechnology and Bioengineering, 64 (1999) 373-376.

[20] B.L. Steadman, K.C. Thompson, C.R. Middaugh, K. Matsuno, S. Vrona, E.Q. Lawson, R.V. Lewis, The effects of surface adsorption on the thermal stability of proteins, Biotechnology and bioengineering, 40 (1992) 8-15.

[21] B. Singla, V. Krisdhasima, J. McGuire, Adsorption kinetics of wild type and two synthetic stability mutants of T4 phage lysozyme at silanized silica surfaces, Journal of Colloid and Interface Science, 182 (1996) 292-296.

[22] R. Machielsen, A.R. Uria, S.W.M. Kengen, J. van der Oost, Production and characterization of a thermostable alcohol dehydrogenase that belongs to the aldo-keto reductase superfamily, Applied and Environmental Microbiology, 72 (2006) 233-238.

[23] K.M. Bohren, J.L. Page, R. Shankar, S.P. Henry, K.H. Gabbay, Expression of human aldose and aldehyde reductases - Site-directed mutagenesis of a critical lysine-262, J Biol Chem, 266 (1991) 24031-24037.

[24] J.M. Jez, M.J. Bennett, B.P. Schlegel, M. Lewis, T.M. Penning, Comparative anatomy of the aldo-keto reductase superfamily., Biochemical Journal, 326 (1997) 625-636.

[25] D. Hyndman, D.R. Bauman, V.V. Heredia, T.M. Penning, The aldo-keto reductase superfamily homepage, Chemico-biological interactions, 143 (2003) 621-631.

[26] T. Matsumoto, S. Takahashi, M. Kaieda, M. Ueda, A. Tanaka, H. Fukuda, A. Kondo, Yeast whole-cell biocatalyst constructed by intracellular overproduction of Rhizopus oryzae lipase is applicable to biodiesel fuel production, Applied microbiology and biotechnology, 57 (2001) 515-520.

[27] K. Goldberg, K. Schroer, S. Lütz, A. Liese, Biocatalytic ketone reduction—a powerful tool for the production of chiral alcohols—part I: processes with isolated enzymes, Applied microbiology and biotechnology, 76 (2007) 237-248.

[28] B. Wilms, A. Wiese, C. Syldatk, R. Mattes, J. Altenbuchner, Development of an Escherichia coli whole cell biocatalyst for the production of-amino acids, Journal of biotechnology, 86 (2001) 19-30.

[29] M.B. Martinez, M.C. Flickinger, G.L. Nelsestuen, Steady-state enzyme kinetics in the Escherichia coli periplasm: a model of a whole cell biocatalyst, Journal of biotechnology, 71 (1999) 59-66.

[30] L.H. Fan, N. Liu, M.R. Yu, S.T. Yang, H.L. Chen, Cell surface display of carbonic anhydrase on Escherichia coli using ice nucleation protein for CO2 sequestration, Biotechnology and Bioengineering, (2011).

[31] K. Ban, M. Kaieda, T. Matsumoto, A. Kondo, H. Fukuda, Whole cell biocatalyst for biodiesel fuel production utilizing Rhizopus oryzae cells immobilized within biomass support particles, Biochemical Engineering Journal, 8 (2001) 39-43.

[32] P. Cornelis, Expressing genes in different< i> Escherichia coli</i> compartments, Current opinion in biotechnology, 11 (2000) 450-454.

[33] S. Ståhl, M. Uhlén, Bacterial surface display: trends and progress, Trends in biotechnology, 15 (1997) 185-192.

[34] S.Y. Lee, J.H. Choi, Z. Xu, Microbial cell-surface display, TRENDS in Biotechnology, 21 (2003) 45-52.

[35] F. Baneyx, Recombinant protein expression in< i> Escherichia coli</i>, Current opinion in biotechnology, 10 (1999) 411-421.

[36] D. Missiakas, S. Raina, Protein folding in the bacterial periplasm, Journal of bacteriology, 179 (1997) 2465.

[37] L. Graham, T. Beveridge, N. Nanninga, Periplasmic space and the concept of the periplasm, Trends in biochemical sciences, 16 (1991) 328-329.

[38] R.R. Chen, Permeability issues in whole-cell bioprocesses and cellular membrane engineering, Applied microbiology and biotechnology, 74 (2007) 730-738.

[39] S. Lindskog, Structure and mechanism of carbonic anhydrase, Pharmacology & Therapeutics, 74 (1997) 1-20.

[40] D. Keilin, T. Mann, Carbonic anhydrase. Purification and nature of the enzyme, Biochemical Journal, 34 (1940) 1163.

[41] D.N. Silverman, S. Lindskog, The Catalytic Mechanism of Carbonic-Anhydrase - Implications of a Rate-Limiting Protolysis of Water, Accounts of Chemical Research, 21 (1988) 30-36.

[42] K.S. Smith, J.G. Ferry, Prokaryotic carbonic anhydrases, FEMS microbiology reviews, 24 (2000) 335-366.

[43] S.J. Dodgson, R.P. Shank, B.E. Maryanoff, Topiramate as an inhibitor of carbonic anhydrase isoenzymes, Epilepsia, 41 (2000) 35-39.

[44] K.S. Smith, N.J. Cosper, C. Stalhandske, R.A. Scott, J.G. Ferry, Structural and kinetic characterization of an archaeal beta-class carbonic anhydrase, Journal of Bacteriology, 182 (2000) 6605-6613.

[45] K.S. Smith, J.G. Ferry, A plant-type (β-class) carbonic anhydrase in the thermophilic methanoarchaeon Methanobacterium thermoautotrophicum, Journal of bacteriology, 181 (1999) 6247-6253.

[46] B.E. Alber, C.M. Colangelo, J. Dong, C.M.V. Stalhandske, T.T. Baird, C.K. Tu, C.A. Fierke, D.N. Silverman, R.A. Scott, J.G. Ferry, Kinetic and spectroscopic characterization of the gamma-carbonic anhydrase from the methanoarchaeon Methanosarcina thermophila, Biochemistry, 38 (1999) 13119-13128.

[47] C.K. Savile, J.J. Lalonde, Biotechnology for the acceleration of carbon dioxide capture and sequestration, Current opinion in biotechnology, (2011).

[48] M.R. Badger, G.D. Price, The role of carbonic anhydrase in photosynthesis, Annual review of plant biology, 45 (1994) 369-392.

[49] A. Kumar, S. Ergas, X. Yuan, A. Sahu, Q. Zhang, J. Dewulf, F.X. Malcata, H. Van Langenhove, Enhanced CO2 fixation and biofuel production via microalgae: recent developments and future directions, Trends in biotechnology, 28 (2010) 371-380.

[50] C. Cammaroto, L. Diliberto, M. Ferralis, R. Manca, A. Sanna, M. Giordano, Use of carbonic anhydrase in electrochemical biosensors for dissolved CO2, Sensors and Actuators B: Chemical, 48 (1998) 439-447.

[51] B.E. Alber, J.G. Ferry, A carbonic anhydrase from the archaeon Methanosarcina thermophila, Proceedings of the National Academy of Sciences, 91 (1994) 6909-6913.

[52] K. Kato, S. Sano, Y. Ikada, Protein adsorption onto ionic surfaces, Colloids and Surfaces B: Biointerfaces, 4 (1995) 221-230.

[53] J. McGuire, M.C. Wahlgren, T. Arnebrant, The Influence of Net Charge and Charge Location on the Adsorption and Dodecyltrimethylammonium Bromide-Mediated Elutability of Bacteriophage-T4 Lysozyme at Silica Surfaces, Journal of Colloid and Interface Science, 170 (1995) 193-202.

[54] M. Malmsten, N. Burns, A. Veide, Electrostatic and hydrophobic effects of oligopeptide insertions on protein adsorption, Journal of Colloid and Interface Science, 204 (1998) 104-111.

[55] P. Billsten, M. Wahlgren, T. Arnebrant, J. McGuire, H. Elwing, Structural changes of T4 lysozyme upon adsorption to silica nanoparticles measured by circular dichroism, Journal of Colloid and Interface Science, 175 (1995) 77-82.

[56] C. Haynes, N. W, Globular proteins at sold/liquid interfaces, Colloids and Surfaces B: Biointerfaces, 2 (1994) 517-566.

[57] T. Arai, W. Norde, The behavior of some model proteins at solid liquid interfaces. 1. Adsorption from single protein solutions, Colloids and Surfaces, 51 (1990) 1-15.

[58] J.D. Andrade, V. Hlady, Plasma-Protein Adsorption - the Big 12, Ann NY Ac Sci, 516 (1987) 158-172.

[59] M.C. Wahlgren, M.A. Paulsson, T. Arnebrant, Adsorption of globular model proteins to silica and methylated silica surfaces and their elutability by dodecyltrimethylammonium bromide, Colloids and Surfaces a-Physicochemical and Engineering Aspects, 70 (1993) 139-149.

[60] M. Karlsson, J. Ekeroth, H. Elwing, U. Carlsson, Reduction of irreversible protein adsorption on solid surfaces by protein engineering for increased stability, Journal of Biological Chemistry, 280 (2005) 25558-25558.

[61] S.Q. Xu, S. Damodaran, Comparative adsorption of native and denatured egg-white, human, and T(4)-phage lysozymes at the air-water interface, Journal of Colloid and Interface Science, 159 (1993) 124-133.

[62] J. McGuire, M.C. Wahlgren, T. Arnebrant, Structural Stability Effects on the Adsorption and Dodecyltrimethylammonium Bromide-Mediated Elutability of Bacteriophage-T4 Lysozyme at Silica Surfaces, Journal of Colloid and Interface Science, 170 (1995) 182-192.

[63] J.S. Apte, L.J. Gamble, D.G. Castner, C.T. Campbell, Kinetics of leucine-lysine peptide adsorption and desorption at -CH3 and -COOH terminated alkylthiolate monolayers, Biointerphases, 5 (2010) 97-104.

[64] T. Weidner, N.T. Samuel, K. McCrea, L.J. Gamble, R.S. Ward, D.G. Castner, Assembly and structure of alpha-helical peptide films on hydrophobic fluorocarbon surfaces, Biointerphases, 5 (2010) 9-16.

[65] S.L. Burkett, M.J. Read, Adsorption-induced conformational changes of alpha-helical peptides, Langmuir, 17 (2001) 5059-5065.

[66] D. Elbaum, J. Harrington, E.F. Roth, R.L. Nagel, Surface-activity of hemoglobin-S and other human hemoglobin variants, Biochimica Et Biophysica Acta, 427 (1976) 57-69.

[67] A. Kato, K. Yutani, Correlation of surface-properties with conformational stabilties of wild-type and 6 mutant tryptophan synthase alpha-subunits substituted in the same position, Protein Eng., 2 (1988) 153-156.

[68] E. Campbell, I.R. Wheeldon, S. Banta, Broadening the Cofactor Specificity of a Thermostable Alcohol Dehydrogenase Using Rational Protein Design Introduces Novel Kinetic Transient Behavior, Biotechnology and Bioengineering, 107 (2010) 763-774.

[69] C.E. Giacomelli, W. Norde, The adsorption-desorption cycle. Reversibility of the BSA-silica system, Journal of Colloid and Interface Science, 233 (2001) 234-240.

[70] A. Kondo, F. Murakami, M. Kawagoe, K. Higashitani, Kinetic and Circular-Dichroism Studies of Enzymes Adsorbed on Ultrafine Silica Particles, Applied Microbiology and Biotechnology, 39 (1993) 726-731.

[71] N. Sreerama, Estimation of protein secondary structure from circular dichroism spectra: comparison of CONTIN, SELCON, and CDSSTR methods with an expanded reference set, Analytical Biochemistry, 287 (2000).

[72] J.W. Evans, Random and cooperative sequential adsorption, Rev. Mod. Phys., 65 (1993) 1281-1329.

[73] J.S. Bee, D. Chiu, S. Sawicki, J.L. Stevenson, K. Chatterjee, E. Freund, J.F. Carpenter, T.W. Randolph, Monoclonal antibody interactions with micro- and nanoparticles: adsorption, aggregation, and accelerated stress studies, J Pharm Sci, 98 (2009) 3218-3238.

[74] S.T. Tzannis, W.J.M. Hrushesky, P.A. Wood, T.M. Przybycien, Adsorption of a Formulated Protein on a Drug Delivery Device Surface, Journal of Colloid and Interface Science, 189 (1997) 216-228.

[75] M.C. Manning, D.K. Chou, B.M. Murphy, R.W. Payne, D.S. Katayama, Stability of protein pharmaceuticals: an update, Pharmaceutical Research, 27 (2010) 544-575.

[76] E.Y. Chi, S. Krishnan, T.W. Randolph, J.F. Carpenter, Physical stability of proteins in aqueous solution: mechanism and driving forces in nonnative protein aggregation, Pharmaceutical Research, 20 (2003) 1325-1336.

[77] S.M. Kelly, N.C. Price, The application of circular dichroism to studies of protein folding and unfolding, Biochimica et Biophysica Acta, 1338 (1997) 161-185.

[78] S.M. Kelly, N.C. Price, Circular dichroism to study protein interactions, Curr Protoc Protein Sci, Chapter 20 (2006) Unit 20 10.

[79] C.P.M. van Mierlo, E. Steensma, Protein folding and stability investigated by fluorescence, circular dichroism (CD), and nuclear magnetic resonance (NMR) spectroscopy: the flavodoxin story, Journal of Biotechnology, 79 (2000) 281-298.

[80] K. Rezwan, L. Meier, L. Gauckler, Lysozyme and bovine serum albumin adsorption on uncoated silica and A1OOH coated silica. , Biomaterials, 26 (2005).

[81] W. Norde, F. MacRitchie, G. Nowicka, J. Lyklema, Protein adsorption at solid-liquid interfaces: reversibility and conformation aspects, Journal of Colloid and Interface Science, 112 (1986) 447-456.

[82] D. Pellenc, O. Gallet, H. Berry, Adsorption-induced conformational changes in protein diffusion-aggregation surface assemblies, Phys Rev E Stat Nonlin Soft Matter Phys, 72 (2005) 051904.

[83] P. Bagchi, S.M. Birnbaum, Effect of pH on the adsorption of immunoglobulin G on anionic poly(vinyltoluene) model latex particles, Journal of Colloid and Interface Science, 83 (1981) 460-478.

[84] R.D. Tilton, A.P. Gast, C.R. Robertson, Surface diffusion of interacting proteins - Effect of concentration on the lateral mobility of adsorbed bovine serum-albumin Biophysical Journal, 58 (1990) 1321-1326.

[85] P. Billsten, U. Carlsson, B.H. Jonsson, G. Olofsson, F. Hook, H. Elwing, Conformation of human carbonic anhydrase II variants adsorbed to silica nanoparticles, Langmuir, 15 (1999) 6395-6399.

[86] A. Sethuraman, G. Vedantham, T. Imoto, T. Przybycien, G. Belfort, Protein unfolding at interfaces: slow dynamics of alpha-helix to beta-sheet transition, Proteins, 56 (2004) 669-678.

[87] J. Buijs, V. Hlady, Adsorption kinetics, conformation, and mobility of the growth hormone and lysozyme on solid surfaces, studied with TIRF, Journal of Colloid and Interface Science, 190 (1997) 171-181.

[88] T.A. Knotts, N. Rathore, J.J. de Pablo, Structure and stability of a model three-helix-bundle protein on tailored surfaces, Proteins-Structure Function and Bioinformatics, 61 (2005) 385-397.

[89] K. Arnold, L. Bordoli, J. Kopp, T. Schwede, The SWISS-MODEL workspace: a web-based environment for protein structure homology modelling, Bioinformatics, 22 (2006) 195-201.

[90] F. Kiefer, K. Arnold, M. Künzli, L. Bordoli, T. Schwede, The SWISS-MODEL Repository and associated resources, Nucleic acids research, 37 (2009) D387-D392.

[91] M. Peitsch, Protein modeling by E-mail, Bio/technology, 13 (1995) 658-660.

[92] D. Vander Jagt, B. Robinson, K. Taylor, L. Hunsaker, Reduction of trioses by NADPH-dependent aldo-keto reductases. Aldose reductase, methylglyoxal, and diabetic complications, Journal of Biological Chemistry, 267 (1992) 4364-4369.

[93] B.H. Gibbons, J.T. Edsall, Rate of hydration of carbon dioxide and dehydration of carbonic acid at 25, Journal of Biological Chemistry, 238 (1963) 3502-3507.

[94] R.P. Henry, Multiple roles of carbonic anhydrase in cellular transport and metabolism, Annual review of physiology, 58 (1996) 523-538.

[95] C. Merlin, M. Masters, S. McAteer, A. Coulson, Why is carbonic anhydrase essential to Escherichia coli?, Journal of Bacteriology, 185 (2003) 6415-6424.

[96] K.S. Smith, C. Jakubzick, T.S. Whittam, J.G. Ferry, Carbonic anhydrase is an ancient enzyme widespread in prokaryotes, Proceedings of the National Academy of Sciences of the United States of America, 96 (1999) 15184-15189.

[97] B.C. Tripp, K. Smith, J.G. Ferry, Carbonic anhydrase: new insights for an ancient enzyme, Journal of Biological Chemistry, 276 (2001) 48615.

[98] R.B.Y. Lee, J.A.C. Smith, R.E.M. Rickaby, Cloning, expression and characterization of the δ-carbonic anhydrase of Thalassiosira Weissflogii (Bacillariophyceae), Journal of Phycology, (2012) n/a-n/a.

[99] M.R. Sawaya, G.C. Cannon, S. Heinhorst, S. Tanaka, E.B. Williams, T.O. Yeates, C.A. Kerfeld, The structure of β-carbonic anhydrase from the carboxysomal shell reveals a distinct subclass with one active site for the price of two, Journal of Biological Chemistry, 281 (2006) 7546-7555.

[100] Y. Xu, L. Feng, P.D. Jeffrey, Y. Shi, F.M.M. Morel, Structure and metal exchange in the cadmium carbonic anhydrase of marine diatoms, Nature, 452 (2008) 56-61.

[101] R.G. Khalifah, Carbon Dioxide Hydration Activity of Carbonic Anhydrase .1. Stop-Flow Kinetic Studies on Native Human Isoenzyme-B and Isoenzyme-C, Journal of Biological Chemistry, 246 (1971) 2561-&.

[102] R.G. Khalifah, Carbon-Dioxide Hydration Activity of Carbonic-Anhydrase - Paradoxical Consequences of Unusually Rapid Catalysis, Proceedings of the National Academy of Sciences of the United States of America, 70 (1973) 1986-1989.

[103] R.G. Khalifah, J.T. Edsall, Carbon-Dioxide Hydration Activity of Carbonic-Anhydrase .2. Kinetics of Alkylated Anhydrases B and C from Humans, Proceedings of the National Academy of Sciences of the United States of America, 69 (1972) 172-&.

[104] S. Lindskog, The Catalytic Mechanism of Carbonic-Anhydrase, Inorganica Chimica Acta-Bioinorganic Chemistry, 79 (1983) 36-37.

[105] Y. Pocker, D.W. Bjorkquist, Stopped-Flow Studies of Carbon-Dioxide Hydration and Bicarbonate Dehydration in H2o and D2o - Acid-Base and Metal-Ion Catalysis, Journal of the American Chemical Society, 99 (1977) 6537-6543.

[106] X. Zhang, R. van Eldik, T. Koike, E. Kimura, Kinetics and mechanism of the hydration of carbon dioxide and dehydration of bicarbonate catalyzed by a zinc (II) complex of 1, 5, 9-triazacyclododecane as a model for carbonic anhydrase, Inorganic Chemistry, 32 (1993) 5749-5755.

[107] J.V. Moroney, H.D. Husic, N. Tolbert, Effect of carbonic anhydrase inhibitors on inorganic carbon accumulation by Chlamydomonas reinhardtii, Plant physiology, 79 (1985) 177.

[108] C.T. Supuran, A. Scozzafava, Carbonic anhydrase inhibitors and their therapeutic potential, Expert Opinion on Therapeutic Patents, 10 (2000) 575-600.

[109] C.T. Supuran, A. Scozzafava, A. Casini, Carbonic anhydrase inhibitors, Medicinal research reviews, 23 (2003) 146-189.

[110] J.J. Baldwin, G.S. Ponticello, P.S. Anderson, M.E. Christy, M.A. Murcko, W.C. Randall, H. Schwam, M.F. Sugrue, P. Gautheron, Thienothiopyran-2-sulfonamides: novel topically active carbonic anhydrase inhibitors for the treatment of glaucoma, Journal of medicinal chemistry, 32 (1989) 2510-2513.

[111] C.T. Supuran, Carbonic anhydrases: novel therapeutic applications for inhibitors and activators, Nature Reviews Drug Discovery, 7 (2008) 168-181.

[112] G.M. Bond, J. Stringer, D.K. Brandvold, F.A. Simsek, M.G. Medina, G. Egeland, Development of integrated system for biomimetic CO2 sequestration using the enzyme carbonic anhydrase, Energy & Fuels, 15 (2001) 309-316.

[113] N. Liu, G.M. Bond, A. Abel, B.J. McPherson, J. Stringer, Biomimetic sequestration of CO2 in carbonate form: Role of produced waters and other brines, Fuel processing technology, 86 (2005) 1615-1625.

[114] P. Mirjafari, K. Asghari, N. Mahinpey, Investigating the application of enzyme carbonic anhydrase for CO2 sequestration purposes, Industrial & engineering chemistry research, 46 (2007) 921-926.

[115] P. Strop, K.S. Smith, T.M. Iverson, J.G. Ferry, D.C. Rees, Crystal structure of the "cab"-type beta class carbonic anhydrase from the archaeon Methanobacterium thermoautotrophicum, J Biol Chem, 276 (2001) 10299-10305.

[116] C. Kisker, H. Schindelin, B.E. Alber, J.G. Ferry, D.C. Rees, A left-handed beta-helix revealed by the crystal structure of a carbonic anhydrase from the archaeon Methanosarcina thermophila, Embo Journal, 15 (1996) 2323-2330.

[117] B.E. Alber, J.G. Ferry, Characterization of heterologously produced carbonic anhydrase from Methanosarcina thermophila, Journal of Bacteriology, 178 (1996) 3270-3274.

[118] S.C. Gill, P.H. Vonhippel, Calculation of Protein Extinction Coefficients from Amino-Acid Sequence Data, Analytical Biochemistry, 182 (1989) 319-326.

[119] T. Zahnley, R. Macey, G. Oster, Berkeley Madonna, version 8.3.14, University of California: Berkeley, CA, (2006).

[120] A.L. Crumbliss, K.L. Mclachlan, J.P. Odaly, R.W. Henkens, Preparation and Activity of Carbonic-Anhydrase Immobilized on Porous Silica Beads and Graphite Rods, Biotechnology and Bioengineering, 31 (1988) 796-801.

[121] C. Prabhu, S. Wanjari, S. Gawande, S. Das, N. Labhsetwar, S. Kotwal, A.K. Puri, T. Satyanarayana, S. Rayalu, Immobilization of carbonic anhydrase enriched microorganism on biopolymer based materials, Journal of molecular catalysis B: Enzymatic, 60 (2009) 13-21.

[122] S. Bhattacharya, M. Schiavone, S. Chakrabarti, S.K. Bhattacharya, CO2 hydration by immobilized carbonic anhydrase, Biotechnology and applied biochemistry, 38 (2003) 111-117.

[123] P.V. Iyer, L. Ananthanarayan, Enzyme stability and stabilization—Aqueous and non-aqueous environment, Process Biochemistry, 43 (2008) 1019-1032.

[124] M. Wahlgren, T. Arnebrant, Protein adsorption to solid surfaces, Trends in biotechnology, 9 (1991) 201-208.

[125] F. Felsovalyi, T. Patel, P. Mangiagalli, S.K. Kumar, S. Banta, Effect of thermal stability on protein adsorption to silica using homologous aldo‐keto reductases, Protein Science, (2012).

[126] K.S. Lackner, S. Brennan, Envisioning carbon capture and storage: expanded possibilities due to air capture, leakage insurance, and C-14 monitoring, Climatic change, 96 (2009) 357-378.

[127] A.H.A. Park, L.S. Fan, CO2 mineral sequestration: physically activated dissolution of serpentine and pH swing process, Chemical Engineering Science, 59 (2004) 5241-5247.

[128] A.-S. Yang, B. Honig, On the pH dependence of protein stability, Journal of molecular biology, 231 (1993) 459.

[129] R.M. Daniel, The upper limits of enzyme thermal stability, Enzyme and Microbial Technology, 19 (1996) 74-79.

[130] A.S. Bommarius, B.B.R. Riebel, Biocatalysis: fundamentals and applications, Wiley. com, 2004.

[131] K.M. Polizzi, A.S. Bommarius, J.M. Broering, J.F. Chaparro-Riggers, Stability of biocatalysts, Current opinion in chemical biology, 11 (2007) 220-225.

[132] G. Vogt, S. Woell, P. Argos, Protein thermal stability, hydrogen bonds, and ion pairs, Journal of molecular biology, 269 (1997) 631-643.

[133] J.T. Kellis, D. Kerstin Nyberg, sbreve, Contribution of hydrophobic interactions to protein stability, (1988).

[134] R.L. Baldwin, How Hofmeister ion interactions affect protein stability, Biophysical journal, 71 (1996) 2056-2063.

[135] P. Argos, M.G. Rossmann, U.M. Grau, H. Zuber, G. Frank, J.D. Tratschin, Thermal stability and protein structure, Biochemistry, 18 (1979) 5698-5703.

[136] V.G. Eijsink, S. Gåseidnes, T.V. Borchert, B. van den Burg, Directed evolution of enzyme stability, Biomolecular engineering, 22 (2005) 21-30.

[137] V.G. Eijsink, A. Bjørk, S. Gåseidnes, R. Sirevåg, B. Synstad, B.v.d. Burg, G. Vriend, Rational engineering of enzyme stability, Journal of biotechnology, 113 (2004) 105-120.

[138] S. Spector, M. Wang, A. Stefan, O. James Robblee, Z.S. Hendsch, O. Robert Fairman, B. Tidor, P. Daniel, Rational modification of protein stability by the mutation of charged surface residues, Biochemistry, 39 (2000) 872-879.

[139] M. Matsumura, W.J. Becktel, M. Levitt, B.W. Matthews, Stabilization of phage T4 lysozyme by engineered disulfide bonds, Proceedings of the National Academy of Sciences, 86 (1989) 6562-6566.

[140] P. Meinhold, M.W. Peters, A. Hartwick, A.R. Hernandez, F.H. Arnold, Engineering cytochrome P450 BM3 for terminal alkane hydroxylation, Advanced Synthesis & Catalysis, 348 (2006) 763-772.

[141] R. Barbero, L. Carnelli, A. Simon, A. Kao, A.d.A. Monforte, M. Riccò, D. Bianchi, A. Belcher, Engineered yeast for enhanced CO2 mineralization, Energy & Environmental Science, 6 (2013) 660-674.

[142] T.N. Patel, A.-H.A. Park, S. Banta, Periplasmic expression of carbonic anhydrase in Escherichia coli: A new biocatalyst for CO2 hydration, Biotechnology and Bioengineering, 110 (2013) 1865-1873.

[143] B.K. Kanth, J. Lee, S.P. Pack, Carbonic anhydrase: Its biocatalytic mechanisms and functional properties for efficient CO2 capture process development, Engineering in Life Sciences, 13 (2013) 422-431.

[144] Y. Pocker, J. Stone, The Catalytic Versatility of Erythrocyte Carbonic Anhydrase. III. Kinetic Studies of the Enzyme-Catalyzed Hydrolysis of p-Nitrophenyl Acetate*, Biochemistry, 6 (1967) 668-678.

[145] K. Okrasa, R.J. Kazlauskas, Manganese‐Substituted Carbonic Anhydrase as a New Peroxidase, Chemistry-A European Journal, 12 (2006) 1587-1596.

[146] Y. Pocker, D. Bjorkquist, Comparative studies of bovine carbonic anhydrase in H2O and D2O. Stopped-flow studies of the kinetics of interconversion of CO2 and HCO3, Biochemistry, 16 (1977) 5698-5707.

[147] L. Gardossi, P.B. Poulsen, A. Ballesteros, K. Hult, V.K. Švedas, Đ. Vasić-Rački, G. Carrea, A. Magnusson, A. Schmid, R. Wohlgemuth, Guidelines for reporting of biocatalytic reactions, Trends in biotechnology, 28 (2010) 171-180.

[148] M. Scheer, A. Grote, A. Chang, I. Schomburg, C. Munaretto, M. Rother, C. Söhngen, M. Stelzer, J. Thiele, D. Schomburg, BRENDA, the enzyme information system in 2011, Nucleic acids research, 39 (2011) D670-D676.

[149] L. Leive, The barrier function of the Gram‐negative envelope, Annals of the New York Academy of Sciences, 235 (1974) 109-129.

[150] H. Nikaido, Transport across the bacterial outer membrane, Journal of bioenergetics and biomembranes, 25 (1993) 581-589.

[151] H. Nikaido, M. Vaara, Molecular basis of bacterial outer membrane permeability, Microbiological reviews, 49 (1985) 1.

[152] H. Nikaido, E.Y. Rosenberg, Porin channels in Escherichia coli: studies with liposomes reconstituted from purified proteins, Journal of bacteriology, 153 (1983) 241-252.

[153] R.E. Hancock, A. Bell, Antibiotic uptake into gram-negative bacteria, European Journal of Clinical Microbiology and Infectious Diseases, 7 (1988) 713-720.

[154] R. Hancock, Role of porins in outer membrane permeability, Journal of bacteriology, 169 (1987) 929.

[155] R. Benz, K. Janko, W. Boos, P. Läuger, Formation of large, ion-permeable membrane channels by the matrix protein (porin) of< i> Escherichia coli</i>, Biochimica et Biophysica Acta (BBA)-Biomembranes, 511 (1978) 305-319.

[156] R.E. Hancock, Alterations in outer membrane permeability, Annual Reviews in Microbiology, 38 (1984) 237-264.

[157] M. Vaara, Agents that increase the permeability of the outer membrane, Microbiological reviews, 56 (1992) 395-411.

[158] R. Irvin, T. MacAlister, J. Costerton, Tris (hydroxymethyl) aminomethane buffer modification of Escherichia coli outer membrane permeability, Journal of bacteriology, 145 (1981) 1397-1403.

[159] I. Helander, E.-L. Nurmiaho-Lassila, R. Ahvenainen, J. Rhoades, S. Roller, Chitosan disrupts the barrier properties of the outer membrane of Gram-negative bacteria, International journal of food microbiology, 71 (2001) 235-244.

[160] A. Sotirova, D. Spasova, D. Galabova, E. Karpenko, A. Shulga, Rhamnolipid–biosurfactant permeabilizing effects on gram-positive and gram-negative bacterial strains, Current Microbiology, 56 (2008) 639-644.

[161] B. Skerlavaj, D. Romeo, R. Gennaro, Rapid membrane permeabilization and inhibition of vital functions of gram-negative bacteria by bactenecins, Infection and immunity, 58 (1990) 3724-3730.

[162] C. Johansen, A. Verheul, L. Gram, T. Gill, T. Abee, Protamine-induced permeabilization of cell envelopes of gram-positive and gram-negative bacteria, Applied and environmental microbiology, 63 (1997) 1155-1159.

[163] H.R. Ibrahim, U. Thomas, A. Pellegrini, A helix-loop-helix peptide at the upper lip of the active site cleft of lysozyme confers potent antimicrobial activity with membrane permeabilization action, Journal of Biological Chemistry, 276 (2001) 43767-43774.

[164] B.A. Sampson, R. Misra, S.A. Benson, Identification and characterization of a new gene of Escherichia coli K-12 involved in outer membrane permeability, Genetics, 122 (1989) 491-501.

[165] M. Perez, B. García-Barreno, J.A. Melero, L. Carrasco, R. Guinea, Membrane Permeability Changes Induced in< i> Escherichia coli</i> by the SH Protein of Human Respiratory Syncytial Virus, Virology, 235 (1997) 342-351.

[166] D. Ma, D.N. Cook, M. Alberti, N.G. Pon, H. Nikaido, J.E. Hearst, Genes acrA and acrB encode a stress‐induced efflux system of Escherichia coli, Molecular microbiology, 16 (1995) 45-55.

[167] N.-K. Birkeland, Cloning, molecular characterization, and expression of the genes encoding the lytic functions of lactococcal bacteriophage ϕLCE: a dual lysis system of modular design, Canadian journal of microbiology, 40 (1994) 658-665.

[168] Y. Ni, R.R. Chen, Accelerating whole‐cell biocatalysis by reducing outer membrane permeability barrier, Biotechnology and bioengineering, 87 (2004) 804-811.

[169] L. Carrasco, Modification of membrane permeability by animal viruses, Advances in virus research, 45 (1995) 61-112.

[170] M.E. Gonzalez, L. Carrasco, Viroporins, FEBS letters, 552 (2003) 28-34.

[171] J.L. Nieva, V. Madan, L. Carrasco, Viroporins: structure and biological functions, Nature Reviews Microbiology, (2012).

[172] I.-N. Wang, D.L. Smith, R. Young, Holins: the protein clocks of bacteriophage infections, Annual Reviews in Microbiology, 54 (2000) 799-825.

[173] Y. Liao, J. Lescar, J. Tam, D. Liu, Expression of SARS-coronavirus envelope protein in< i> Escherichia coli</i> cells alters membrane permeability, Biochemical and biophysical research communications, 325 (2004) 374-380.

[174] J. Torres, K. Parthasarathy, X. Lin, R. Saravanan, A. Kukol, D.X. Liu, Model of a Putative Pore: The Pentameric< i> α</i>-Helical Bundle of SARS Coronavirus E Protein in Lipid Bilayers, Biophysical journal, 91 (2006) 938-947.

[175] K. Parthasarathy, L. Ng, X. Lin, D.X. Liu, K. Pervushin, X. Gong, J. Torres, Structural flexibility of the pentameric SARS coronavirus envelope protein ion channel, Biophysical journal, 95 (2008) L39-L41.

[176] K. Pervushin, E. Tan, K. Parthasarathy, X. Lin, F.L. Jiang, D. Yu, A. Vararattanavech, T.W. Soong, D.X. Liu, J. Torres, Structure and inhibition of the SARS coronavirus envelope protein ion channel, PLoS pathogens, 5 (2009) e1000511.

[177] L. Wilson, C. Mckinlay, P. Gage, G. Ewart, SARS coronavirus E protein forms cation-selective ion channels, Virology, 330 (2004) 322-331.

[178] B.H. Jo, J.H. Seo, D.G. Kang, H.J. Cha, Engineered Escherichia coli with Periplasmic Carbonic Anhydrase as a Biocatalyst for CO2 Sequestration, Applied and environmental microbiology, (2013).

[179] I. Helander, T. Mattila‐Sandholm, Fluorometric assessment of Gram‐negative bacterial permeabilization, Journal of applied microbiology, 88 (2000) 213-219.

[180] H.-L. Alakomi, E. Skyttä, M. Saarela, T. Mattila-Sandholm, K. Latva-Kala, I. Helander, Lactic acid permeabilizes gram-negative bacteria by disrupting the outer membrane, Applied and Environmental Microbiology, 66 (2000) 2001-2005.

[181] D. Nieva-Gomez, R.B. Gennis, Affinity of intact Escherichia coli for hydrophobic membrane probes is a function of the physiological state of the cells, Proceedings of the National Academy of Sciences, 74 (1977) 1811-1815.

[182] H.S. Fogler, Elements of Chemical Reaction Engineering, 4 ed., Prentice Hall, 2006.

[183] R. Dutta, Fundamentals of biochemical engineering, Ane Books India India, 2008.

[184] H. Nikaido, E.Y. Rosenberg, Effect on solute size on diffusion rates through the transmembrane pores of the outer membrane of Escherichia coli, The Journal of general physiology, 77 (1981) 121-135.

[185] A. Tamimi, E.B. Rinker, O.C. Sandall, Diffusion coefficients for hydrogen sulfide, carbon dioxide, and nitrous oxide in water over the temperature range 293-368 K, Journal of Chemical and Engineering data, 39 (1994) 330-332.

[186] J. Hobot, E. Carlemalm, W. Villiger, E. Kellenberger, Periplasmic gel: new concept resulting from the reinvestigation of bacterial cell envelope ultrastructure by new methods, Journal of bacteriology, 160 (1984) 143-152.

[187] S.G. Schultz, A. Solomon, Determination of the effective hydrodynamic radii of small molecules by viscometry, The Journal of general physiology, 44 (1961) 1189-1199.

[188] B.J. Zwolinski, H. Eyring, C.E. Reese, Diffusion and Membrane Permeability, The Journal of Physical Chemistry, 53 (1949) 1426-1453.

[189] B. Schmid, M. Krömer, G.E. Schulz, Expression of porin from< i> Rhodopseudomonas blastica</i> in< i> Escherichia coli</i> inclusion bodies and folding into exact native structure, FEBS letters, 381 (1996) 111-114.

[190] B. Schmid, L. Maveyraud, M. Krömer, G.E. Schulz, Porin mutants with new channel properties, Protein science, 7 (1998) 1603-1611.

[191] A.K. Mohanty, M.C. Wiener, Membrane protein expression and production: effects of polyhistidine tag length and position, Protein expression and purification, 33 (2004) 311-325.

[192] W.W. Ward, G. Swiatek, Protein purification, Current Analytical Chemistry, 5 (2009) 85-105.

[193] M. Bannwarth, G.E. Schulz, The expression of outer membrane proteins for crystallization, Biochimica et Biophysica Acta (BBA)-Biomembranes, 1610 (2003) 37-45.

[194] H.N. Chang, T.H. Park, A theoretical model for immobilized whole cell enzyme, Journal of theoretical biology, 116 (1985) 9-20.

[195] J. Blanchard, Problem Solving with Excel and Matlab, in, Board of Regents of the University of Wisconsin System, 2009.

[196] N. Favre, M.L. Christ, A.C. Pierre, Biocatalytic capture of CO< sub> 2</sub> with carbonic anhydrase and its transformation to solid carbonate, Journal of Molecular Catalysis B: Enzymatic, 60 (2009) 163-170.

[197] S.-W. Lee, S.-B. Park, S.-K. Jeong, K.-S. Lim, S.-H. Lee, M.C. Trachtenberg, On carbon dioxide storage based on biomineralization strategies, Micron, 41 (2010) 273-282.

[198] M. Vinoba, D.H. Kim, K.S. Lim, S.K. Jeong, S.W. Lee, M. Alagar, Biomimetic sequestration of CO2 and reformation to CACO3 using bovine carbonic anhydrase immobilized on SBA-15, Energy & Fuels, 25 (2010) 438-445.

[199] K. Naka, Y. Chujo, Control of crystal nucleation and growth of calcium carbonate by synthetic substrates, Chemistry of materials, 13 (2001) 3245-3259.

[200] A. McPHERSON, Review Current approaches to macromolecular crystallization, in: EJB Reviews 1990, Springer, 1991, pp. 49-71.

[201] G. Fu, S.R. Qiu, C.A. Orme, D.E. Morse, J.J. De Yoreo, Acceleration of calcite kinetics by abalone nacre proteins, Advanced materials, 17 (2005) 2678-2683.

[202] M. Gunthorpe, C. Sikes, A. Wheeler, Promotion and inhibition of calcium carbonate crystallization in vitro by matrix protein from blue crab exoskeleton, The Biological Bulletin, 179 (1990) 191-200.

[203] S. Elhadj, E. Salter, A. Wierzbicki, J. De Yoreo, N. Han, P. Dove, Peptide controls on calcite mineralization: polyaspartate chain length affects growth kinetics and acts as a stereochemical switch on morphology, Crystal growth & design, 6 (2006) 197-201.

[204] P. Malkaj, E. Dalas, Calcium carbonate crystallization in the presence of aspartic acid, Crystal growth & design, 4 (2004) 721-723.

[205] C. Li, G.D. Botsaris, D.L. Kaplan, Selective in vitro effect of peptides on calcium carbonate crystallization, Crystal growth & design, 2 (2002) 387-393.

[206] P.L. Corstjens, A. Van Der Kooij, C. Linschooten, G.J. Brouwers, P. Westbroek, E.W. Jong, GPA, A CALCIUM‐BINDING PROTEIN IN THE COCCOLITHOPHORID EMILIANIA HUXLEYI (PRYMNESIOPHYCEAE), Journal of phycology, 34 (1998) 622-630.

[207] J.J. Rice, P.S. Daugherty, Directed evolution of a biterminal bacterial display scaffold enhances the display of diverse peptides, Protein Engineering Design and Selection, 21 (2008) 435-442.

[208] S. Goutelle, M. Maurin, F. Rougier, X. Barbaut, L. Bourguignon, M. Ducher, P. Maire, The Hill equation: a review of its capabilities in pharmacological modelling, Fundamental & clinical pharmacology, 22 (2008) 633-648.

[209] K. Jørgensen, A.V. Rasmussen, M. Morant, A.H. Nielsen, N. Bjarnholt, M. Zagrobelny, S. Bak, B.L. Møller, Metabolon formation and metabolic channeling in the biosynthesis of plant natural products, Current opinion in plant biology, 8 (2005) 280-291.

[210] H. McMurtrie, H. Cleary, B. Alvarez, F. Loiselle, D. Sterling, P. Morgan, D. Johnson, J. Casey, The bicarbonate transport metabolon, Journal of enzyme inhibition and medicinal chemistry, 19 (2004) 231-236.

[211] T.F. Moraes, R.A. Reithmeier, Membrane transport metabolons, Biochimica et Biophysica Acta (BBA)-Biomembranes, 1818 (2012) 2687-2706.

[212] D. Sowah, J.R. Casey, An intramolecular transport metabolon: fusion of carbonic anhydrase II to the COOH terminus of the Cl−/HCO3− exchanger, AE1, American Journal of Physiology-Cell Physiology, 301 (2011) C336-C346.

[213] C. Vélot, M.B. Mixon, M. Teige, P.A. Srere, Model of a quinary structure between Krebs TCA cycle enzymes: a model for the metabolon, Biochemistry, 36 (1997) 14271-14276.

[214] H.O. Spivey, J. Ovádi, Substrate channeling, Methods, 19 (1999) 306-321.

8. Publications

Felsovalyi, F, **Patel, TN**, Mangiagalli, P, Kumar, SK, and Banta, S. "Effect of thermal stability on protein adsorption to silica using homologous aldo-keto reductases." *Protein Science* 21(8), pp 1113-1125 (2012).

Patel, TN, Park, AH, and Banta, S. "Periplasmic expression of carbonic anhydrase in *Escherichia coli*: a new biocatalyst for CO_2 hydration." *Biotechnology and Bioengineering* 110(7), pp 1865-1873 (2013).

Patel, TN, Swanson, EJ, Park, AH, and Banta, S. "An automated method for measuring the operational stability of biocatalysts with carbonic anhydrase activity." *In press*, *Biochemical Engineering Journal* (2013).

Patel, TN, Park, AH, and Banta, S. "Genetic Manipulation of Outer Membrane Permeability: Generating Porous Heterogeneous Catalyst Analogs in *Escherichia coli*." *In review* (2013).

Patel, TN, Park, AH, and Banta, S. "Surface display of small peptides on *Escherichia coli* for enhanced calcite (CaCO3) precipitation kinetics." *In preparation* (2013).